ANALYSIS OF DC POWER SYSTEMS CONTAINING

INDUCTION MOTOR-DRIVE LOADS

Except where reference is made to the work of others, the work described in this thesis is my own or was done in collaboration with my advisory committee. This thesis does not include proprietary or classified information.

_____

Aleck Wayne Leedy

Certificate of Approval:

_____	_____
S. Mark Halpin	R. Mark Nelms, Chair
Professor	Professor
Electrical and Computer Engineering	Electrical and Computer Engineering
_____	_____
Charles A. Gross	John Y. Hung
Professor	Associate Professor
Electrical and Computer Engineering	Electrical and Computer Engineering

_____

Stephen L. McFarland
Dean
Graduate School

ANALYSIS OF DC POWER SYSTEMS CONTAINING INDUCTION MOTOR-DRIVE LOADS

Aleck Wayne Leedy

A Dissertation

Submitted to

the Graduate Faculty of

Auburn University

in Partial Fulfillment of the

Requirements for the

Degree of

Doctor of Philosophy

Auburn, Alabama
May 11, 2006

ANALYSIS OF DC POWER SYSTEMS CONTAINING

INDUCTION MOTOR-DRIVE LOADS

Aleck Wayne Leedy

Permission is granted to Auburn University to make copies of this dissertation at its discretion, upon request of individuals or institutions and at their expense. The author reserves all publication rights.

_____
Signature of Author

_____
Date of Graduation

VITA

Aleck Wayne Leedy, son of Robert Aleck and Jane (Pigmon) Leedy, was born February 10, 1973, in Pennington Gap, Virginia. He graduated from Lee High School in Jonesville, Virginia in 1991. He entered the University of Kentucky in August, 1991, and graduated with a Bachelor of Science degree in Electrical Engineering with a Minor in Mathematics on May 5, 1996. After working for Mountain Empire Community College and The Trane Company, he entered Graduate School at the University of Kentucky in May, 1998. He graduated from the University of Kentucky with a Master of Science in Mining Engineering (Electrical Engineering emphasis) on May 6, 2001. Following his thesis defense, he entered Graduate School at Auburn University in March, 2001. He is a registered Professional Engineer in the Commonwealth of Kentucky.

DISSERTATION ABSTRACT

ANALYSIS OF DC POWER SYSTEMS CONTAINING

INDUCTION MOTOR-DRIVE LOADS

Aleck W. Leedy

Doctor of Philosophy, May 11, 2006
(M.S., University of Kentucky, 2001)
(B.S., University of Kentucky, 1996)

157 Typed Pages

Directed by R. Mark Nelms

The development of an analytical method used for conducting a power flow analysis on a DC power system containing multiple motor-drive loads is presented. The method is fast, simplistic, easy to implement, and produces results that are comparable to software packages such as PSPICE and Simulink. The method presented utilizes a simplified model of a voltage source inverter-fed induction motor, which is based on the steady-state T-type harmonic equivalent circuit model of the induction motor and the input-output relationships of the inverter. In the simplified model, a V-I load characteristic curve is established that allows the inverter, motor, and load to be replaced by a current-controlled voltage source. This simplified model can be utilized in the

analysis of a multiple-bus DC power system containing motor-drive loads by incorporating the V-I load characteristic curve of each motor-drive load into an iterative procedure based on the Newton-Raphson method. The analytical method presented is capable of analyzing DC power systems containing induction motor-drive loads fed from voltage source inverters with various types of switching schemes. The speed advantage of the analytical method presented versus simulation packages such as PSPICE is apparent when analyzing multiple motor-drive systems.

ACKNOWLEDGMENTS

I would like to thank my advisor, Dr. R. Mark Nelms, for his advice and guidance throughout my graduate studies at Auburn University. I am grateful to Dr. Charles A. Gross for providing an EMAP simulation that was used for comparison with my induction motor harmonic model that was used in this dissertation. I would also like to thank Dr. Gross for his helpful suggestions and his willingness to share some of his knowledge of electric machines with me. I want to thank the other members of my committee, Dr. S. Mark Halpin and Dr. John Y. Hung, for their time and suggestions during the proposal and review of my dissertation. I would like to thank my parents, Jane E. (Pigmon) Leedy and the late Robert A. Leedy, for always stressing to me the importance of a sound education. Most of all, I want to thank my wife, Stephanie J. Leedy, for her love, support, and encouragement during my graduate studies at Auburn University.

Style manual or journal used Graduate School: Guide to Preparation and Submission of Theses and Dissertations.

Computer software used: Microsoft Word 2003, Microsoft Excel 2003, Microsoft Visio 2000, MATLAB 6.5, and PSPICE 9.2.

TABLE OF CONTENTS

LIST OF TABLES xi

LIST OF FIGURES xiii

CHAPTER 1 INTRODUCTION 1
1.1 Introduction 1
1.2 Background 4
1.2.1 The Six-Step Inverter 4
1.2.2 The Sinusoidal PWM Inverter 6
1.2.3 The Space Vector PWM Inverter 9
1.2.4 The Induction Motor 11
1.3 Organization of Dissertation 12

CHAPTER 2 HARMONIC ANALYSIS OF THE VOLTAGE SOURCE INVERTER 14
2.1 The Sinusoidal PWM Inverter 14
2.1.1 The Two-Level PWM Inverter 15
2.1.1.1 Harmonic Analysis of the Two-Level Inverter Using the Method of Pulse Pairs 18
2.1.1.2 Simulation Results for the Two-Level PWM Inverter 25
2.1.2 The Three-Level PWM Inverter 30
2.1.2.1 Harmonic Analysis of the Three-Level Inverter Using the Method of Pulse Pairs 32
2.1.2.2 Simulation Results for the Three-Level PWM Inverter 36
2.1.2.3 Comparison of New and Old Methods 40
2.2 The Space Vector PWM Inverter 42
2.2.1 Carrier-Based Approach 43
2.2.2 Method of Multiple Pulses 46
2.2.3 Simulation Results for the Space Vector PWM Inverter 51
2.3 Line-Neutral Voltage Fourier Series Development 55
2.3.1 The Six-Step Inverter 56
2.3.1.1 120° Conduction 56
2.3.1.2 180° Conduction 57
2.3.2 The Two-Level Sinusoidal PWM Inverter 58
2.3.3 The Space Vector PWM Inverter 68
2.4 Summary 73

CHAPTER 3 THE INVERTER-FED INDUCTION MOTOR 75
3.1 Induction Motor Equivalent Circuit 75
3.2 Verification of Induction Motor Harmonic Model 83
3.3 Motor-Drive System Model 83
3.3.1 Simplified Model Simulation Results 88
3.3.2 Six-Step Inverter Results 89
3.3.3 Two-Level Sinusoidal PWM Inverter Simulation Results 91
3.3.4 Space Vector PWM Inverter Simulation Results 93
3.4 Summary 95

CHAPTER 4 MULTIPLE MOTOR DRIVE SYSTEMS 96
4.1 DC Power Flow 97
4.2 Verification of the Power Flow Algorithm 100
4.3 Six-Step Simulation Results for a 10-Bus System 115
4.4 Two-Level Sinusoidal PWM Simulation Results 120
4.5 Power Flow Results for Systems with Higher Line Resistance Values 123
4.6 Summary 132

CHAPTER 5 CONCLUSIONS 133
5.1 Summary 133
5.2 Recommendations for Future Work 136

REFERENCES 138

LIST OF TABLES

TABLE 2.1 MATLAB AND PSPICE RESULTS FOR m_a=0.3 and m_f=9 27
TABLE 2.2 MATLAB AND PSPICE RESULTS FOR m_a=0.6 and m_f=15 27
TABLE 2.3 MATLAB AND PSPICE RESULTS FOR m_a=1.4 and m_f=15 28
TABLE 2.4 MATLAB AND PSPICE RESULTS FOR m_a=2.2 and m_f=25 28
TABLE 2.5 MATLAB AND PSPICE RESULTS FOR m_a=0.8 and m_f=10 38
TABLE 2.6 MATLAB AND PSPICE RESULTS FOR m_a=1.4 and m_f=16 38
TABLE 2.7 MATLAB AND PSPICE RESULTS FOR m_a=1.8 and m_f=20 39
TABLE 2.8 MATLAB AND PSPICE RESULTS FOR m_a=2.2 and m_f=20 39
TABLE 2.9 BESSEL FUNCTION METHOD AND PSPICE RESULTS FOR m_a=1.4 and m_f=18.....41
TABLE 2.10 METHOD OF PULSE PAIRS AND PSPICE RESULTS FOR m_a=1.4 and m_f=18.....42
TABLE 2.11 MATLAB AND PSPICE RESULTS FOR M=0.5 and m_f=9 52
TABLE 2.12 MATLAB AND PSPICE RESULTS FOR M=0.866 and m_f=9 53
TABLE 2.13 MATLAB AND PSPICE RESULTS FOR M=0.7 and m_f=15 53
TABLE 2.14 MATLAB AND PSPICE RESULTS FOR M=0.65 and m_f=15 54
TABLE 2.15 LINE-TO-NEGATIVE DC BUS VOLTAGE COMPONENTS FOR m_a=1.4 and m_f=15.....67
TABLE 2.16 LINE-TO-NEUTRAL VOLTAGE COMPONENTS FOR m_a=1.4 and m_f=15.....68
TABLE 2.17 LINE-TO-NEGATIVE DC BUS VOLTAGE COMPONENTS FOR M=0.7 and m_f=15.....72
TABLE 2.18 LINE-TO-NEUTRAL VOLTAGE COMPONENTS FOR M=0.7 and m_f=15.....73
TABLE 3.1 50 HP, 3-PHASE, INDUCTION MOTOR PARAMETERS 84
TABLE 3.2 MATLAB AND EMAP SIX-STEP INVERTER RESULTS.....84
TABLE 3.3 DIFFERENCES AND PERCENT ERRORS 85
TABLE 4.1 4-BUS SYSTEM LINE RESISTANCES AND LOAD TORQUES 101
TABLE 4.2 POWER FLOW RESULTS FOR THE 4-BUS SYSTEM.....115
TABLE 4.3 SYSTEM LINE RESISTANCES AND LOAD TORQUES 118
TABLE 4.4 POWER FLOW RESULTS FOR THE SIX-STEP INVERTER 120
TABLE 4.5 SYSTEM LINE RESISTANCES AND LOAD TORQUES 121
TABLE 4.6 POWER FLOW RESULTS FOR THE TWO-LEVEL SINE PWM INVERTER 123
TABLE 4.7 HARMONIC CONTENT OF INVERTER CURRENT AND VOLTAGE 130

TABLE 4.8 SYSTEM LINE RESISTANCES AND LOAD TORQUES 130
TABLE 4.9 POWER FLOW RESULTS WITH LARGER LINE RESISTANCES 131

LIST OF FIGURES

Figure 1.1 Motor-Drive System Model 2
Figure 1.2 DC Power System Model 2
Figure 1.3 Three-Phase Voltage Source Inverter 3
Figure 1.4 Carrier Waveform and Control Signal for a Sinusoidal PWM Inverter 7
Figure 1.5 Carrier Waveform and Control Signal for a Space Vector PWM Inverter 10
Figure 1.6 Induction Motor T-Type Equivalent Circuit 12
Figure 2.1 Triangular Waveform and Control Signal 16
Figure 2.2 Single-Phase Inverter 17
Figure 2.3 Two-Level PWM Output Waveform 18
Figure 2.4 Positive Pulse Pair 19
Figure 2.5 Negative Pulse Pair 19
Figure 2.6 PWM Output Signal with Positive and Negative Pulse Pairs Labeled 23
Figure 2.7 Special Case Crossing Points 25
Figure 2.8 Harmonic Spectrum with m_a=1.0 and m_f=25 29
Figure 2.9 Carrier Waveform and Control Signal 31
Figure 2.10 Three-Level PWM Output Waveform 31
Figure 2.11 Three-Level PWM Alternative Method 32
Figure 2.12 Positive Pulse Pair 33
Figure 2.13 PWM Output Signal with Pulse Pairs Labeled 35
Figure 2.14 Special Case Crossing Points 36
Figure 2.15 Harmonic Spectrum with m_a=0.9 and m_f=16 40
Figure 2.16 Triangular Waveform and Space Vector Control Signal 44
Figure 2.17 Space Vector PWM Output Waveform 45
Figure 2.18 Positive Pulse 47
Figure 2.19 Negative Pulse 47
Figure 2.20 PWM Output Signal with Positive and Negative Pulses Labeled 50
Figure 2.21 Harmonic Spectrum with M=1.1 and m_f=27 54
Figure 2.22 Three-Phase Inverter Block Model 55
Figure 2.23 Six-Step Phase *a* Voltage Waveform with 120° Conduction 57
Figure 2.24 Six-Step Phase *a* Voltage Waveform with 180° Conduction 57
Figure 2.25 Three-Phase Sinsusoidal PWM Control Signals and Carrier Waveform 59
Figure 2.26 Line-to-Negative DC Bus Voltage Waveforms 60
Figure 2.27 Waveform $v_{aN}(t)$ with Pulses Labeled 61
Figure 2.28 Phase *a* Line-to-Neutral Voltage Produced using MATLAB 62
Figure 2.29 Harmonic Spectrum of the Phase *a* Line-to-Negative DC Bus Voltage 62

Figure 2.30 Harmonic Spectrum of the Phase *a* Line-to-Neutral Voltage 63
Figure 2.31 Space Vector PWM Control Signal and Carrier Waveform 69
Figure 2.32 Line-to-Negative DC Bus Voltage Waveforms 63
Figure 2.33 Phase *a* Line-to-Neutral Voltage Waveform 70
Figure 3.1 (a) Induction Motor T-Type Equivalent Circuit;
(b) Thevenin Equivalent of (a) 76
Figure 3.2 (a) Induction Motor Harmonic Equivalent Circuit;
(b) Thevenin Equivalent of (a) 80
Figure 3.3 Positive-Sequence Harmonic Equivalent Circuit 82
Figure 3.4 Negative-Sequence Harmonic Equivalent Circuit 82
Figure 3.5 Motor-Drive System Model 85
Figure 3.6 V-I Data Points 87
Figure 3.7 Linear Curve Fit 88
Figure 3.8 Quadratic Curve Fit 88
Figure 3.9 Simplified System Model 89
Figure 3.10 V-I Load Curve Produced From MATLAB Code 90
Figure 3.11 V-I Load Curve Produced From PSPICE Simulations 91
Figure 3.12 V-I Characteristic Curve For a Sinusoidal PWM Inverter
with T_L=100 N-m 92
Figure 3.13 Quadratic Curve Fit for T_L=100 N-m 92
Figure 3.14 V-I Curve For a Space Vector PWM Inverter with T_L=80 N-m 94
Figure 3.15 Quadratic Curve Fit for T_L=80 N-m 94
Figure 4.1 DC Power System Model 98
Figure 4.2 Four-Bus DC Power System 101
Figure 4.3 V-I Characteristic Curve for T_L=75 N-m 105
Figure 4.4 Quadratic Curve Fit for T_L=75 N-m 106
Figure 4.5 V-I Characteristic Curve for T_L=40 N-m 106
Figure 4.6 Quadratic Curve Fit for T_L=40 N-m 107
Figure 4.7 PSPICE 4-bus System Model 113
Figure 4.8 PSPICE Six-Step Motor-Drive Model 114
Figure 4.9 PSPICE Induction Motor Part 115
Figure 4.10 10-Bus DC Power System Model 116
Figure 4.11 PSPICE 10-Bus Power System Model 119
Figure 4.12 PSPICE Sinusoidal PWM Motor-Drive Model 122
Figure 4.13 Six-Step Inverter System with a Low Line Resistance Value 124
Figure 4.14 Line-to-Line Voltages with Low Line Resistance 125
Figure 4.15 Inverter DC Input Current and Voltage with Low Line Resistance 125
Figure 4.16 Six-Step Inverter System with a Higher Line Resistance Value 127
Figure 4.17 Line-to-Line Voltage (V_{ab}) with a Higher Line Resistance 128
Figure 4.18 Inverter Input Voltage with a Higher Line Resistance 128
Figure 4.19 Inverter Input Current with a Higher Line Resistance 129

CHAPTER 1

1.1 Introduction

This effort has been focused on the analysis of the system shown in Figure 1.1. In this figure, a DC voltage source is connected to a three-phase inverter driving a three-phase induction motor with a load attached. The goal was to develop an analytical method to analyze this system that is faster than simulation packages such as PSPICE and Simulink and produces comparable results. The method can be utilized in the analysis of a DC power system containing multiple motor-drive loads such as the one shown in Figure 1.2. The speed advantage of the analytical method is evident when multiple motor-drive systems are analyzed.

Some possible applications for DC power systems such as the one shown in Figure 1.2 are: transit systems, U.S Navy ships and submarines, and some coal mining operations. The induction motor was utilized in Figure 1.2 because it is employed in some of the applications mentioned previously. Induction motors are used in a wide range of industrial settings as they are capable of operating in dusty and harsh environments such as in underground coal mines.

The output voltage waveforms produced by the inverter shown in Figure 1.1 will contain harmonics. The harmonic content of the output waveforms will depend on the switching scheme utilized in the voltage source inverter of Figure 1.1. A more detailed drawing of a three-phase voltage source inverter is illustrated in Figure 1.3. Depending

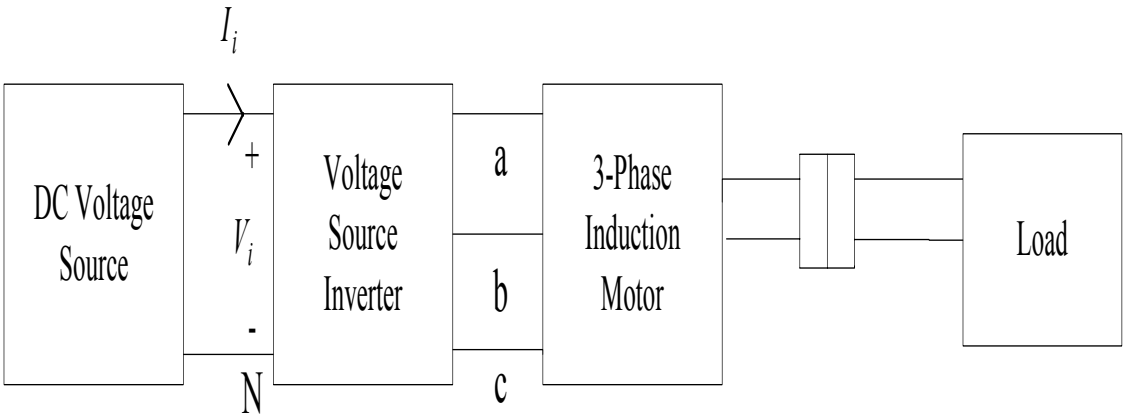

Figure 1.1: Motor-Drive System Model.

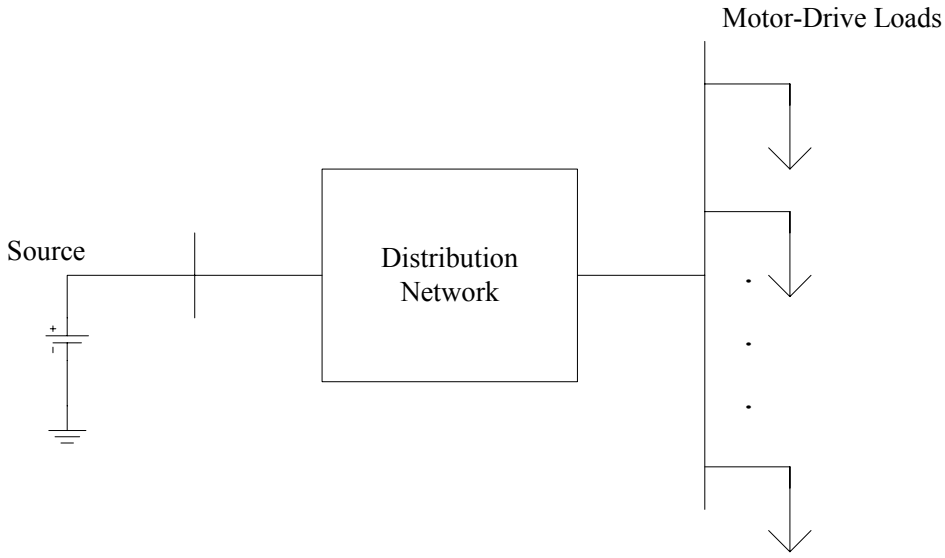

Figure 1.2: DC Power System Model.

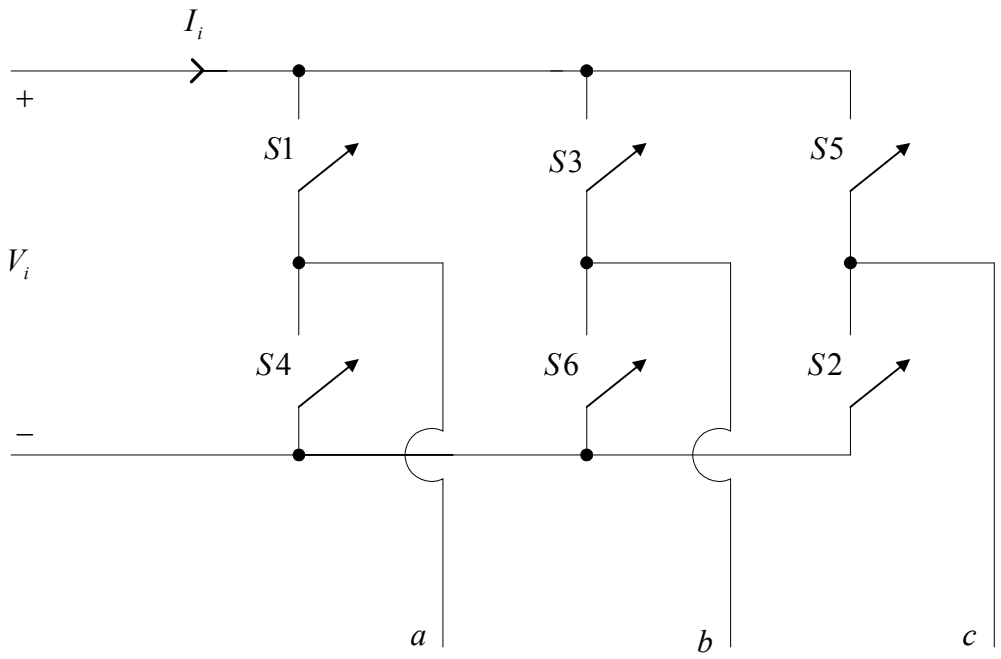

Figure 1.3: Three-Phase Voltage Source Inverter.

upon the method for controlling the switches of the inverter in Figure 1.3, the inverter can operate as a six-step inverter, sinusoidal PWM inverter, or a space vector PWM inverter. Two methods for determining the harmonic components of the output waveforms of the voltage source inverter in Figure 1.3 were developed in this dissertation. Both methods can be used to determine the harmonic content of the inverter output waveforms for different switching schemes. The two harmonic analysis methods developed allow direct calculation of harmonic magnitudes and angles without having to use linear approximations, iterative procedures, look-up tables, or Bessel functions. These methods can also be extended to other types of multilevel inverters and PWM schemes.

Because the voltages at the terminals of the induction motor shown in Figure 1.1 will contain harmonics produced by the inverter, a harmonic model of the induction motor

was developed that is based on the steady-state T-type equivalent circuit model of the induction motor. A simplified model of the system shown in Figure 1.1 was developed using the induction motor harmonic model and the input-output relationships of the voltage source inverter. In the simplified model a *V-I* load characteristic curve was established that allows all of the system components to the right of V_i (inverter, motor, and load) in Figure 1.1 to be replaced by a current-controlled voltage source. The simplified model developed for the system in Figure 1.1 was shown to be applicable to a multiple-bus DC power system such as that shown in Figure 1.2 by forming a *V-I* load characteristic curve for each motor-drive load in the system and incorporating them into an iterative procedure used to conduct a power flow analysis.

1.2 Background

1.2.1 The Six-Step Inverter

The six-step inverter is perhaps the simplest form of three-phase inverter. A circuit diagram of a three-phase voltage source inverter is shown in Figure 1.3. The output of a six-step inverter can be produced by using one of two types of gate firing sequences: three switches in conduction at the same time (180° conduction), or two switches in conduction at the same time (120° conduction). With either case, the gating signals are applied and removed every 60° of the output voltage waveform. The switches in Figure 1.3 are gated in the sequence S1, S2, S3, S4, S5, and S6 every cycle. The result of this type of gating produces six steps in each cycle. Even though the six-step inverter is simplistic compared to the various types of PWM inverters, many articles have been written covering different applications and various aspects of the operation of the six-step voltage source inverter [1-7].

Murphy and Turnbull [8] discussed AC motor operation when supplied by a six-step voltage source inverter in Chapter 4 of their book. Voltage waveforms were provided along with the Fourier series representations. Current waveforms were also provided with detailed discussions of motor operation when supplied by a six-step inverter.

Abbas and Novotny [9] utilized a fundamental component approximation to develop equivalent circuits that represent the transfer relations of the six-step voltage source and current source inverters during steady-state operation. Development of the equivalent circuits was based on the idealized switching constraints of the inverter circuits. Only the fundamental component of the voltage and current Fourier series was retained in the development of the equivalent circuits presented. This simplification was made due to the harmonics resulting in small amounts of average torque.

Krause and Lipo [10] presented simplified representations of a rectifier-inverter induction motor drive system. The first simplified representation was developed by neglecting the harmonic components due to the switching in the rectifier. The second simplified representation resulted when the harmonic components due to the switching in the inverter were neglected. The final simplification was made by neglecting all harmonic components and representing the system in the synchronously rotating reference frame. In the analysis leading to the final simplified system representation, the operation of the inverter was expressed analytically in the synchronously rotating reference frame with the harmonic components due to the switching in the inverter included.

Krause and Hake [11] used the method of multiple reference frames and the equations of transformation of the inverter to establish a method of calculating the inverter input

current. The method presented allows the current flowing into the inverter to be determined during constant speed, steady-state operation.

Novotny [12] used time dependent functions called switching functions to represent transfer properties of six-step voltage source and current source inverters. The switching functions were expanded as complex Fourier series and applied to steady-state inverter operation. The concepts presented can be extended to PWM inverters.

Novotny [13] used time domain complex variables to represent the inverter and the induction motor. Time domain complex variables result from applying the symmetrical component concept to instantaneous quantities. Steady-state analysis of the six-step voltage and current source inverter-driven induction motor is provided. Closed form solutions for the instantaneous voltages, currents, and torques were presented.

1.2.2 The Sinusoidal PWM Inverter

Pulse width modulation is a popular technique used to control the magnitude and frequency of the AC output voltages of an inverter. In a sinusoidal PWM inverter, the gate signals used to control the switches of the inverter in Figure 1.3 are produced by comparing a sinusoidal control signal with a high frequency carrier waveform as shown in Figure 1.4 for a two-level sinusoidal PWM inverter. This technique is widely used in industrial applications such as variable-speed electric drives [14, 15] and has been the focus of research interests in power electronics applications for many years. Most of the research to date has been focused on determining the harmonic components produced as a result of the modulation process due to various schemes and techniques [14, 16-18].

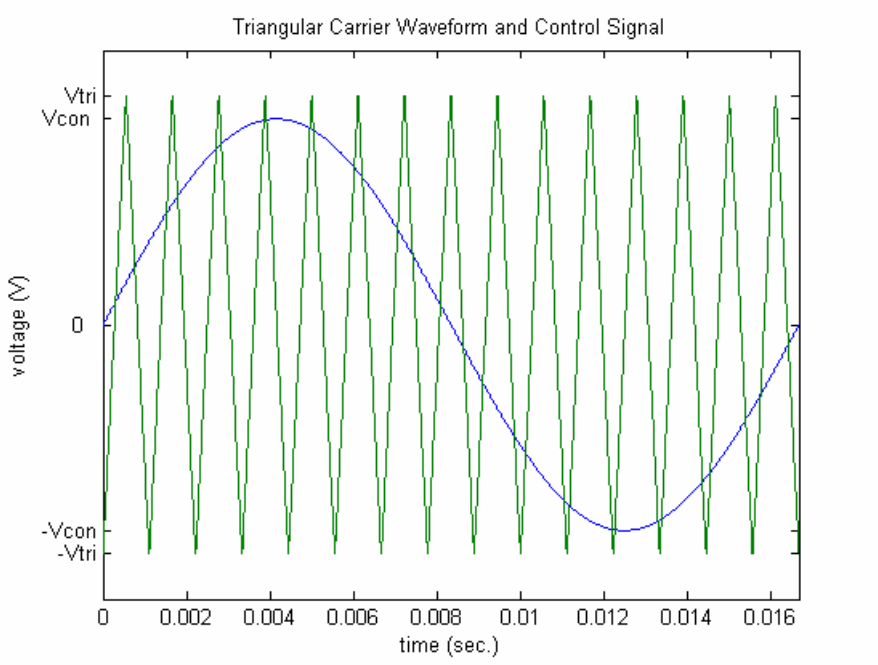

Figure 1.4: Carrier Waveform and Control Signal for a Sinusoidal PWM Inverter.

Analysis of modulated pulses was first introduced by Bennett [19] in 1933. Bennett used the double Fourier series to analyze modulated pulses in his study of rectified waves. Bennett's method was shown to be applicable to various types of waveforms and complex modulation processes. A detailed explanation of Bennett's method as applied to communications systems was presented by Black [20]. Bowes [21,22] was the first to use Bennett's method in power electronics applications. Bowes used a 3-D modulation model based on the double Fourier series to apply Bennett's method to inverter systems. The method introduced by Bennett and applied by Black and Bowes is valid only for amplitude modulation ratios less than one. Using the waveforms of a two-level sinusoidal PWM inverter with sine-triangle modulation in Figure 1.4, the amplitude modulation ratio is defined as:

$$m_a = \frac{V_{con}}{V_{tri}} \tag{1.1}$$

where V_{con} is the peak amplitude of the control signal in Figure 1.4 and V_{tri} is the peak amplitude of the triangular carrier waveform in Figure 1.4.

Extensions of Bennett's method to calculate the harmonic content of the output voltage of a PWM inverter for amplitude modulation ratios greater than one were presented by Franzo et al. [15] and Mazzucchelli et al. [23]. Carrara et al. [24] used an extension of Bennett's method to find analytical expressions of the output voltage of single-phase and three-phase inverters. Calculations of the harmonic components of the output voltage of the inverter were possible for any operating condition, including the over modulation region m_a>1.0. The analysis presented was applied to various multilevel modulation techniques.

Holmes [25] presented a generalized analytical approach for calculating the harmonic components of various fixed carrier frequency PWM schemes. The method was based on the double Fourier series of the switched waveform. Holmes produced closed form solutions using a Jacobi-Anger substitution. Analytical solutions were provided for various PWM strategies including space vector modulation.

Tseng, et al. [26] used a 3-D modulation model and the double Fourier series as first proposed by Bennett to analyze the harmonic characteristics of a three-phase two-level PWM inverter. Models of the three-phase inverter system were constructed in PSPICE and MATLAB for harmonic analysis purposes. Equations from the theoretical analysis using the 3-D modulation model and the double Fourier series were coded in MATLAB for comparison with PSPICE and Simulink results. It was shown that the harmonic

content of waveforms produced from the PSPICE and Simulink models are in good agreement with the harmonic content of waveforms calculated using the 3-D modulation model and the double Fourier series.

Mohan et al. [27] conducted an analysis of two-level PWM inverters in Chapter 8 of their book. Design considerations for the two-level PWM were discussed in Chapter 8 as well. Harmonic analysis of the induction motor was discussed in Chapter 14.

Various schemes using pulse width modulation for the purpose of shaping the AC output voltages of an inverter to be as close to sinusoidal as possible have been studied and continue to be the focus of many power electronics research activities. For the interested researcher, a detailed literature review on pulse width modulation that includes various modulation techniques and schemes can be found in [16].

1.2.3 The Space Vector PWM Inverter

Space vector modulation is a PWM technique that has become extremely popular in recent years. In a space vector PWM inverter, the gate signals used to control the switches of the inverter in Figure 1.3 are produced by comparing the control signal shown in Figure 1.5 with a high frequency triangular waveform. The space vector PWM inverter is commonly used in vector control drive applications [28] where microprocessors are used to generate voltage waveforms [29]. Even though many articles are available in the literature [16], space vector pulse width modulation continues to be the focus of many power electronics researchers [30, 31]. Space vector modulation was first introduced in the mid-1980's [32-34] and was greatly advanced by Van Der Broeck [33] in 1988. The method was initially developed as a vector approach to pulse

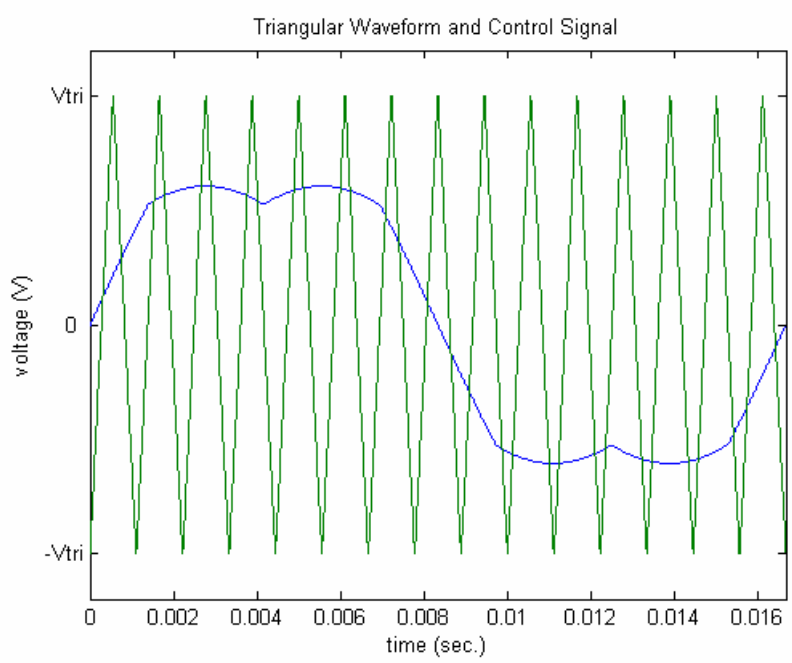

Figure 1.5: Carrier Waveform and Control Signal for a Space Vector PWM Inverter.

width modulation. The approach used by Van Der Broeck was based on representing voltages using space vectors in the α, β plane.

Harmonic analysis of the space vector PWM inverter has been investigated by various researchers [16, 29, 35-37]. Boys and Handley [29] decomposed a general regularly sampled asymmetric PWM waveform into symmetrical components that simplified the harmonic analysis of the PWM output waveform. The technique was extended by Boys and Handley to analyze waveforms generated by space vector modulation. Bresnahan et al. [35] conducted a harmonic analysis of space vector line-to-line voltages generated by a microcontroller. An FFT analyzer and MATLAB/Simulink routines were used to conduct the harmonic analysis. Moynihan et al. [36] used an extension of the geometric-wall model to conduct a harmonic analysis on space vector modulated waveforms.

Harmonic analysis of two different space vector PWM methods was presented by Halasz et al. [37]. Holmes and Lipo presented a technique used to analyze the harmonic content of space vector PWM waveforms using a double Fourier series method [16]. A detailed explanation of the technique was provided along with the mathematical derivation of the analytical results.

Panaitescu and Mohan [38] presented an analysis and hardware implementation of space vector pulse width modulation used for voltage source inverter-fed AC motor drives. A carrier-based approach was used without the need for sector calculations or vector decomposition.

Mohan [39] presents a detailed explanation of space vector PWM inverters in Chapter 7 of his book. A CD was provided with examples and Simulink® models that are helpful in understanding space vector concepts. Mohan used a carrier-based approach to analyze the space vector PWM inverter.

1.2.4 The Induction Motor

Fitzgerald, et al. [40] provided a detailed analysis of the steady-state T-type equivalent circuit model of the induction motor in Chapter 7 of their book. The model presented in Chapter 7, and shown in Figure 1.6, can easily be modified in order to perform a harmonic analysis on the induction motor.

Ozpineci and Tolbert [41] presented a modular Simulink implementation of an induction motor model. In the model presented, each block solved one of the model equations. This "modular" system model allowed all of the machine parameters to be accessible for control and verification of results.

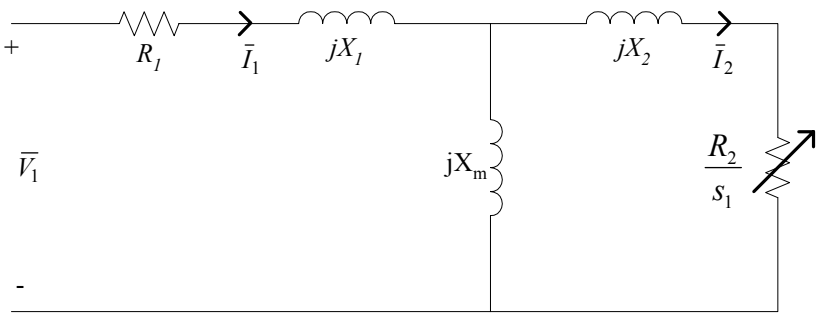

Figure 1.6: Induction Motor T-Type Equivalent Circuit.

Giesselmann [42] developed a PSPICE d-q model of the induction motor for analysis and simulation purposes. The PSPICE model was based on the T-type equivalent circuit model of the induction motor. Implementation of the d-q model equations in PSPICE was accomplished using Analog Behavioral Modeling (ABM) devices. Expression based ABM devices allow the user to enter mathematical expressions that can be used in PSPICE circuit models.

Krause [43] used reference frame theory for the analysis of electric machines in Chapter 3 of his book. In Chapter 4, a detailed d-q analysis of the induction motor is presented. Reference frame theory as applied to the analysis of electric drives is discussed in Chapter 13.

1.3 Organization of the Dissertation

In this introductory chapter, a description of the problem to be investigated, the goals of the dissertation, and background information on previous work relating to voltage source inverter-fed induction motor drives have been presented. Harmonic analysis of the voltage source inverter and two methods for determining the harmonic components of the output of a voltage source inverter are discussed in Chapter 2. A harmonic model of

the induction motor and the development of a simplified model of an inverter-fed induction motor are discussed in Chapter 3. Multiple motor-drive systems are the focus of Chapter 4, with a presentation of an iterative procedure that can be used to conduct a power flow analysis on a DC power system containing multiple motor-drive loads. The dissertation concludes with a summary of the dissertation and recommendations for future work in Chapter 5.

CHAPTER 2

HARMONIC ANALYSIS OF THE VOLTAGE SOURCE INVERTER

The focus of this chapter is on the harmonic analysis of different types of voltage source inverters. The types of inverters analyzed in this chapter include: the six-step inverter, the sinusoidal PWM inverter, and the space vector PWM inverter. Methods for determining the harmonic content of the output waveforms of the sinusoidal PWM and the space vector PWM voltage source inverters are presented and can be used to conduct a harmonic analysis on an induction motor while supplied by a voltage source inverter. The waveforms analyzed in sections 2.1and 2.2 are typical voltage source inverter output waveforms produced by single-phase inverter topologies, while those analyzed in section 2.3 are typical waveforms produced by a three-phase voltage source inverter. The equations used to determine the harmonic content of the voltage source inverter output waveforms were coded in MATLAB and compared with PSPICE simulation models. The chapter concludes with a summary of the harmonic analysis techniques presented in the chapter.

2.1 The Sinusoidal PWM Inverter

A method to analyze the harmonic content of modulated pulses was first introduced by Bennett in 1933 [19]. Bennett's method and other methods based on Bennett's work used the double Fourier series to analyze the output PWM signal. Using a double

Fourier series to determine the harmonic components of the PWM output signal required the use of Jacobi-Anger expansions to establish closed form solutions. The end result of using Jacobi-Anger expansions was the appearance of Bessel functions in the final expression of the output PWM signal. Understanding and applying these methods can be cumbersome, leading to computer programming errors when attempting to implement a particular method. Methods that use the double Fourier series also result in final voltage expressions that typically contain three terms: one term to calculate the amplitude of the fundamental harmonic, one term to calculate the carrier frequency harmonic and harmonics of the carrier frequency, and another term to calculate the sideband frequency harmonics.

The purpose of this section is to present a method to calculate the harmonic components of the output voltage of a two-level and a three-level sinusoidal PWM inverter that is capable of being applied to various types of multilevel inverters and PWM schemes. This method allows direct calculation of harmonic magnitudes and angles without the use of linear approximations, iterative procedures, look-up tables, Bessel functions, or the gathering of harmonic terms. The method is valid in the overmodulation region (m_a>1.0) and has the potential to be extended to inverter-drive systems such as the one presented in [44].

2.1.1 The Two-Level PWM Inverter

In a two-level PWM inverter with sine-triangle modulation, a sinusoidal control signal at a desired output frequency is compared with a triangular waveform as shown in Figure 2.1. The control signal shown in Figure 2.1 can be expressed as:

$$v_{control}(t) = V_{con} \sin \omega_1 t \tag{2.1}$$

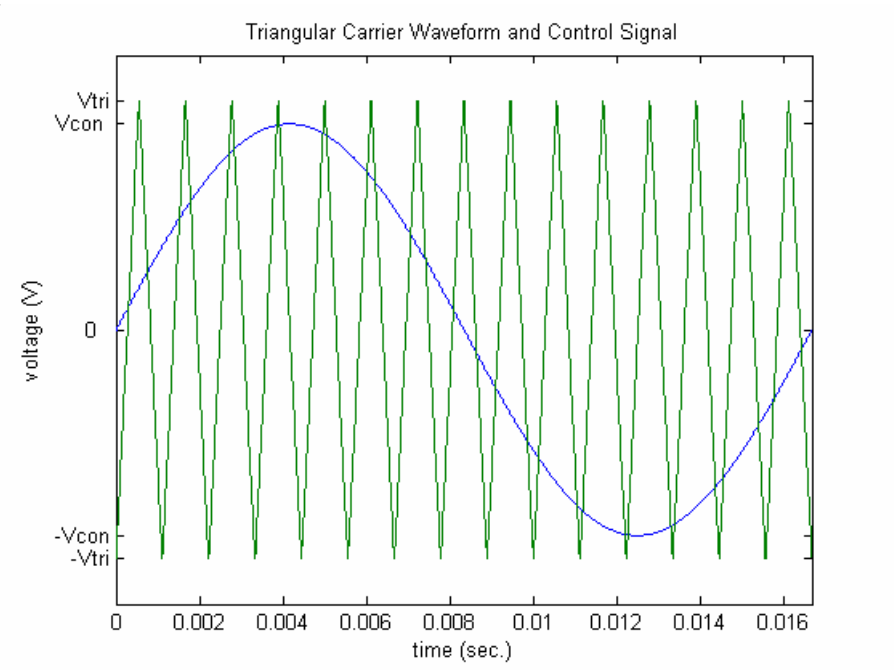

Figure 2.1: Triangular Waveform and Control Signal.

where V_{con} is the peak amplitude of the control signal and ω_1 is the angular frequency. The angular frequency is given as:

$$\omega_1 = 2\pi f_1 \tag{2.2}$$

where f_1 is the desired fundamental frequency of the inverter output. The triangular waveform $v_{triangle}$ in Figure 2.1 is normally kept at a constant frequency f_s and a constant amplitude V_{tri}. The frequency f_s is also known as the switching frequency or carrier frequency of the inverter. The amplitude modulation ratio is defined as:

$$m_a = \frac{V_{con}}{V_{tri}}. \tag{2.3}$$

The frequency modulation ratio is defined as:

$$m_f = \frac{f_s}{f_1}. \tag{2.4}$$

If the variables listed in (2.1-2.4) are known, the output PWM signal can be produced by comparing the waveforms shown in Figure 2.1. Referring to Figure 2.2, when $v_{control} > v_{triangle}$, T_{A+} and T_{B-} are closed and the value of the output PMW signal is $+V_i$ (where V_i is the DC input voltage of the inverter). When $v_{control} < v_{triangle}$, T_{A-} and T_{B+} are closed and the value of the output PWM signal becomes $-V_i$. As noted in [23], the output voltage of the inverter can be considered to be a voltage switching from $+V_i$ to $-V_i$. The output PWM signal produced from comparing the waveforms in Figure 2.1 is shown in Figure 2.3.

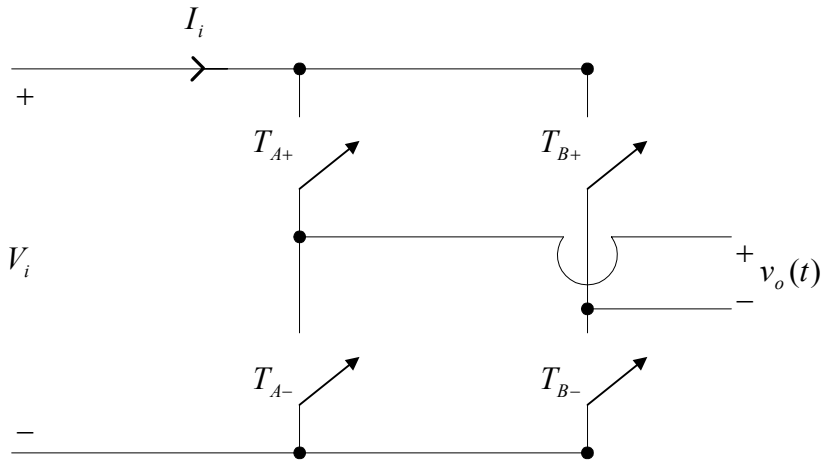

Figure 2.2: Single-Phase Inverter.

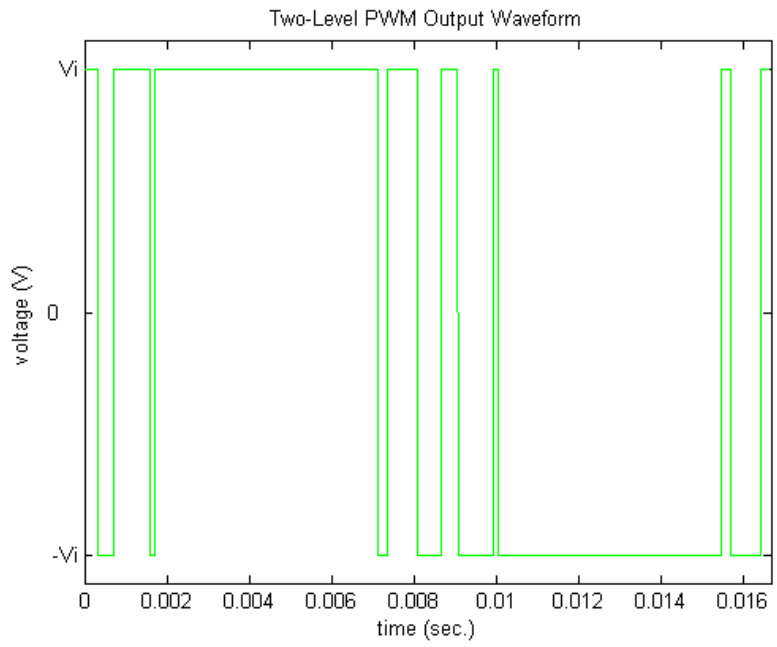

Figure 2.3: Two-Level PWM Output Waveform.

2.1.1.1 Harmonic Analysis of the Two-Level Inverter Using the Method of Pulse Pairs

It is desirable to find a general technique to calculate the harmonic components of a PWM waveform such as the one shown in Figure 2.3. To accomplish this task, it can be observed that the waveform in Figure 2.3 is made up of multiple positive and negative pulse pairs. Also, another observation that will be helpful in the derivation of the analysis technique presented is the fact that the waveform in Figure 2.3 possesses half-wave symmetry. This means that for each positive pulse during the first half of the period of the PWM signal, there is a corresponding negative pulse in the second half of the PWM signal period. This is illustrated by the arbitrary positive pulse pair shown in Figure 2.4 where A is the amplitude of the pulse, a_P is the initial time delay of the positive pulse, b_P is the pulse width of the positive pulse, and T is the period of the

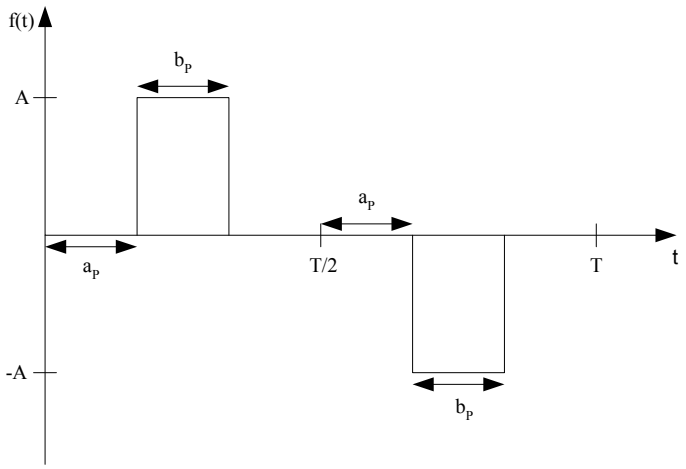

Figure 2.4: Positive Pulse Pair.

PWM waveform. For each negative pulse in the first half of the PWM signal period, there is a corresponding positive pulse in the second half of the period. This is illustrated by the arbitrary negative pulse pair shown in Figure 2.5. In this figure, a_N is the initial time delay of the negative pulse, and b_N is the pulse width of the negative pulse.

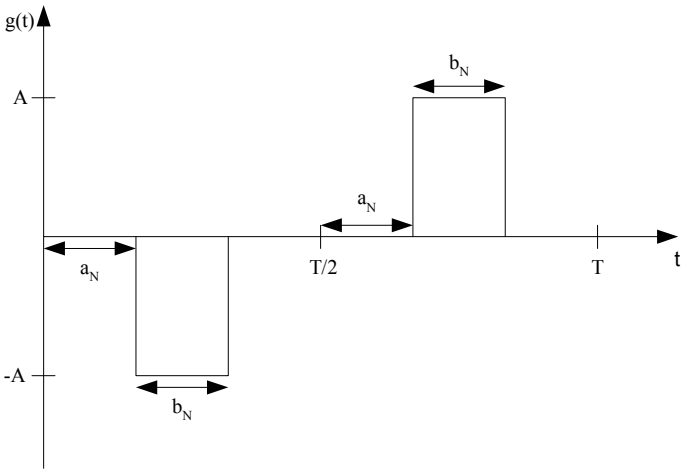

Figure 2.5: Negative Pulse Pair.

The first step in the analysis is to find the trigonometric Fourier series of the waveform shown in Figure 2.4. Since it is known that the waveform in Figure 2.3 has half-wave symmetry, the Fourier coefficient a_0 is zero. This is due to the fact that the average value of a function with half-wave symmetry is always zero. The Fourier coefficients a_n and b_n are also zero for n even due to half-wave symmetry. Using the above simplifications, the trigonometric Fourier series of the function *f(t)* shown in Figure 2.4 can be expressed as:

$$f(t) = \sum_{\substack{n=1 \\ n\ odd}}^{\infty} \left(a_{n_{POS}} \cos\frac{2\pi n}{T}\, t + b_{n_{POS}} \sin\frac{2\pi n}{T}\, t \right) \tag{2.5}$$

where $a_{n_{POS}}$ and $b_{n_{POS}}$ are the Fourier coefficients of the positive pulse pair. The coefficient $a_{n_{POS}}$ can be found from Figure 2.4 as follows:

$$a_{n_{POS}} = \frac{2}{T}\int_0^T f(t)\cos\frac{2\pi n}{T} t\ dt\,, \tag{2.6}$$

$$a_{n_{POS}} = \frac{2}{T}\int_{a_P}^{a_P+b_P} (A)\cos\frac{2\pi n}{T} t\ dt + \frac{2}{T}\int_{\frac{T}{2}+a_P}^{\frac{T}{2}+a_P+b_P} (-A)\cos\frac{2\pi n}{T} t\ dt\,. \tag{2.7}$$

Integrating (2.7) and using the identity $\sin\alpha - \sin\beta = 2\cos 1/2(\alpha+\beta)\ \sin 1/2(\alpha-\beta)$, (2.7) becomes:

$$\begin{aligned} a_{n_{POS}} &= \frac{2A}{\pi n}\left[\cos\left(\frac{2\pi n}{T}a_P + \frac{\pi n}{T}b_P\right)\sin\left(\frac{\pi n}{T}b_P\right)\right] \\ &\quad -\frac{2A}{\pi n}\left[\cos\left(\pi n + \frac{2\pi n}{T}a_P + \frac{\pi n}{T}b_P\right)\sin\left(\frac{\pi n}{T}b_P\right)\right]. \end{aligned} \tag{2.8}$$

The coefficient $b_{n_{POS}}$ can be found from Figure 2.4 as follows:

$$b_{n_{POS}} = \frac{2}{T}\int_0^T f(t)\sin\frac{2\pi n}{T}t\ dt, \tag{2.9}$$

$$b_{n_{POS}} = \frac{2}{T}\int_{a_P}^{a_P+b_P} A\sin\frac{2\pi n}{T}t\ dt + \frac{2}{T}\int_{\frac{T}{2}+a_P}^{\frac{T}{2}+a_P+b_P}(-A)\sin\frac{2\pi n}{T}t\ dt. \tag{2.10}$$

Integrating (2.10), using the identity cos α-cos β = -2sin 1/2(α+β) sin 1/2(α-β), and using the fact that sin(-θ) = -sin θ, (2.10) becomes:

$$\begin{aligned} b_{n_{POS}} &= \frac{2A}{\pi n}\left[\sin\left(\frac{2\pi n}{T}a_P + \frac{\pi n}{T}b_P\right)\sin\left(\frac{\pi n}{T}b_P\right)\right] \\ &\quad -\frac{2A}{\pi n}\left[\sin\left(\pi n + \frac{2\pi n}{T}a_P + \frac{\pi n}{T}b_P\right)\sin\left(\frac{\pi n}{T}b_P\right)\right]. \end{aligned} \tag{2.11}$$

Equations (2.8) and (2.11) can now be substituted into (2.5) and the trigonometric Fourier series of the waveform *f(t)* is established. The trigonometric Fourier series of the waveform *g(t)* shown in Figure 2.5 is the same as the waveform *f(t)* in Figure 2.4 except that the magnitudes are the negative of each other. The Fourier coefficients for *g(t)* are as follows:

$$\begin{aligned} a_{n_{NEG}} &= -\frac{2A}{\pi n}\left[\cos\left(\frac{2\pi n}{T}a_N + \frac{\pi n}{T}b_N\right)\sin\left(\frac{\pi n}{T}b_N\right)\right] \\ &\quad +\frac{2A}{\pi n}\left[\cos\left(\pi n + \frac{2\pi n}{T}a_N + \frac{\pi n}{T}b_N\right)\sin\left(\frac{\pi n}{T}b_N\right)\right], \end{aligned} \tag{2.12}$$

$$b_{n_{NEG}} = -\frac{2A}{\pi n}\left[\sin\left(\frac{2\pi n}{T}a_N + \frac{\pi n}{T}b_N\right)\sin\left(\frac{\pi n}{T}b_N\right)\right] + \frac{2A}{\pi n}\left[\sin\left(\pi n + \frac{2\pi n}{T}a_N + \frac{\pi n}{T}b_N\right)\sin\left(\frac{\pi n}{T}b_N\right)\right], \tag{2.13}$$

where $a_{n_{NEG}}$ and $b_{n_{NEG}}$ are the Fourier coefficients of the negative pulse pair. The trigonometric Fourier series for *g(t)* can be expressed in the same form as *f(t)* in (2.5):

$$g(t) = \sum_{\substack{n=1 \\ n\ odd}}^{\infty}\left(a_{n_{NEG}}\cos\frac{2\pi n}{T}\,t + b_{n_{NEG}}\sin\frac{2\pi n}{T}\,t\right). \tag{2.14}$$

Because the Fourier series of arbitrary positive and negative pulse pairs has been established, the Fourier series of a given PWM signal produced by two-level modulation can be found by application of the principle of superposition. A PWM waveform like the one in Figure 2.3 is made up of the sum of positive and negative pulse pairs as shown in Figure 2.6 where P1-P3 in the figure are positive pulse pairs and N1-N3 are negative pulse pairs. All that is required to find the Fourier series of a signal like the one shown in Figure 2.6 is to find the Fourier coefficients of each individual positive and negative pulse pair contained in the PWM signal and add them to get the Fourier coefficients of the entire PWM signal. The total a_n and b_n coefficients of the entire PWM signal can be found using (2.8) and (2.11-2.13) as follows:

$$a_n = \sum_{\substack{n=1 \\ n\ odd}}^{\infty}\sum_{j=1}^{K}\left(a_{n_{NEG_j}} + a_{n_{POS_j}}\right), \tag{2.15}$$

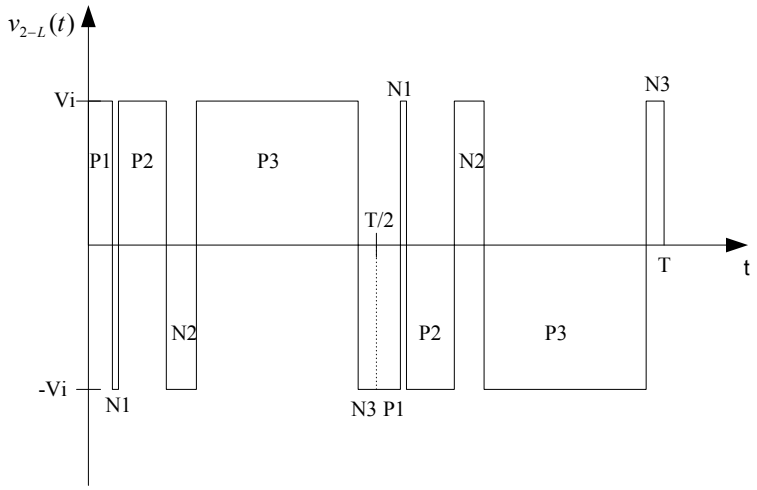

Figure 2.6: PWM Output Signal with Positive and Negative Pulse Pairs Labeled.

$$b_n = \sum_{\substack{n=1 \\ n\ odd}}^{\infty} \sum_{j=1}^{K} \left(b_{n_{NEG_j}} + b_{n_{POS_j}} \right), \tag{2.16}$$

where K is the number of positive or negative pulse pairs (Note: the number of positive pulse pairs will equal the number of negative pulse pairs due to symmetry.). The Fourier series of a given PWM signal produced by two-level modulation can be expressed in a single-cosine series as:

$$v_{2-L}(t) = \sum_{\substack{n=1 \\ n\ odd}}^{\infty} C_n \cos\left(\frac{2\pi n}{T} t + \delta_n \right) \tag{2.17}$$

where $C_n = \sqrt{a_n^2 + b_n^2}$ and $\delta_n = \tan^{-1}\left(-\frac{b_n}{a_n} \right)$. It should be noted that the subscript 2-L in (2.17) stands for two-level.

The final step in implementing this method is to find the crossing points of the waveforms shown in Figure 2.2 that determine the edges of the PWM signal pulses. In order to determine the crossing points, an equation for the triangular wave in Figure 2.2 must be established. The signal can be thought of as being made up of straight lines having alternating positive and negative slopes with shifted intercepts on the time axis. To implement this idea in a computer software package, the triangular waveform can be expressed as:

$$V_{triangle}(n,t) = (-1)^{n+1}\left(\frac{4V_{tri}}{T_s}\right)t + (-1)^{n+2}\left(V_{tri} + 2V_{tri}(n-1)\right) \tag{2.18}$$

where n is the index number used in a computer program and T_s is the period of the triangular wave. Since the PWM signal has half-wave symmetry, only the crossing points that occur in the first half of the PWM signal period need to be considered when using the method of pulse pairs. To find the crossing points, set $v_{control} = v_{triangle}$ and solve the transcendental equation for t. To easily solve the transcendental equation in MATLAB, declare t as a symbolic object using the *syms* command. The *solve* command can then be used to find the crossing points. However, the use of (2.18) results in some special cases where crossing points occur above the peak amplitude V_{tri} of the triangular wave as shown in Figure 2.7. These special cases occur due to the fact that the straight lines used to represent the triangular signal extend beyond the value of V_{tri}

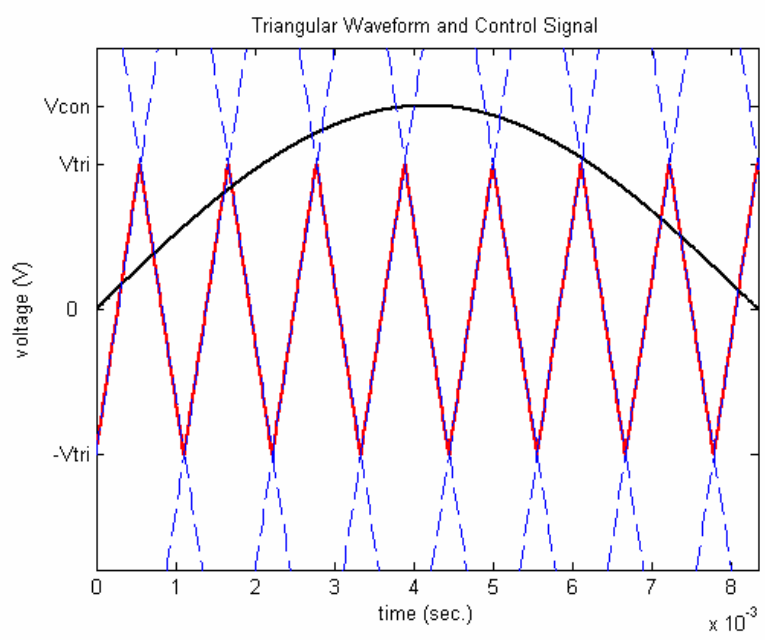

Figure 2.7: Special Case Crossing Points.

and will intersect the control signal at crossing points that are undesired. These undesired points can be eliminated using the *find* command in MATLAB, leaving the crossing points that determine the edges of the PWM signal pulses. At this point, the only requirement to implement the method of pulse pairs is to use the crossing points to determine the time delays and the pulse widths.

2.1.1.2 Simulation Results for the Two-Level PWM Inverter

The equations of the control signal, the carrier waveform, and the equations used to implement the method of pulse pairs were coded in MATLAB for the purpose of computing the harmonic components of a PWM signal such as the one shown in Figure 2.3. MATLAB code was also written to find the crossing points, time delays, and pulse widths. Four MATLAB simulations were conducted using different values of m_a and m_f.

The following parameter values were used for all simulations: V_i = 270 V, V_{tri} = 10 V, and f_1 = 60 Hz. The other parameters used for the first simulation were as follows: V_{con} = 3 V and f_s = 540 Hz. The parameters used for the second MATLAB simulation were: V_{con} = 6 V and f_s = 900 Hz. The parameters used for the third simulation were: V_{con} = 14 V and f_s = 900 Hz. The fourth simulation was conducted using the following parameters: V_{con} = 22 V and f_s = 1.5 kHz.

PSPICE was used to verify the results from the MATLAB calculations by constructing a two-level PWM simulation model. A PSPICE ABM block was used to compare the sinusoidal control signal and the triangular carrier wave. A Fourier analysis was then performed in PSPICE on the PWM output signal of the ABM block. The parameters used in the PSPICE simulations were the same as the ones used in the four MATLAB simulations.

Results of the MATLAB and PSPICE simulations are shown in Tables 2.1-2.4. The results shown in Table 2.1 and Table 2.2 are for dominant carrier frequency and sideband harmonics. Because the results shown in Table 2.3 and Table 2.4 are for simulations conducted in the overmodulation region, all harmonics up to the 31st harmonic were included. The harmonic number of individual sidebands can be found using the following formula [27]:

$$h = pm_f \pm q \tag{2.19}$$

where p and q are integers. When p is odd, sideband harmonics exist only for even values of q. When p is even, sideband harmonics exist only for odd values of q. The use of (2.19) is not required when applying the method of pulse pairs and is provided here as

TABLE 2.1

MATLAB AND PSPICE RESULTS FOR m_a=0.3 and m_f=9

Harmonic Number	Voltage Magnitude (PSPICE)	Voltage Magnitude (MATLAB)	ΔV	Voltage Angle (PSPICE)	Voltage Angle (MATLAB)	Δθ
1	81.03	80.999	0.031	-0.030	0.0006	0.03049
7	9.395	9.3652	0.0298	90.190	90.0002	0.1898
9	324.9	324.9511	0.0511	89.910	90.0001	0.0901
11	9.362	9.3652	0.0032	89.980	90.0077	0.0277
25	24.18	24.1504	0.0296	-90.130	269.9971	0.1271
27	64.07	64.1064	0.0364	-90.260	-89.9995	0.2605
29	24.17	24.1504	0.0196	-90.370	269.9822	0.3522
35	49.96	49.9735	0.0135	179.600	180.0004	0.4004
37	49.98	49.9735	0.0065	-0.382	0.0057	0.388
41	4.187	4.1754	0.0116	83.030	83.7006	0.6706
43	29.14	29.1326	0.0074	89.620	89.9774	0.3574
45	1.728	1.7524	0.0244	90.210	89.9252	0.2848
53	22.92	22.9487	0.0287	-0.556	0.002	0.5578
55	22.93	22.9487	0.0187	179.600	180.1294	0.5294
57	15.95	15.942	0.008	-177.400	183.3271	0.7271

TABLE 2.2

MATLAB AND PSPICE RESULTS FOR m_a=0.6 and m_f=15

Harmonic Number	Voltage Magnitude (PSPICE)	Voltage Magnitude (MATLAB)	ΔV	Voltage Angle (PSPICE)	Voltage Angle (MATLAB)	Δθ
1	162	161.9981	0.0019	0.003	0.0013	0.001369
13	35.38	35.4205	0.0405	89.830	89.9971	0.1671
15	271.5	271.5686	0.0686	89.850	90.0002	0.1502
17	35.45	35.4205	0.0295	89.790	90.0056	0.2156
27	19.1	19.1058	0.0058	-0.394	-0.0128	0.3815
29	99.99	99.947	0.043	-0.306	-0.0033	0.303
31	99.93	99.947	0.017	179.700	180.0033	0.3033
33	19.17	19.1058	0.0642	179.7	180.0125	0.3125
41	12.63	12.606	0.024	-90.72	269.9957	0.7157
43	54.94	54.9466	0.0066	-90.45	269.9967	0.4467
45	22.52	22.4717	0.0483	89.62	89.9978	0.3778
47	54.9	54.9466	0.0466	-90.47	-89.9949	0.4751
49	12.57	12.6061	0.0361	-90.77	-89.9948	0.7752

TABLE 2.3

MATLAB AND PSPICE RESULTS FOR m_a=1.4 and m_f=15

Harmonic Number	Voltage Magnitude (PSPICE)	Voltage Magnitude (MATLAB)	ΔV	Voltage Angle (PSPICE)	Voltage Angle (MATLAB)	Δθ
1	311.8	311.8012	0.0012	-0.239	-0.2342	0.0047
3	39.2	39.2488	0.0488	3.519	3.5087	0.0103
5	8.765	8.7275	0.0375	176.100	176.1209	0.0209
7	7.559	7.5407	0.0183	-132.400	227.4985	0.1015
9	4.01	4.0148	0.0048	33.060	33.788	0.728
11	37.26	37.2808	0.0208	87.700	87.8266	0.1266
13	83.63	83.6026	0.0274	91.390	91.5182	0.1282
15	105.4	105.3281	0.0719	89.820	89.9667	0.1467
17	83.65	83.6208	0.0292	88.310	88.4674	0.1574
19	37.29	37.2907	0.0007	92.430	92.5775	0.1475
21	3.731	3.7163	0.0147	143.900	143.55	0.35
23	12.49	12.51	0.02	-26.680	-26.3705	0.3095
25	35.1	35.0952	0.0048	0.798	1.0319	0.2341
27	43.54	43.5175	0.0225	2.872	3.131	0.259
29	20.07	20.0505	0.0195	-4.290	-3.9921	0.2979
31	20.02	20.0147	0.0053	-176.800	183.4837	0.2837

TABLE 2.4

MATLAB AND PSPICE RESULTS FOR m_a=2.2 and m_f=25

Harmonic Number	Voltage Magnitude (PSPICE)	Voltage Magnitude (MATLAB)	ΔV	Voltage Angle (PSPICE)	Voltage Angle (MATLAB)	Δθ
1	331.5	331.5119	0.0119	-0.187	-0.1964	0.0091
3	80.94	80.8832	0.0568	0.163	0.1361	0.0273
5	21.78	21.7184	0.0616	4.276	4.2415	0.0345
7	2.064	2.0923	0.0283	130.800	131.7061	0.9061
9	7.324	7.3304	0.0064	-176.100	183.8417	0.0583
11	5.917	5.8938	0.0232	-146.200	213.9363	0.1363
13	4.024	4.0355	0.0115	-96.410	264.1293	0.5393
15	2.304	2.3063	0.0023	10.570	9.7675	0.8025
17	11.69	11.6474	0.0426	79.240	79.4863	0.2463
19	27.94	27.9149	0.0251	89.070	89.3683	0.2983
21	45.75	45.7661	0.0161	91.260	91.5431	0.2831
23	59.53	59.573	0.043	90.930	91.2003	0.2703
25	64.71	64.7653	0.0553	89.700	89.9511	0.2511
27	59.55	59.5887	0.0387	88.470	88.7123	0.2423
29	45.77	45.7829	0.0129	88.230	88.4476	0.2176

an aid in determining sideband harmonic numbers for the example simulations shown in Tables 2.1-2.4. Most techniques that use the double Fourier series approach must include a term in the final PWM output voltage expression dedicated to calculating sideband harmonics that requires (2.19). The harmonic spectrum of a PWM inverter output voltage waveform with m_a=1.0 and m_f=25 is shown in Figure 2.8 for the first 80 harmonics. The white bars on the graph in Figure 2.8 are PSPICE results and the gray bars on the graph are results from the derived equations that were coded in MATLAB.

The harmonic components found using the equations coded in MATLAB are similar to the ones found using the PSPICE model as illustrated by the results in the tables and Figure 2.8. These results show that the method of pulse pairs is an accurate method used to find the harmonic components of a two-level PWM inverter output waveform.

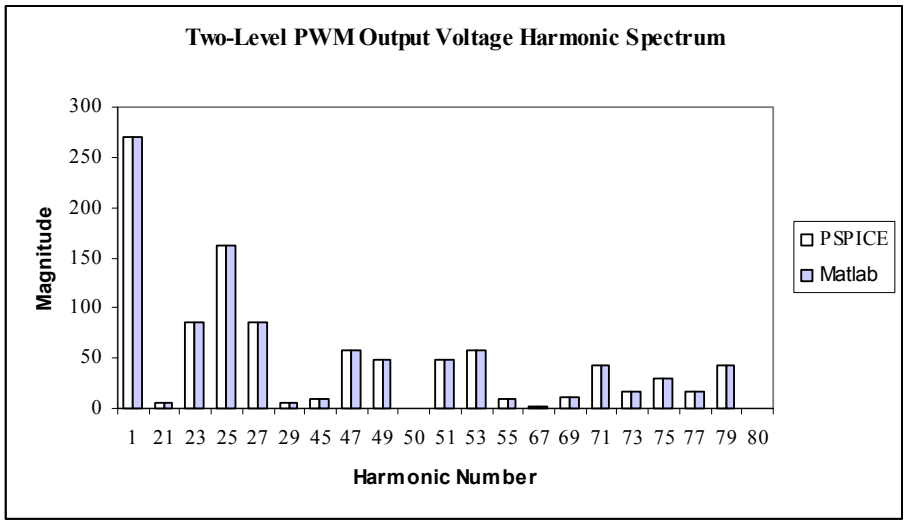

Figure 2.8: Harmonic Spectrum with m_a=1.0 and m_f=25.

2.1.2 The Three-Level PWM Inverter

In a three-level PWM inverter with sinusoidal modulation, a control signal at a desired output frequency is compared with a multi-level triangular waveform as shown in Figure 2.9. The control signal shown in Figure 2.9 can be expressed the same as (2.1). It should be noted that the carrier signal in Figure 2.9 is a different carrier signal than the one used for the two-level case in Figure 2.1. Therefore, a new notation for the carrier waveform is needed. The triangular waveform in Figure 2.9 will be referred to as $v_{carrier}$ and the amplitude of the carrier waveform will be denoted as V_{car}. The amplitude modulation ratio is defined as:

$$m_a = \frac{V_{con}}{V_{car}} \ . \tag{2.20}$$

The frequency modulation ratio is defined the same as in (2.4).

If the variables listed in (2.1, 2.2, 2.4, and 2.20) are known, the output PWM signal can be produced by comparing the waveforms shown in Figure 2.9. The switches in Figure 2.2 are controlled based on the following conditions: $v_{control}<v_{tri}$: T_{A-} is closed, $v_{control}<-v_{tri}$: T_{B+} is closed, $v_{control}>v_{tri}$: T_{A+} is closed, and when $v_{control}>-v_{tri}$: T_{B-} is closed. It should be noted that V_{tri} is the upper half of the carrier waveform and $-V_{tri}$ is the lower half of the carrier waveform in Figure 2.9. Referring to Figure 2.2, when T_{A+} and T_{B-} are closed, the value of the output PMW signal is $+V_i$. When T_{A-} and T_{B+} are closed in Figure 2.2, the value of the output PWM signal is $-V_i$. When T_{A+} and T_{B+} are closed or when T_{A-} and T_{B-} are closed, the value of the output PWM signal is zero. A three-level PWM output waveform such as the one shown in Figure 2.10 can also be generated by comparing a triangular carrier waveform with a sinusoidal control signal and the negative

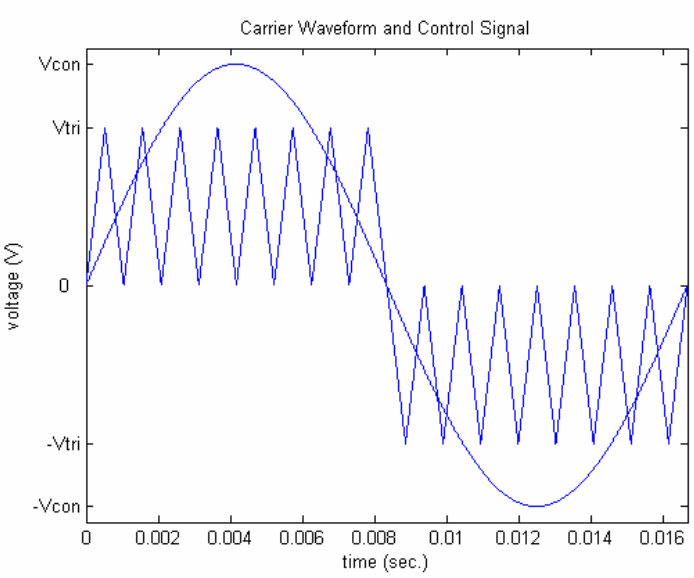

Figure 2.9: Carrier Waveform and Control Signal.

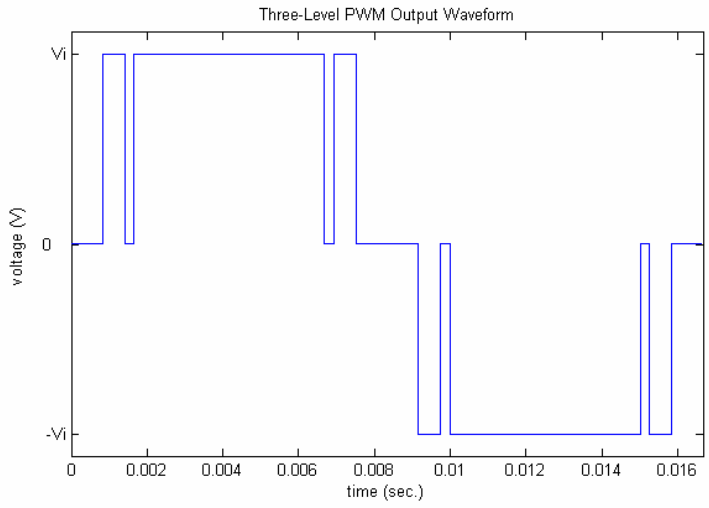

Figure 2.10: Three-Level PWM Output Waveform.

of the sinusoidal control signal as described in [27]. This alternative method of generating a three-level PWM output signal is shown in Figure 2.11.

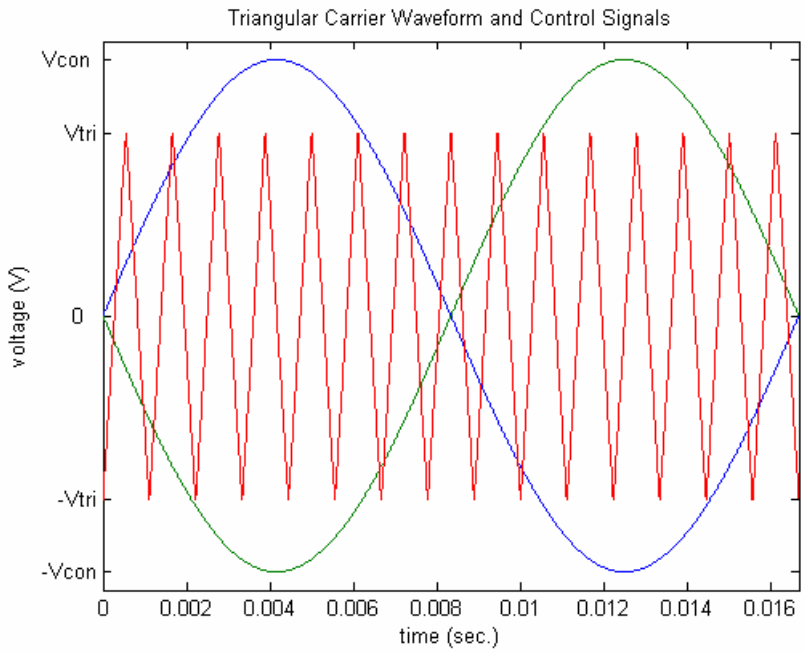

Figure 2.11: Three-Level PWM Alternative Method.

2.1.2.1 Harmonic Analysis of the Three-Level Inverter Using the Method of Pulse Pairs

A technique can be found to calculate the harmonic components of the PWM waveform shown in Figure 2.10 that is simple and easy to implement in a computer software package such as MATLAB. It can be observed that the waveform in Figure 2.10 is made up of multiple positive pulse pairs. This waveform also possesses half-wave symmetry. This means that for each positive pulse during the first half of the period of

the PWM signal, there is a corresponding negative pulse in the second half of the PWM signal period. This is illustrated by the arbitrary positive pulse pair shown in Figure 2.12 where A in the figure is the amplitude of the pulse, a_P is the initial time delay of the positive pulse, b_P is the pulse width of the positive pulse, and T is the period of the PWM waveform.

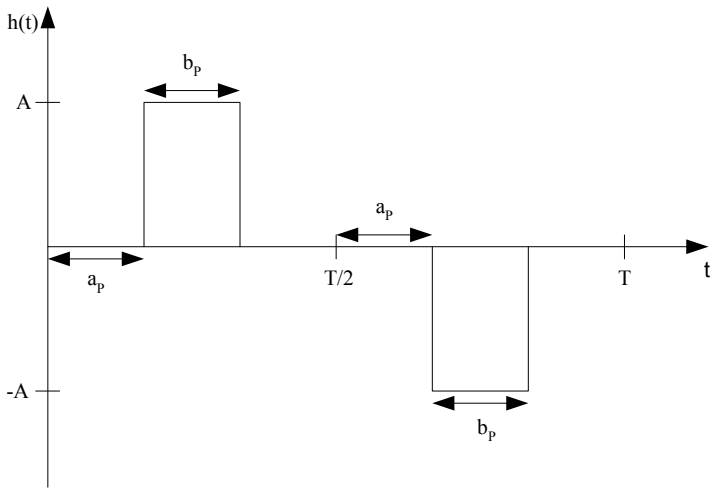

Figure 2.12: Positive Pulse Pair.

The first step in the analysis is to find the trigonometric Fourier series of the waveform shown in Figure 2.12. Because it is known that the waveform in Figure 2.10 has half-wave symmetry, the Fourier coefficient a_0 is zero. The trigonometric Fourier series of the function $h(t)$ shown in Figure 2.12 can be expressed as:

$$h(t) = \sum_{\substack{n=1 \\ n\ odd}}^{\infty} \left(a_{n_{POS}} \cos\frac{2\pi n}{T} t + b_{n_{POS}} \sin\frac{2\pi n}{T} t \right) \tag{2.21}$$

where $a_{n_{POS}}$ and $b_{n_{POS}}$ are the Fourier coefficients of the positive pulse pair. The

coefficients $a_{n_{POS}}$ and $b_{n_{POS}}$ can be found using (2.6-2.11). The Fourier coefficients can then be substituted into (2.21) and the trigonometric Fourier series of the waveform *h(t)* is established.

Because the Fourier series of an arbitrary positive pulse pair has been established in (2.21), the Fourier series of a given PWM signal produced by three-level modulation can be found by application of the principle of superposition. A PWM waveform like the one in Figure 2.10 is made up of the sum of positive pulse pairs as shown in Figure 2.13 where P1-P3 in the figure are positive pulse pairs. All that is required to find the Fourier series of the signal in Figure 2.13 is to find the Fourier coefficients of each individual positive pulse pair contained in the PWM signal and add them to get the Fourier coefficients of the entire PWM signal. The total a_n and b_n coefficients of the entire PWM signal can be found using (2.8) and (2.11) as follows:

$$a_n = \sum_{\substack{n=1 \\ n\ odd}}^{\infty} \sum_{j=1}^{K_P} \left(a_{n_{POS_j}} \right), \tag{2.22}$$

$$b_n = \sum_{\substack{n=1 \\ n\ odd}}^{\infty} \sum_{j=1}^{K_P} \left(b_{n_{POS_j}} \right), \tag{2.23}$$

where K_P is the number of positive pulse pairs. The Fourier series of a given PWM signal produced by three-level modulation can be expressed in a single cosine series as:

$$v_{3-L}(t) = \sum_{\substack{n=1 \\ n\ odd}}^{\infty} D_n \cos\left(\frac{2\pi n}{T} t + \gamma_n \right) \tag{2.24}$$

where $D_n = \sqrt{a_n^2 + b_n^2}$ and $\gamma_n = \tan^{-1}\left(-\frac{b_n}{a_n} \right)$. The subscript 3-L in (2.24) stands for three-level.

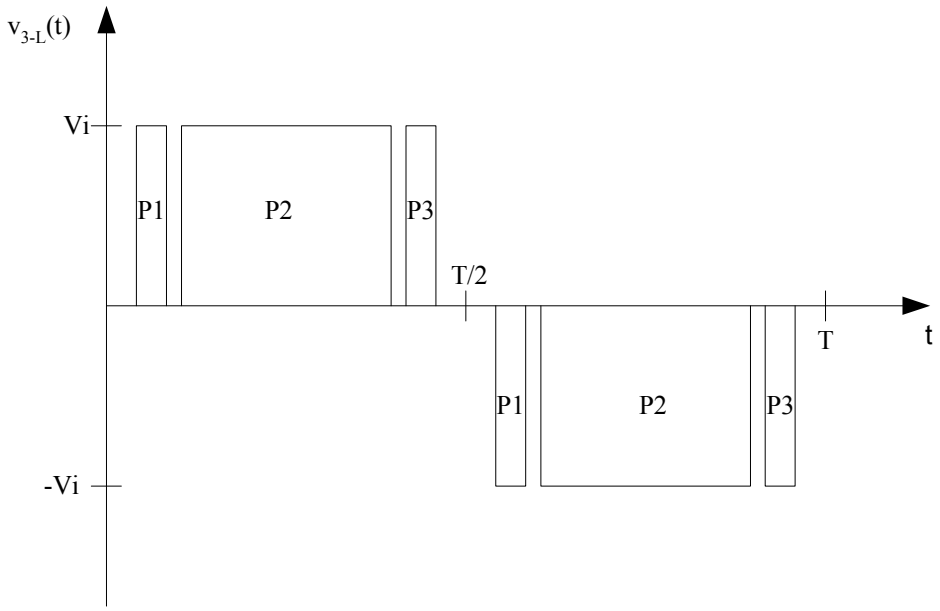

Figure 2.13: PWM Output Signal with Pulse Pairs Labeled.

The final step in implementing this method is to find the crossing points of the waveforms shown in Figure 2.9 that determine the edges of the PWM signal pulses. In order to determine the crossing points, an equation for the carrier wave in Figure 2.9 must be established. The signal can be thought of as being made up of straight lines having alternating positive and negative slopes with shifted intercepts on the time axis in the first half cycle of the control signal. To implement this idea in a computer software package, the carrier waveform can be expressed as:

$$V_{carrier}(1,t) = \left(\frac{2V_{car}}{T_s}\right)t\,, \tag{2.25}$$

$$V_{carrier}(m,t) = \left(\frac{-2V_{car}}{T_s}\right)t + mV_{car}\,;m \text{ even}, \tag{2.26}$$

$$V_{carrier}(n,t) = \left(\frac{2V_{car}}{T_s}\right)t - (n-1)V_{car} \;;n \text{ odd}, \tag{2.27}$$

where m and n are index numbers used in a computer program, and T_s is the period of the triangular wave. Because the PWM signal has half-wave symmetry, only the crossing points that occur in the first half of the PWM signal period need consideration when using the method of pulse pairs. To find the crossing points, set $v_{control} = v_{carrier}$ and solve the transcendental equation for t using MATLAB. Special cases exist as shown in Figure 2.14.

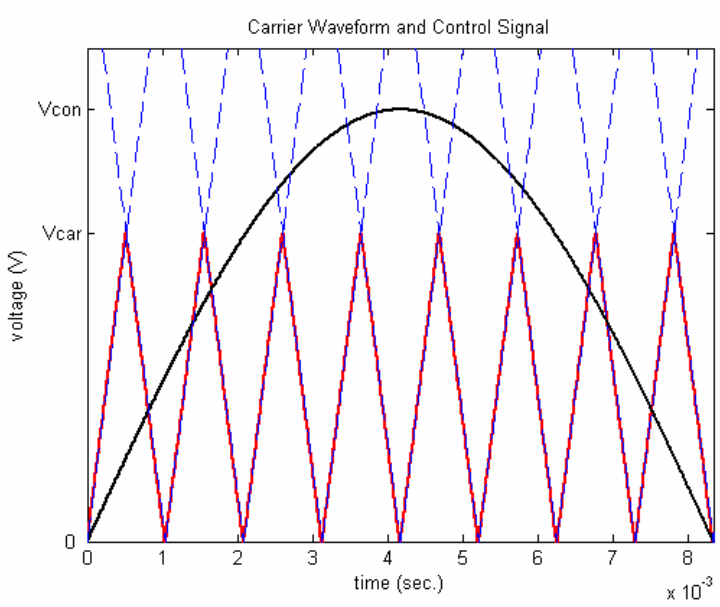

Figure 2.14: Special Case Crossing Points.

2.1.2.2 Simulation Results for the Three-Level PWM Inverter

The equations of the control signal, the carrier waveform, and the equations used to implement the method of pulse pairs were coded in MATLAB for the purpose of computing the harmonic components of a PWM signal such as the one shown in Figure

2.10. MATLAB code was also written to find the crossing points, time delays, and pulse widths. Four MATLAB simulations were conducted using different values of m_a and m_f. The following parameter values were used for all simulations: V_l=270 V, V_{car}=10 V, and f_l=60 Hz. The other parameters used for the first simulation were as follows: V_{con}= 8V and f_s=600 Hz. The parameters used for the second MATLAB simulation were: V_{con}=14V and f_s=960 Hz. The parameters used for the third simulation were: V_{con}=18 V and f_s=1.2 kHz. The fourth simulation was conducted using the following parameters: V_{con}=22 V and f_s=1.2 kHz.

PSPICE was used to verify the results from the MATLAB calculations by constructing a three-level PWM simulation model. A PSPICE ABM block was used to compare the sinusoidal control signal and the multi-level triangular carrier wave. A Fourier analysis was then performed in PSPICE on the PWM output signal of the ABM block. The parameters used in the PSPICE simulations were the same as the ones used in the four MATLAB simulations.

Results of the MATLAB and PSPICE simulations are shown in Tables 2.5-2.8. The results shown in these tables include all harmonics up to the 31st harmonic. The harmonic spectrum of a PWM inverter output voltage waveform with m_a=0.9 and m_f=16 is shown in Figure 2.15 for the first 61 harmonics. The white bars on the graph in Figure 2.15 are PSPICE results and the gray bars on the graph are results from the derived equations that were coded in MATLAB.

TABLE 2.5
MATLAB AND PSPICE RESULTS FOR m_a=0.8 and m_f=10

	Voltage	Voltage		Voltage	Voltage	
Harmonic	**Magnitude**	**Magnitude**	**ΔV**	**Angle**	**Angle**	**Δθ**
Number	(PSPICE)	(MATLAB)		(PSPICE)	(MATLAB)	
1	215.8	215.9948	0.1948	-0.012	0.0012	0.0132
7	37.59	37.6563	0.0663	179.900	179.9988	0.0988
9	84.96	84.9067	0.0533	179.900	180.0002	0.1002
11	84.46	84.382	0.078	-0.148	-0.0001	0.1477
13	32.93	32.9386	0.0086	-0.239	0.0035	0.2422
15	19.32	19.3161	0.0039	179.600	179.9957	0.3957
17	31.02	30.9192	0.1008	179.900	179.9998	0.0998
19	27.46	27.4984	0.0384	-0.304	-0.0085	0.2954
21	33.53	33.6488	0.1188	179.700	180.0046	0.3046
23	14.63	14.5081	0.1219	-0.134	0.017	0.1512
27	18.4	18.4752	0.0752	-0.200	-0.01	0.1899
29	13.18	13.2756	0.0956	179.800	180.0031	0.2031
31	4.428	4.376	0.052	179.500	179.9848	0.4848

TABLE 2.6
MATLAB AND PSPICE RESULTS FOR m_a=1.4 and m_f=16

	Voltage	Voltage		Voltage	Voltage	
Harmonic	**Magnitude**	**Magnitude**	**ΔV**	**Angle**	**Angle**	**Δθ**
Number	(PSPICE)	(MATLAB)		(PSPICE)	(MATLAB)	
1	310	310.1109	0.1109	-0.018	0.0014	0.0193
3	37.36	37.4979	0.1379	0.005	0.0012	0.0040
5	6.103	6.0378	0.0652	179.400	180.0546	0.6546
7	2.777	2.8288	0.0518	179.500	180.1123	0.6123
9	8.475	8.5533	0.0783	-179.700	180.0023	0.2977
11	32.62	32.6266	0.0066	-180.000	179.9948	0.0052
13	45.23	45.1691	0.0609	179.900	179.9989	0.0989
15	21.71	21.6852	0.0248	179.700	180.008	0.3080
17	21.85	21.7923	0.0577	-0.077	-0.0083	0.0690
19	44.53	44.445	0.085	-0.220	0.0015	0.2211
21	27.06	27.0322	0.0278	-0.288	0.0112	0.2996
23	7.486	7.4276	0.0584	179.700	179.9614	0.2614
25	22.21	22.1277	0.0823	179.600	179.9976	0.3976
27	8.243	8.2003	0.0427	179.600	180.0215	0.4215
29	9.591	9.5887	0.0023	-0.527	-0.0266	0.5003
31	6.533	6.5106	0.0224	-0.748	-0.0297	0.7187

TABLE 2.7
MATLAB AND PSPICE RESULTS FOR m_a=1.8 and m_f=20

Harmonic Number	Voltage Magnitude (PSPICE)	Voltage Magnitude (MATLAB)	ΔV	Voltage Angle (PSPICE)	Voltage Angle (MATLAB)	Δθ
1	323.9	324.0214	0.1214	-0.001	0.0016	0.0028
3	63.97	64.1346	0.1646	0.008	0.0031	0.0044
5	7.55	7.6989	0.1489	0.131	-0.0262	0.1575
7	5.1	5.0645	0.0355	180.000	180.0812	0.0812
9	4.785	4.8727	0.0877	-179.700	180.0647	0.235
11	8.907	9.0402	0.1332	-179.700	180.0037	0.296
13	21.08	21.1577	0.0777	-180.000	179.9912	0.009
15	32.33	32.3006	0.0294	179.900	179.9946	0.0946
17	30.68	30.5728	0.1072	179.900	180.0012	0.1012
19	12.55	12.4589	0.0911	179.800	180.0195	0.2195
21	12.98	12.9781	0.0019	-0.113	-0.0196	0.0933
23	30.45	30.3457	0.1043	-0.174	-0.0013	0.1731
25	29.61	29.4787	0.1313	-0.177	0.0086	0.1854
27	13.05	12.9782	0.0718	-0.062	0.0317	0.09339
29	6.237	6.1935	0.0435	179.300	179.9469	0.6469
31	15.05	14.9172	0.1328	179.600	179.9953	0.3953

TABLE 2.8
MATLAB AND PSPICE RESULTS FOR m_a=2.2 and m_f=20

Harmonic Number	Voltage Magnitude (PSPICE)	Voltage Magnitude (MATLAB)	ΔV	Voltage Angle (PSPICE)	Voltage Angle (MATLAB)	Δθ
1	334.3	334.3343	0.0343	-0.009	0.0019	0.0114
3	87.19	87.3399	0.1499	-0.034	0.0025	0.0362
5	26.6	26.7078	0.1078	-0.081	-0.0104	0.07055
7	3.268	3.2849	0.0169	-179.800	180.1529	-0.0471
9	19.23	19.3552	0.1252	179.900	180.0165	0.1165
11	26.1	26.2223	0.1223	179.900	179.9973	0.0973
13	26.27	26.2904	0.0204	179.800	179.9883	0.1883
15	21.58	21.4839	0.0961	179.800	179.9916	0.1916
17	13.83	13.6935	0.1365	179.800	180.0146	0.2146
19	4.882	4.8219	0.0601	179.900	180.1015	0.2015
21	3.428	3.3572	0.0708	-0.465	-0.1208	0.3441
23	9.581	9.4353	0.1457	-0.284	0.0037	0.2876
25	12.7	12.5928	0.1072	-0.247	0.041	0.2877
27	12.68	12.7009	0.0209	-0.251	0.053	0.3042
29	10.12	10.2469	0.1269	-0.302	0.0378	0.3398
31	5.985	6.1173	0.1323	-0.427	-0.0196	0.407

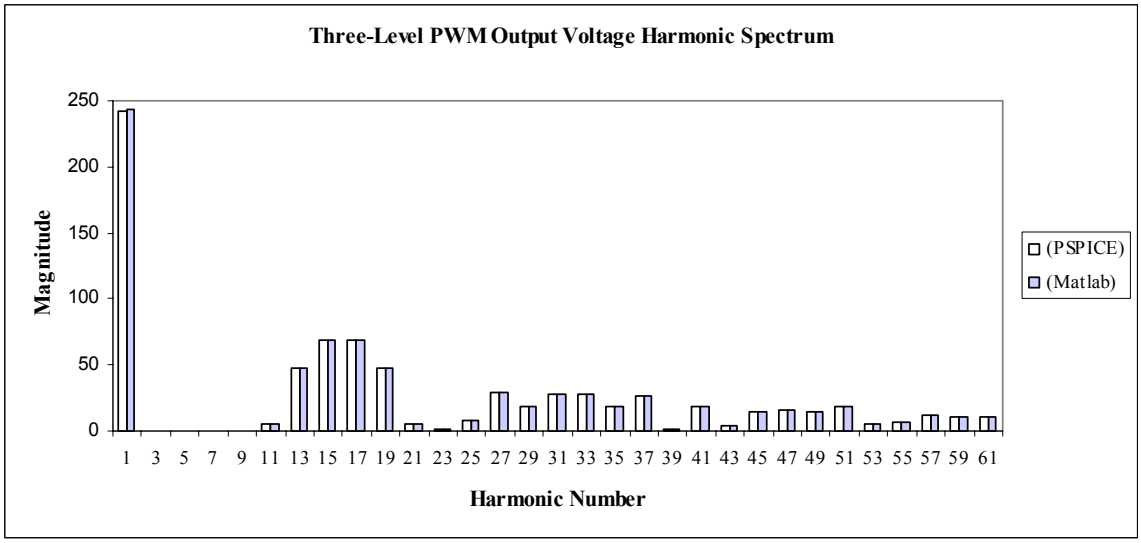

Figure 2.15. Harmonic Spectrum with m_a=0.9 and m_f=16.

2.1.2.3 Comparison of New and Old Methods

A paper written in 1981 by Mazzucchelli, et al. [23] claims to have a Fourier series representation for the output voltage waveform of a three-level PWM inverter based on an extension of Bennett's method [19] that is valid for amplitude modulation ratios greater than one. The equations used to calculate the harmonic components of the output voltage waveform of a three-level PWM inverter from [23] were coded in MATLAB. A MATLAB simulation was conducted using the three-level PWM inverter equations from [23] with V_i=270V, m_a=1.4, and m_f=18.

A three-level PWM simulation model was constructed in PSPICE for comparison purposes. A PSPICE ABM block was used to compare the sinusoidal control signal and the multi-level triangular carrier waveform. A Fourier analysis was then performed in PSPICE on the PWM output signal of the ABM block. The parameters used in the PSPICE simulation were the same as the ones used in the MATLAB simulation.

The results from the MATLAB coded equations of the Bessel function method presented in [23] were compared with the PSPICE simulation. The results from the comparison are shown in Table 2.9 for a few harmonics. Table 2.9 shows that the method presented in [23] is not very accurate when used to calculate the 3rd, 11th, and 39th harmonic components.

A MATLAB simulation using the method of pulse pairs was conducted using the same parameter values that were used in the previous two simulations. Table 2.10 shows the results from the method of pulse pairs compared with the PSPICE simulation. This table shows that the method of pulse pairs is a more accurate method than the one presented in [23]. It should be noted that the PSPICE values in Tables 2.9 and 2.10 were assumed to be the base (or benchmark) values and the percent error was calculated as:

$$\%\,error = \frac{|PSPICE\,value - MATLAB\,value|}{PSPICE\,value}\ x100\%\,. \tag{2.28}$$

Unless otherwise noted, all percent error calculations shown in the tables in this dissertation will be calculated as in (2.28).

TABLE 2.9
BESSEL FUNCTION METHOD AND PSPICE RESULTS FOR m_a=1.4 and m_f=18

	Voltage	Voltage		Voltage
Harmonic	(Bessel Function Method)	(PSPICE)	ΔV	% Error
Number	(V)	(V)	(V)	(% of PSPICE values)
1	311.7518	311.6	0.1518	0.05
3	34.3703	38.3	3.9297	11.43
11	11.4749	9.509	1.9659	17.13
13	34.8965	35.6	0.7035	2.02
17	20.0398	20.19	0.1502	0.75
21	43.3644	44.36	0.9956	2.30
39	7.7607	13.35	5.5893	72.02

TABLE 2.10
METHOD OF PULSE PAIRS AND PSPICE RESULTS FOR m_a=1.4 and m_f=18

	Voltage	Voltage		Voltage
Harmonic	(Method of Pulse Pairs)	(PSPICE)	ΔV	% Error
Number	(V)	(V)	(V)	(% of PSPICE values)
1	311.7425	311.6	0.1425	0.05
3	38.5205	38.3	0.2205	0.57
11	9.6195	9.509	0.1105	1.15
13	35.6043	35.6	0.0043	0.01
17	20.1429	20.19	0.0471	0.23
21	44.2791	44.36	0.0809	0.18
39	13.5071	13.35	0.1571	1.16

2.2 The Space Vector PWM Inverter

The analytical methods for determining the harmonic components of the output waveforms of a space vector PWM inverter presented in [16, 29, 36, 37] resulted in the appearance of Bessel functions in the final expression of the output PWM signal. Methods such as those presented in [16, 36] use the double Fourier series in the analysis. The purpose of this section is to present a method used to calculate the harmonic components of the output voltage waveforms of a space vector PWM inverter that is general and capable of being applied to various types of multilevel inverters and PWM schemes. This method allows direct calculation of harmonic magnitudes and angles without using the double Fourier series in the analysis. The final expression of the output voltage is compact, and does not contain Bessel functions. The method presented in this section also has the potential to be extended to inverter-drive systems such as the one presented in [44].

2.2.1 Carrier-Based Approach

Space vector modulation involves the vector decomposition of a desired voltage space vector into voltage vector components that can be generated using a typical six-switch, three-phase, voltage source inverter. The instantaneous output voltages are determined by the state of the inverter switches. Eight states are possible that correspond to the six possible instantaneous voltage vectors [29]. However, implementing this "classical" space vector PWM approach can be a complex task to perform. The implementation requires the use of Park's transformation, sector calculations, hexagon of states, and vector decomposition. A newer "carrier-based" approach can be used to implement the space vector PWM as shown by different researchers in the literature [45, 46]. The carrier-based method is less complex, more intuitive, and easier to implement than the classical method and will be used to generate the space vector PWM output voltages.

Space vector pulse width modulation can be realized by comparing a control signal with a triangular carrier signal as shown in Figure 2.16. The control signal shown in Figure 2.16 is the same control signal used in Mohan's carrier-based approach [38, 39]. The control signal shown in Figure 2.16 can be expressed as [29]:

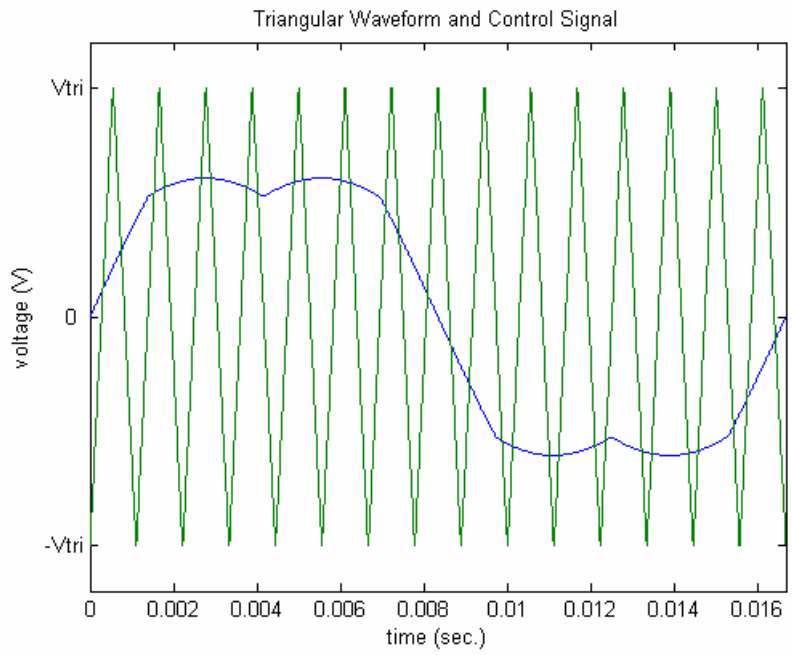

Figure 2.16: Triangular Waveform and Space Vector Control Signal.

$$v_{control}(t) = \begin{cases} \frac{3}{2} M \sin \omega t, & 0 \le \omega t \le \frac{\pi}{6} \\ \frac{\sqrt{3}}{2} M \sin\left(\omega t + \frac{\pi}{6}\right), & \frac{\pi}{6} \le \omega t \le \frac{\pi}{2} \\ \frac{\sqrt{3}}{2} M \sin\left(\omega t - \frac{\pi}{6}\right), & \frac{\pi}{2} \le \omega t \le \frac{5\pi}{6} \\ \frac{\sqrt{3}}{2} M \sin \omega t, & \frac{5\pi}{6} \le \omega t \le \pi \\ \frac{3}{2} M \sin \omega t, & \pi \le \omega t \le \frac{7\pi}{6} \\ \frac{\sqrt{3}}{2} M \sin\left(\omega t + \frac{\pi}{6}\right), & \frac{7\pi}{6} \le \omega t \le \frac{3\pi}{2} \\ \frac{\sqrt{3}}{2} M \sin\left(\omega t - \frac{\pi}{6}\right), & \frac{3\pi}{2} \le \omega t \le \frac{11\pi}{6} \\ \frac{3}{2} M \sin \omega t, & \frac{11\pi}{6} \le \omega t \le 2\pi \end{cases} \tag{2.29}$$

where M is the modulation index, and ω is the angular frequency. The range of values of (2.29) is limited to $M \leq 1.15$. Once the level of $M = 1.15$ is reached, different regions of overmodulation are defined as described in [16]. Each region of overmodulation requires a different space vector modulation strategy. Extension of space vector modulation into the overmodulation region above $M = 1.15$ requires extensive computations and the use of look-up tables as noted in [16]. The output PWM signal can be produced by comparing the waveforms shown in Figure 2.16. Referring to Figure 2.2, when $v_{control} > v_{triangle}$, T_{A+} and T_{B-} are closed and the value of the output PMW signal is $+V_i$ (where V_i is the DC input voltage of the inverter). When $v_{control} < v_{triangle}$, T_{A-} and T_{B+} are closed and the value of the output PWM signal becomes $-V_i$. The output PWM signal produced from comparing the waveforms in Figure 2.16 is shown in Figure 2.17.

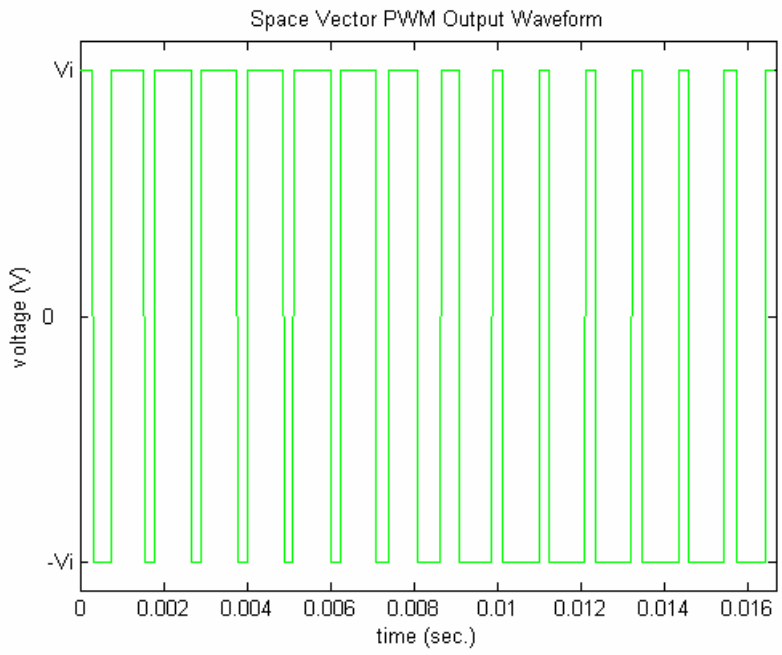

Figure 2.17: Space Vector PWM Output Waveform.

2.2.2 Method of Multiple Pulses

The method of multiple pulses was developed due to the fact that there is a possibility of a loss of half-wave symmetry in the output waveform of the space vector PWM inverter as described in [16, 35]. A function has half-wave symmetry if it satisfies $f(t)= - f(t-T/2)$. The method of pulse pairs would fail if half-wave symmetry is lost, because there would not be corresponding positive and negative pulse pairs in the output waveform. There is no limitation due to a loss of symmetry when the method of multiple pulses is used. This method is a general method that is valid regardless of the scheme utilized to produce a PWM waveform. The method of multiple pulses is less complex and easier to implement than other methods found in the literature. To begin the analysis, it can be observed that the waveform in Figure 2.17 is made up of multiple positive and negative pulses. Harmonic analysis of the PWM waveform shown in Figure 2.17 can be conducted by breaking up the waveform into multiple positive and negative pulses analyzed individually. An arbitrary positive pulse is shown in Figure 2.18 where A in the figure is the amplitude of the pulse, a_P is the initial time delay of the positive pulse, b_P is the pulse width of the positive pulse, and T is the period of the PWM waveform. An arbitrary negative pulse is shown in Figure 2.19 where a_N is the initial time delay of the negative pulse and b_N is the pulse width of the negative pulse.

The first step in the analysis is to find the trigonometric Fourier series of the waveform shown in Figure 2.18. The trigonometric Fourier series of the function $x(t)$ can be expressed as:

$$x(t) = a_{0_{POS}} + \sum_{n=1}^{\infty}\left(a_{n_{POS}} \cos\frac{2\pi n}{T} t + b_{n_{POS}} \sin\frac{2\pi n}{T} t \right) \tag{2.30}$$

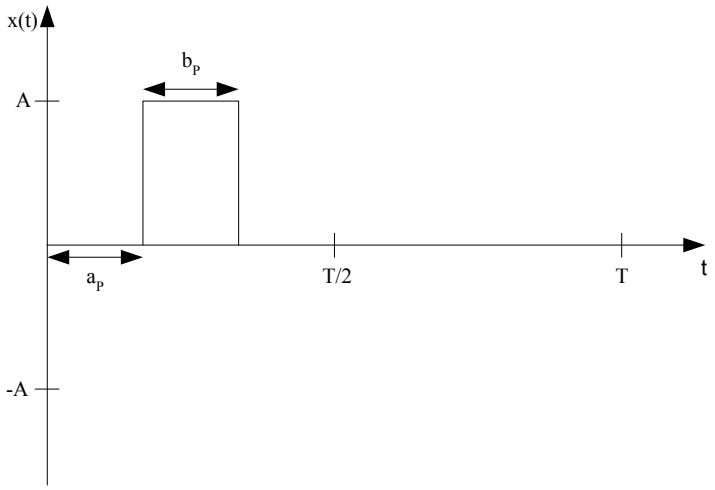

Figure 2.18: Positive Pulse.

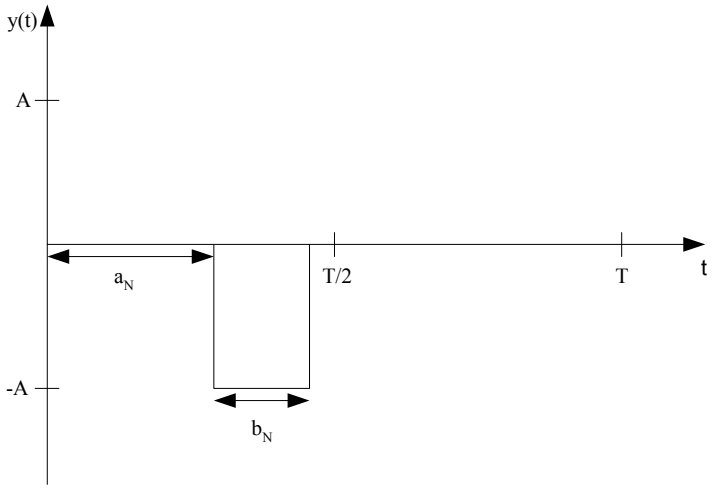

Figure 2.19: Negative Pulse.

where $a_{0_{POS}}$, $a_{n_{POS}}$, and $b_{n_{POS}}$ are the Fourier coefficients of the positive pulse. The coefficient $a_{0_{POS}}$ can be found from Figure 2.18 as follows:

$$a_{0_{POS}} = \frac{1}{T}\int_0^T x(t)\,dt\,, \tag{2.31}$$

$$a_{0_{POS}} = \frac{1}{T}\int_{a_P}^{a_P+b_P}(A)\,dt\,, \tag{2.32}$$

$$a_{0_{POS}} = \frac{1}{T}\left[Ab_P\right]. \tag{2.33}$$

The coefficient $a_{n_{POS}}$ can be found from Figure 2.18 as follows:

$$a_{n_{POS}} = \frac{2}{T}\int_0^T x(t)\cos\frac{2\pi n}{T}t\;dt\,, \tag{2.34}$$

$$a_{n_{POS}} = \frac{2}{T}\int_{a_P}^{a_P+b_P}(A)\cos\frac{2\pi n}{T}t\;dt\,. \tag{2.35}$$

Integrating (2.35) and using the identity $\sin\alpha - \sin\beta = 2\cos\frac{1}{2}(\alpha+\beta)\sin\frac{1}{2}(\alpha-\beta)$,

(2.35) becomes:

$$a_{n_{POS}} = \frac{2A}{\pi n}\left[\cos\left(\frac{2\pi n}{T}a_P + \frac{\pi n}{T}b_P\right)\sin\left(\frac{\pi n}{T}b_P\right)\right]. \tag{2.36}$$

The coefficient $b_{n_{POS}}$ can be found from Figure 2.18 as follows:

$$b_{n_{POS}} = \frac{2}{T}\int_0^T x(t)\sin\frac{2\pi n}{T}t\;dt, \tag{2.37}$$

$$b_{n_{POS}} = \frac{2}{T}\int_{a_P}^{a_P+b_P} A\sin\frac{2\pi n}{T}t\;dt\,. \tag{2.38}$$

Integrating (2.38), using the identity $\cos\alpha - \cos\beta = -2\sin\frac{1}{2}(\alpha+\beta)\sin\frac{1}{2}(\alpha-\beta)$, and

the fact that sin(-θ)= -sin(θ), (2.38) becomes:

$$b_{n_{POS}} = \frac{2A}{\pi n}\left[\sin\left(\frac{2\pi n}{T}a_P + \frac{\pi n}{T}b_P\right)\sin\left(\frac{\pi n}{T}b_P\right)\right]. \tag{2.39}$$

Equations (2.33), (2.36), and (2.39) can now be substituted into (2.30) and the trigonometric Fourier series of the waveform *x(t)* can be established. The trigonometric Fourier series of the waveform *y(t)* shown in Figure 2.19 is the same as the waveform *x(t)* in Figure 2.18 except that the magnitudes are the negative of each other. The Fourier coefficients for *y(t)* are as follows:

$$a_{0_{NEG}} = -\frac{1}{T}\left[Ab_P\right], \tag{2.40}$$

$$a_{n_{NEG}} = -\frac{2A}{\pi n}\left[\cos\left(\frac{2\pi n}{T}a_N + \frac{\pi n}{T}b_N\right)\sin\left(\frac{\pi n}{T}b_N\right)\right], \tag{2.41}$$

$$b_{n_{NEG}} = -\frac{2A}{\pi n}\left[\sin\left(\frac{2\pi n}{T}a_N + \frac{\pi n}{T}b_N\right)\sin\left(\frac{\pi n}{T}b_N\right)\right], \tag{2.42}$$

where $a_{0_{NEG}}$, $a_{n_{NEG}}$, and $b_{n_{NEG}}$ are the Fourier coefficients of the negative pulse. The trigonometric Fourier series for *y(t)* can be expressed in the same form as *x(t)* in (2.30):

$$y(t) = a_{0_{NEG}} + \sum_{n=1}^{\infty}\left(a_{n_{NEG}}\cos\frac{2\pi n}{T}t + b_{n_{NEG}}\sin\frac{2\pi n}{T}t\right). \tag{2.43}$$

Because the Fourier series of arbitrary positive and negative pulses has been established, the Fourier series of a given PWM signal produced by space vector modulation can be found by application of the principle of superposition. A PWM waveform like the one in Figure 2.17 is made up of the sum of positive and negative pulses as shown in Figure 2.20 where P1-P6 are positive pulses and N1-N5 are negative pulses. All that is required to find the Fourier series of a signal like the one shown in Figure 2.20 is to find the Fourier coefficients of each individual positive pulse and negative pulse contained in the PWM signal and add them to get the Fourier coefficients

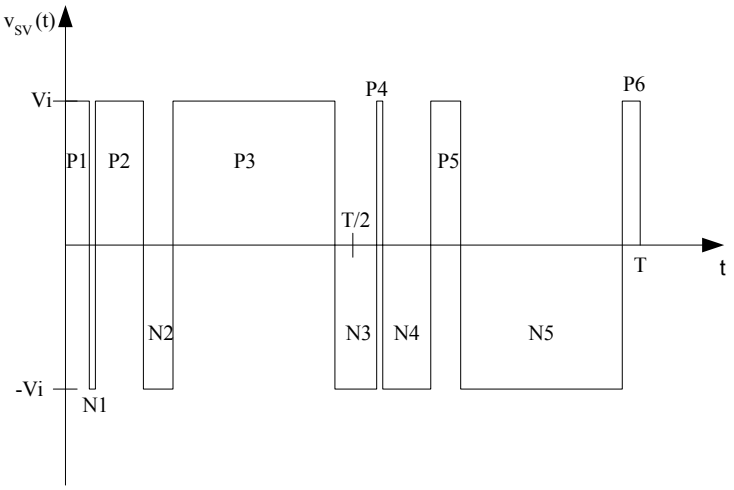

Figure 2.20: PWM Output Signal with Positive and Negative Pulses Labeled.

of the entire PWM signal. The total Fourier coefficients of the entire PWM signal can be found using (2.33), (2.36), and (2.39-2.42) as follows:

$$a_0 = \sum_{j=1}^{K_N} \left(a_{0_{NEG_j}} + a_{0_{POS_j}} \right), \tag{2.44}$$

$$a_n = \sum_{n=1}^{\infty} \sum_{j=1}^{K_N} \left(a_{n_{NEG_j}} \right) + \sum_{n=1}^{\infty} \sum_{j=1}^{K_P} \left(a_{n_{POS_j}} \right), \tag{2.45}$$

$$b_n = \sum_{n=1}^{\infty} \sum_{j=1}^{K_N} \left(b_{n_{NEG_j}} \right) + \sum_{n=1}^{\infty} \sum_{j=1}^{K_P} \left(b_{n_{POS_j}} \right), \tag{2.46}$$

where K_N is the number of negative pulses, and K_P is the number of positive pulses. The Fourier series of a given PWM signal produced by space vector modulation can be expressed in a single-cosine series as:

$$v_{SV}(t) = C_0 + \sum_{\substack{n=1 \\ n \text{ odd}}}^{\infty} C_n \cos\left(\frac{2\pi n}{T} t + \delta_n \right) \tag{2.47}$$

where $C_0 = a_0$, $C_n = \sqrt{a_n^2 + b_n^2}$, and $\delta_n = \tan^{-1}\left(-\frac{b_n}{a_n}\right)$. The subscript SV in (2.47) stands for space vector.

The final step in implementing this method is to find the crossing points of the waveforms shown in Figure 2.16 that determine the edges of the PWM signal pulses. In order to determine the crossing points, an equation for the triangular wave in Figure 2.16 is needed. An expression used to represent this waveform is given in (2.18).

2.2.3 Simulation Results for the Space Vector PWM Inverter

The equations of the control signal (2.29), the carrier waveform (2.18), and the equations used to implement the method of multiple pulses (2.33), (2.36), (2.39), (2.40-2.42), and (2.44-2.47) were coded in MATLAB for the purpose of computing the harmonic components of a PWM signal such as the one shown in Figure 2.17. MATLAB code was also written to find the crossing points, time delays, and pulse widths. Four MATLAB simulations were conducted using different values of M and m_f. The following parameter values were used for all simulations: V_i = 270 V, V_{tri} = 10 V, and f_1 = 60 Hz. The other parameters used for the first simulation were as follows: M=0.5 and f_s = 540 Hz. The parameters used for the second MATLAB simulation were: M=0.866 and f_s = 540 Hz. The parameters used for the third simulation were: M=0.7 and f_s = 900 Hz. The fourth simulation was conducted using the following parameters: M=0.65 and f_s = 900 Hz.

PSPICE was used to verify the results from the MATLAB calculations by constructing a space vector PWM simulation model. A PSPICE ABM block was used to

compare the control signal and the triangular carrier wave. A Fourier analysis was then performed in PSPICE on the PWM output signal of the ABM block. The parameters used in the PSPICE simulations were the same as the ones used in the four MATLAB simulations.

Results of the MATLAB and PSPICE simulations are shown in Tables 2.11-2.14. The results shown in Tables 2.11-2.14 include all harmonics up to the 31st harmonic. The harmonic spectrum of a space vector PWM inverter output voltage waveform with M=1.1 and m_f=27 is shown in Figure 2.20 for the first 61 harmonics. The light colored bars on the graph in Figure 2.21 are PSPICE results and the darker colored bars on the graph are results from the derived equations that were coded in MATLAB.

TABLE 2.11
MATLAB AND PSPICE RESULTS FOR M=0.5 and m_f=9

	Voltage	**Voltage**		**Voltage**	**Voltage**	
	Magnitude	**Magnitude**		**Angle**	**Angle**	
Harmonic	**PSPICE**	**MATLAB**	**ΔV**	**PSPICE**	**MATLAB**	**Δθ**
Number	(V)	(V)	(V)	(degrees)	(degrees)	(degrees)
1	135	135.023	0.023	0.06184	0.0636	0.00176
3	28.2	28.156	0.044	2.501	2.4728	0.0282
5	10.26	10.2734	0.0134	90.5	90.7438	0.2438
7	15.01	14.997	0.013	90.94	91.0142	0.0742
9	290.2	290.2518	0.0518	90.59	90.6879	0.0979
11	14.69	14.7426	0.0526	84.83	84.975	0.145
13	12.47	12.4597	0.0103	62.8	62.9017	0.1017
15	24.97	24.9186	0.0514	4.298	4.4682	0.1702
17	101.3	101.2876	0.0124	1.046	1.2386	0.1926
19	101.5	101.4705	0.0295	182.2	182.3483	0.1483
21	24.68	24.6842	0.0042	194.5	194.576	0.076
23	23.31	23.2777	0.0323	256.2	256.5535	0.3535
25	30.9	30.9417	0.0417	267.66	267.9628	0.3028
27	7.847	7.832	0.015	105.3	105.5191	0.2191
29	31.75	31.7658	0.0158	261.47	261.8123	0.3423
31	27.25	27.2818	0.0318	237	237.3195	0.3195

TABLE 2.12

MATLAB AND PSPICE RESULTS FOR M=0.866 and m_f=9

	Voltage	**Voltage**		**Voltage**	**Voltage**	
	Magnitude	**Magnitude**		**Angle**	**Angle**	
Harmonic	**PSPICE**	**MATLAB**	**ΔV**	**PSPICE**	**MATLAB**	**Δθ**
Number	(V)	(V)	(V)	(degrees)	(degrees)	(degrees)
1	233.9	233.8479	0.0521	0.209	0.2088	0.0002
3	47.01	47.0461	0.0361	4.994	4.9453	0.0487
5	27.8	27.8464	0.0464	90.67	90.811	0.141
7	41.82	41.7877	0.0323	90.64	90.7053	0.0653
9	194.1	194.1243	0.0243	90.18	90.2867	0.1067
11	42.54	42.5242	0.0158	81.34	81.446	0.106
13	36.57	36.6615	0.0915	52.58	52.6732	0.0932
15	32.97	32.9496	0.0204	7.404	7.6133	0.2093
17	86.3	86.3222	0.0222	-0.635	-0.4072	0.2278
19	86.32	86.3061	0.0139	187.5	187.7082	0.2082
21	37.8	37.7688	0.0312	213.3	213.6108	0.3108
23	36.79	36.719	0.071	228.9	229.1608	0.2608
25	36.01	35.999	0.011	251.1	251.4222	0.3222
27	74.91	74.9134	0.0034	101.3	101.5967	0.2967
29	37.6	37.6243	0.0243	244.2	244.5293	0.3293
31	30.27	30.3025	0.0325	232.2	232.5469	0.3469

TABLE 2.13

MATLAB AND PSPICE RESULTS FOR M=0.7 and m_f=15

	Voltage	**Voltage**		**Voltage**	**Voltage**	
	Magnitude	**Magnitude**		**Angle**	**Angle**	
Harmonic	**PSPICE**	**MATLAB**	**ΔV**	**PSPICE**	**MATLAB**	**Δθ**
Number	(V)	(V)	(V)	(degrees)	(degrees)	(degrees)
1	189	189.001	0.001	-0.02108	-0.0173	0.00378
3	38.87	38.8784	0.0084	-0.5511	-0.4735	0.0776
5	1.459	1.4856	0.0266	268.14	268.6838	0.5438
7	1.856	1.8592	0.0032	90.16	91.2928	1.1328
9	4.675	4.6945	0.0195	141.7	141.6784	0.0216
11	19.65	19.6529	0.0029	89.55	89.7153	0.1653
13	28.19	28.1499	0.0401	89.47	89.7296	0.2596
15	242.3	242.2973	0.0027	89.57	89.7477	0.1777
17	28.07	28.1285	0.0585	90.49	90.6927	0.2027
19	19.88	19.8898	0.0098	91.16	91.5545	0.3945
21	3.032	3.0604	0.0284	85.27	85.1494	0.1206
23	4.105	4.0833	0.0217	31.64	31.7633	0.1233
25	13.85	13.8198	0.0302	-9.223	-8.7861	0.4369
27	29.9	29.8562	0.0438	-1.691	-1.3571	0.3339
29	103.7	103.8003	0.1003	-0.7829	-0.4568	0.3261
31	103.8	103.768	0.032	178.8	179.1586	0.3586

TABLE 2.14

MATLAB AND PSPICE RESULTS FOR M=0.65 and m_f=15

	Voltage Magnitude	Voltage Magnitude		Voltage Angle	Voltage Angle	
Harmonic Number	**PSPICE** (V)	**MATLAB** (V)	**ΔV** (V)	**PSPICE** (degrees)	**MATLAB** (degrees)	**Δθ** (degrees)
1	175.5	175.501	0.001	-0.008324	-0.0141	0.005776
3	36.16	36.1635	0.0035	-0.5121	-0.4455	0.0666
5	1.29	1.321	0.031	268.19	268.697	0.507
7	1.576	1.6077	0.0317	91.21	91.3396	0.1296
9	4.255	4.2918	0.0368	144.9	144.7438	0.1562
11	17.18	17.1535	0.0265	89.68	89.7168	0.0368
13	24.52	24.536	0.016	89.49	89.7247	0.2347
15	255.4	255.4661	0.0661	89.55	89.7422	0.1922
17	24.54	24.4988	0.0412	90.56	90.6821	0.1221
19	17.36	17.3766	0.0166	91.36	91.5882	0.2282
21	2.663	2.6327	0.0303	96.75	96.0965	0.6535
23	3.399	3.3937	0.0053	34.62	34.5675	0.0525
25	11.56	11.5085	0.0515	-9.882	-9.618	0.264
27	28.77	28.8084	0.0384	-1.752	-1.3321	0.4199
29	105.7	105.7049	0.0049	-0.8627	-0.4768	0.3859
31	105.7	105.6959	0.0041	178.8	179.2077	0.4077

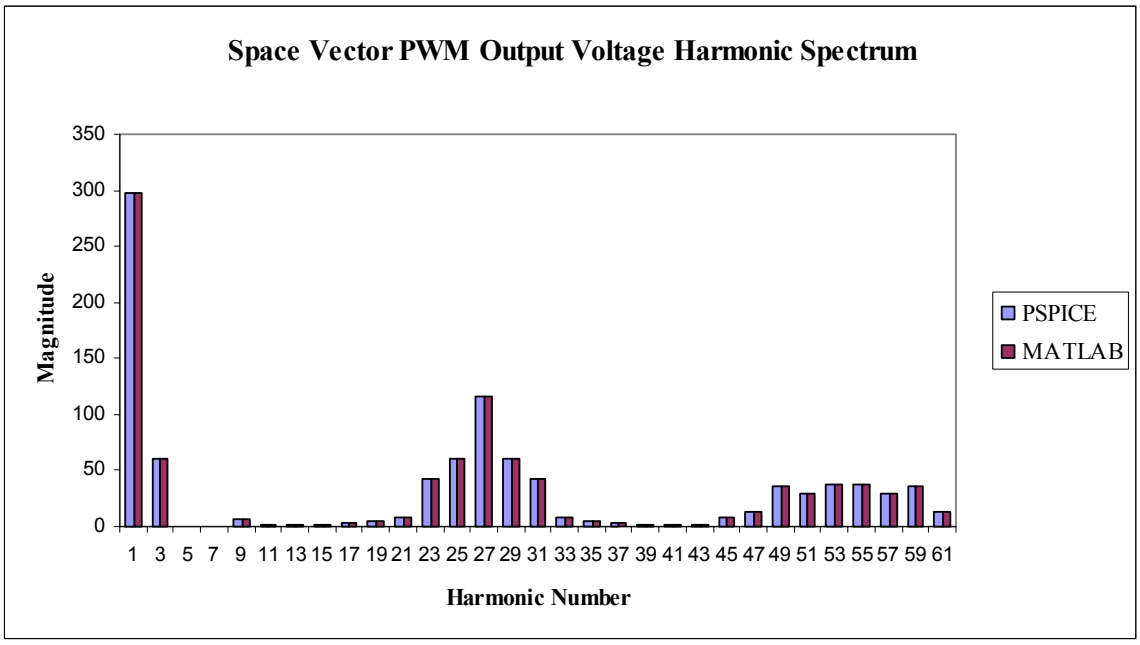

Figure 2.21: Harmonic Spectrum with M=1.1 and m_f=27.

The harmonic components found using the equations coded in MATLAB are similar to the ones found using the PSPICE model as illustrated by the results in the tables and Figure 2.21. The method of multiple pulses is an accurate method used to find the harmonic components of a space vector PWM inverter output waveform as illustrated by the results.

2.3 Line-to-Neutral Voltage Fourier Series Development

The focus of the previous sections of this chapter has been on determining the harmonic content of the output voltages of the sinusoidal PWM inverter and the space vector PWM inverter. The methods developed were shown to be effective methods for determining the harmonic content of the inverter output waveforms. However, the inverter output waveforms are typical waveforms produced from single-phase inverters. The focus of Chapter 3 and Chapter 4 will be on analyzing a three-phase, voltage source inverter supplying an induction motor. A general diagram of the system is shown in Figure 2.22. The purpose of this section is to develop a general Fourier series expression of the phase *a* line-neutral voltage produced from the three-phase inverter system shown in Figure 2.22 that can be used in the harmonic analysis of an induction motor supplied by a three-phase inverter.

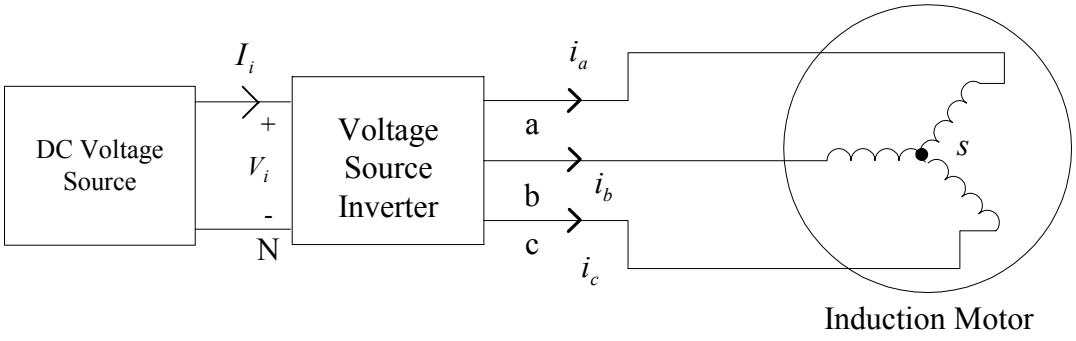

Figure 2.22: Three-Phase Inverter Block Model.

2.3.1 The Six-Step Inverter

In this section, the Fourier series of the six-step voltage source inverter line-to-neutral voltage for both 180° and 120° conduction will be presented. The Fourier series of the line-to-neutral voltage of the six-step voltage source inverter can be easily found in the literature [8, 47]. However, the Fourier series will be presented in this section due to the fact that the Fourier series of the six-step inverter will be used in analyses presented in Chapter 3 and 4. It should be noted that the method of pulse pairs or the method of multiple pulses can be used to produce the Fourier series of the line-to-neutral voltage of the six-step voltage source inverter.

2.3.1.1 120° Conduction

A plot of the phase *a* line-to-neutral voltage of the six-step inverter with 120° conduction is shown in Figure 2.23. The Fourier series of the six-step inverter phase *a* line-to-neutral voltage waveform with 120° conduction can be expressed as [8, 47]:

$$v_{\phi}(t) = \frac{\sqrt{3}}{\pi} V_i \left[\cos(\omega t + 30°) - \frac{1}{5}\cos(5\omega t + 30°) - \frac{1}{7}\cos(7\omega t + 30°) + \frac{1}{11}\cos(11\omega t + 30°) + \ldots \right] \tag{2.48}$$

As can be seen from (2.48), harmonics exist at $h = 6k \pm 1$ for $k = 1, 2, 3, \ldots$. The other phase voltages can be found by substituting $\omega t - \frac{2}{3}\pi$ and $\omega t + \frac{2}{3}\pi$ into (2.48) in place of ω.

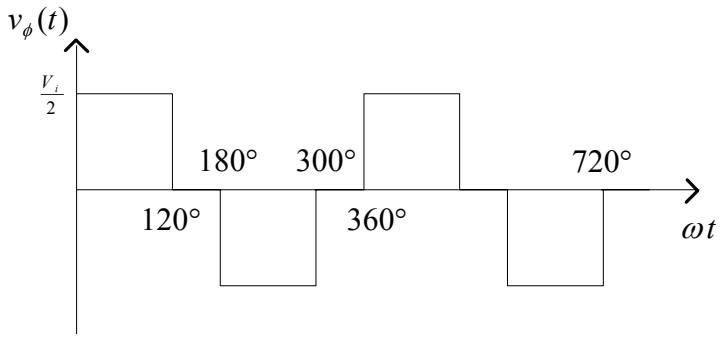

Figure 2.23: Six-Step Phase *a* Voltage Waveform with 120° Conduction.

2.3.1.2 180° Conduction

A plot of the phase *a* voltage of the six-step inverter with 180° conduction is shown in Figure 2.24. The Fourier series of the basic six-step inverter representing the phase *a* voltage during normal, balanced operation with 180° conduction can be expressed as [8, 47]:

$$v_\phi(t) = \frac{2}{\pi} V_i \left[\cos\omega t + \frac{1}{5}\cos 5\omega t - \frac{1}{7}\cos 7\omega t - \frac{1}{11}\cos 11\omega t + \ldots \right]. \tag{2.49}$$

It is easy to recognize from (2.49) that harmonics exist at $h = 6k \pm 1$ for $k = 1, 2, 3, \ldots$ The other phase voltages can be found by substituting $\omega t - \frac{2}{3}\pi$ and $\omega t + \frac{2}{3}\pi$ into (2.49) in place of ω.

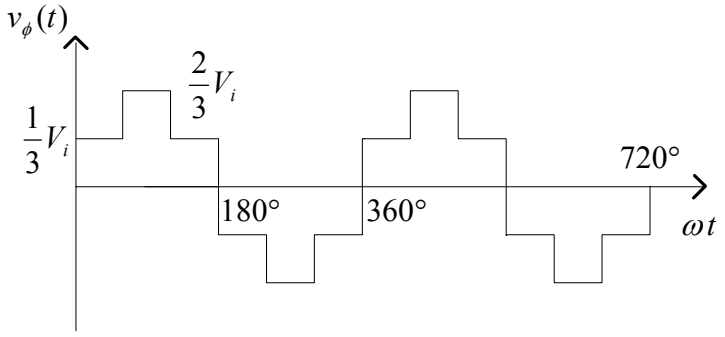

Figure 2.24: Six-Step Phase *a* Voltage Waveform with 180° Conduction.

2.3.2 Two-Level Sinusoidal PWM Inverter

When the motor in Figure 2.22 is supplied from a three-phase two-level sinusoidal PWM inverter, the line-to-negative DC bus voltage waveforms (the negative DC bus is denoted with an N in Figure 2.22) produced under balanced operating conditions for m_a=1.4 and m_f=15 can be produced by comparing the three sinusoidal control signals shifted 120° from each other with a triangular carrier waveform as illustrated in Figure 2.25. The resulting line-to-negative DC bus voltage waveforms are shown in Figure 2.26. A harmonic analysis can be conducted on these waveforms by using the method of multiple pulses that was discussed in Section 2.2.2. As can be observed from Figure 2.26, the waveforms shown can be broken up into multiple positive pulses as shown in Figure 2.27 and analyzed individually as in Section 2.2.2. The equation of the triangular carrier waveform used to find the crossing points is the same as in (2.18). It should be noted that the waveform in Figure 2.26 will contain a DC component. The Fourier series of the phase *a* line-to-negative DC bus voltage produced by two-level sinusoidal modulation can be expressed as:

$$v_{aN}(t) = C_0 + \sum_{n=1}^{\infty} C_n \cos\left(\frac{2\pi n}{T}t + \delta_n\right) \tag{2.50}$$

where $C_0 = a_0$, $C_n = \sqrt{{a_n}^2 + {b_n}^2}$, and $\delta_n = \tan^{-1}\left(-\frac{b_n}{a_n}\right)$.

The trigonometric Fourier series of the line-to-negative DC bus voltage has now been established in (2.50). However, a trigonometric Fourier series representation of the phase

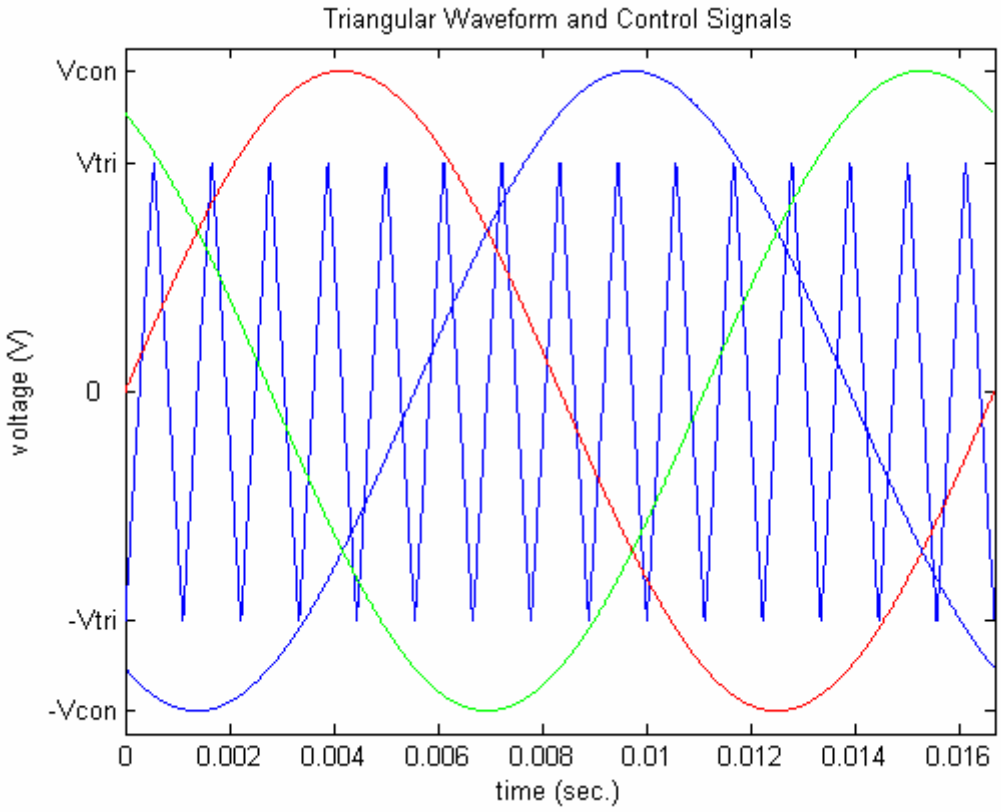

Figure 2.25: Three-Phase Sinusoidal PWM Control Signals and Carrier Waveform.

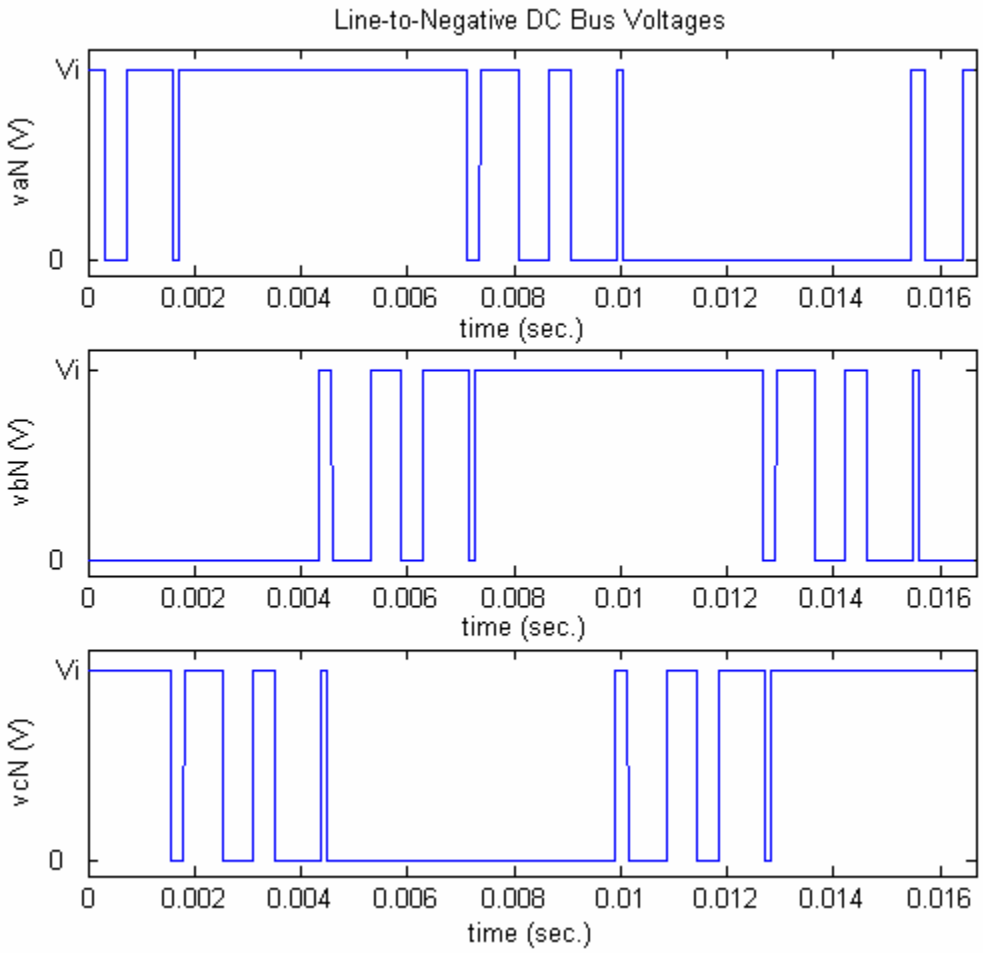

Figure 2.26: Line-to-Negative DC Bus Voltage Waveforms.

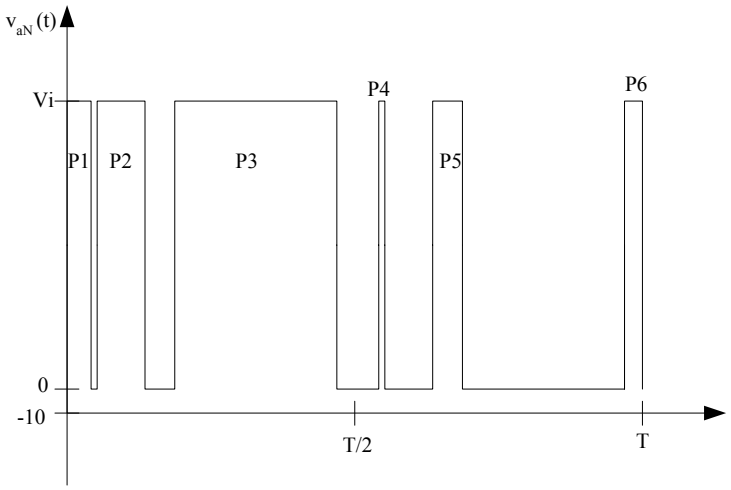

Figure 2.27: Waveform $v_{aN}(t)$ with Pulses Labeled.

a line-to-neutral voltage of the system shown in Figure 2.22 is needed. The phase a line-to-neutral voltage waveform for this system while supplied by a two-level sinusoidal PWM inverter is shown in Figure 2.28. Before beginning to develop a Fourier series representation of the line-to-neutral voltage, it is appropriate to first look at the harmonic spectrums of the phase *a* line-to-negative DC bus voltage and the phase *a* line-to-neutral voltage by creating the waveforms in MATLAB and using the FFT command to produce the harmonic spectrums. The harmonic spectrum of the phase *a* line-to-negative DC bus voltage is shown in Figure 2.29 and the harmonic spectrum of the phase *a* line-to-neutral voltage is shown in Figure 2.30. It can be observed from Figure 2.29 and Figure 2.30 that the magnitudes of the harmonics and the harmonic content of each voltage waveform is the same except that the line-to-neutral voltage does not contain a DC component nor any zero-sequence harmonics (triplen harmonics). For maximum cancellation of dominant harmonics in the line voltages of a three-phase inverter, m_f should always be odd and a multiple of three [27]. The results from the comparison of the harmonic

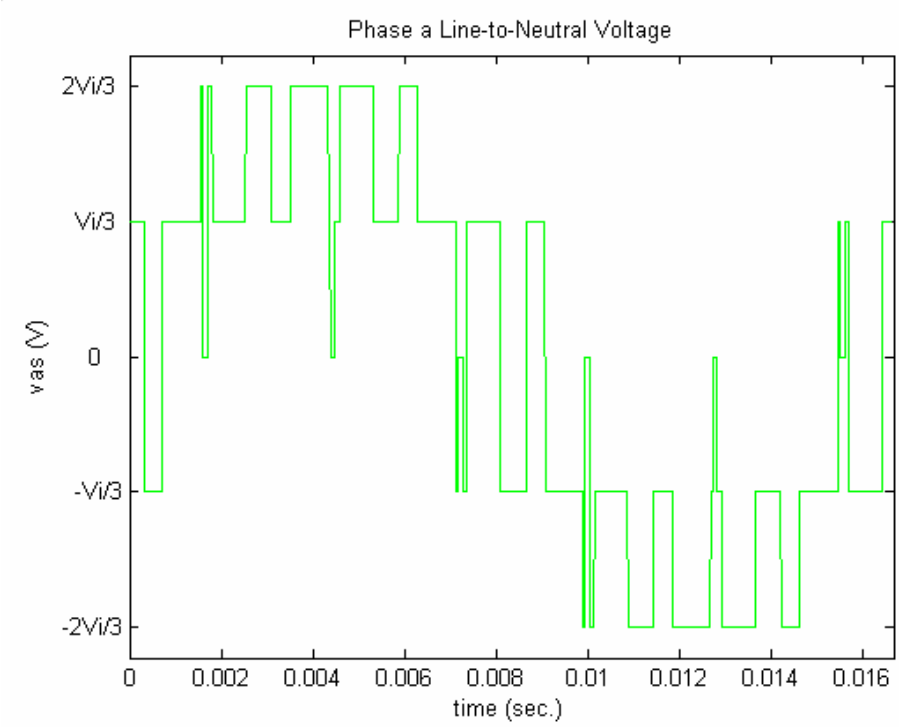

Figure 2.28: Phase *a* Line-to-Neutral Voltage Produced using MATLAB.

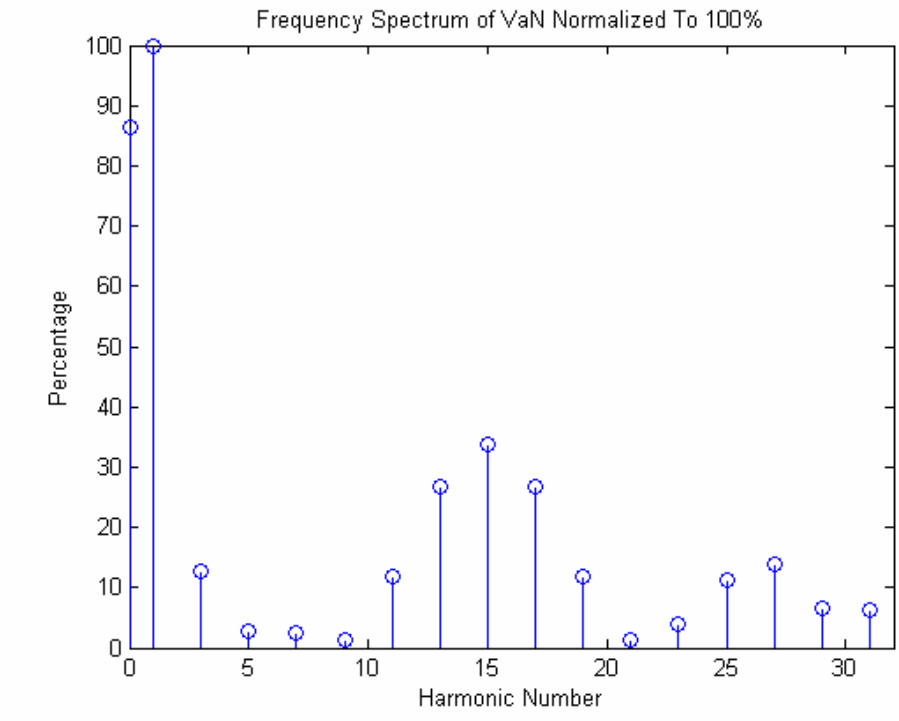

Figure 2.29: Harmonic Spectrum of the Phase *a* Line-to-Negative DC Bus Voltage.

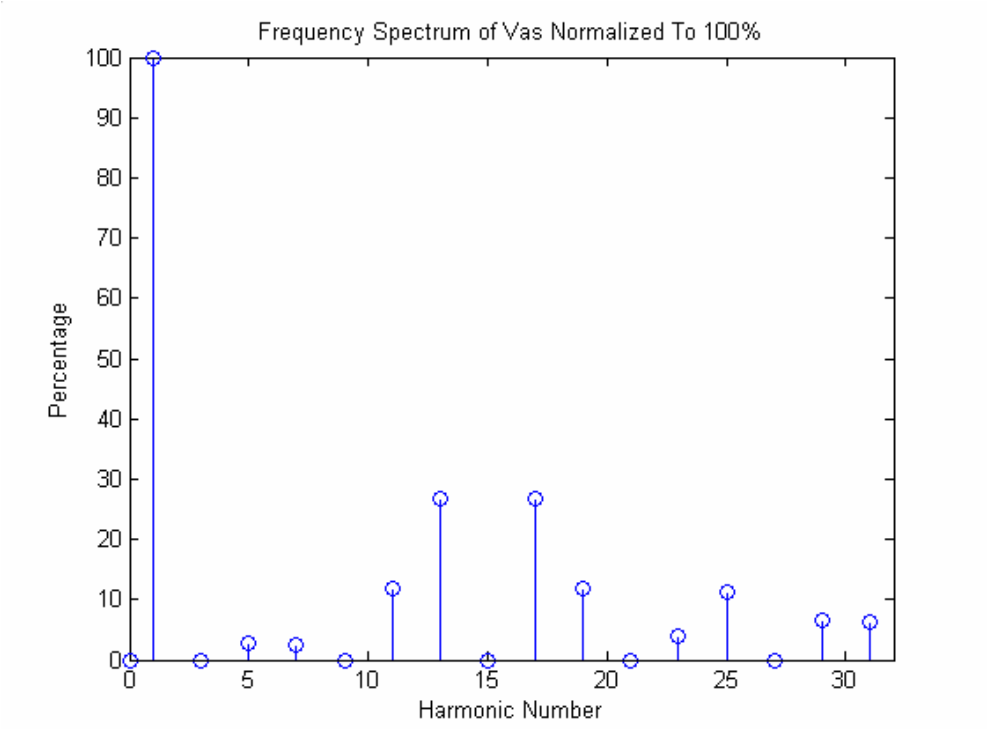

Figure 2.30: Harmonic Spectrum of the Phase *a* Line-to-Neutral Voltage.

spectrums can be proven mathematically by first considering some basic three-phase relationships for the system shown in Figure 2.22. The inverter line-to-neutral voltages can be expressed as [27]:

$$v_{as}(t) = v_{aN}(t) - v_{sN}(t), \tag{2.51}$$

$$v_{bs}(t) = v_{bN}(t) - v_{sN}(t), \tag{2.52}$$

$$v_{cs}(t) = v_{cN}(t) - v_{sN}(t). \tag{2.53}$$

The following condition for the inverter voltages must hold under balanced conditions [27]:

$$v_{as}(t) + v_{bs}(t) + v_{cs}(t) = 0. \tag{2.46}$$

The following relationship can be obtained by substituting (2.51-2.53) into (2.54):

$$v_{sN}(t) = \frac{1}{3}\left[v_{aN}(t) + v_{bN}(t) + v_{cN}(t) \right]. \tag{2.55}$$

By substituting (2.54) into (2.50), the phase *a* line-to-neutral voltage can be expressed as:

$$v_{as}(t) = \frac{2}{3} v_{aN}(t) - \frac{1}{3} v_{bN}(t) - \frac{1}{3} v_{cN}(t). \tag{2.56}$$

Using (2.56) it is easy to prove that no DC component exists in the phase *a* line-to-neutral voltage by considering the DC component of each line-to-negative DC bus voltage: $V_{aN_0} = A_0$, $V_{bN_0} = A_0$, and $V_{cN_0} = A_0$. These components can be substituted into (2.56) as follows:

$$V_{as_0} = \frac{2}{3} V_{aN_0} - \frac{1}{3} V_{bN_0} - \frac{1}{3} V_{cN_0}, \tag{2.57}$$

$$V_{as_0} = \frac{2}{3} A_0 - \frac{1}{3} A_0 - \frac{1}{3} A_0 = 0. \tag{2.58}$$

As can be seen from (2.58), no DC component exists in the line-to-neutral voltage. It can also be shown that the magnitudes of the harmonic components in the harmonic spectrum of the line-to-neutral voltages are the same as the magnitudes of the line-to-negative DC bus voltages. This can be accomplished by considering a balanced set of fundamental line-to-negative DC bus voltages:

$$v_{aN_1}(t) = A_1 \cos \omega t, \tag{2.59}$$

$$v_{bN_1}(t) = A_1 \cos\left(\omega t - 120°\right), \tag{2.60}$$

$$v_{cN_1}(t) = A_1 \cos\left(\omega t + 120°\right). \tag{2.61}$$

These voltages can be substituted into (2.56) as follows:

$$v_{as_1}(t) = \frac{2}{3} A_1 \cos \omega t - \frac{1}{3} A_1 \cos\left(\omega t - 120°\right) - \frac{1}{3} A_1 \cos\left(\omega t + 120°\right). \tag{2.62}$$

Using the trigonometric identity $\cos(\alpha \pm \beta) = \cos\alpha\cos\beta \mp \sin\alpha\sin\beta$, (2.62) can be written as:

$$v_{as_1}(t) = \frac{2}{3}A_1\cos\omega t + \frac{1}{6}A_1\cos\omega t + \frac{1}{6}A_1\cos\omega t, \tag{2.63}$$

$$v_{as_1}(t) = A_1\cos\omega t. \tag{2.64}$$

The result in (2.64) matches (2.59), verifying that the harmonic spectrums of the phase *a* line-to-neutral and the line-to-negative DC bus voltages are the same excluding the triplen harmonics and the DC component. Perhaps the most important result is to show that the triplen harmonics are not present in the line-to-neutral voltages. To prove this, consider the following balanced set of 3rd harmonic voltages:

$$v_{aN_3}(t) = A_3\cos 3\omega t, \tag{2.65}$$

$$v_{bN_3}(t) = A_3\cos\left(3\omega t - 360°\right), \tag{2.66}$$

$$v_{cN_3}(t) = A_3\cos\left(3\omega t + 360°\right). \tag{2.67}$$

The voltages in (2.65-2.67) can be substituted into (2.56) as follows:

$$v_{as_3}(t) = \frac{2}{3}A_3\cos 3\omega t - \frac{1}{3}A_3\cos(3\omega t - 360°) - \frac{1}{3}A_3\cos(3\omega t + 360°). \tag{2.68}$$

The trigonometric identity $\cos(\alpha \pm \beta) = \cos\alpha\cos\beta \mp \sin\alpha\sin\beta$ can be used to express (2.68) as:

$$v_{as_3}(t) = \frac{2}{3}A_3\cos 3\omega t - \frac{1}{3}A_3\cos 3\omega t - \frac{1}{3}A_3\cos 3\omega t, \tag{2.69}$$

$$v_{as_3}(t) = \frac{2}{3}A_3\cos 3\omega t - \frac{2}{3}A_3\cos 3\omega t, \tag{2.70}$$

$$v_{as_3}(t) = 0. \tag{2.71}$$

The result in (2.71) proves that no zero-sequence (or triplen) harmonics exist in the line-to-neutral voltages. No zero-sequence current can flow in an ungrounded wye circuit under balanced or unbalanced conditions. At this point, the expression in (2.50) can be modified to produce a Fourier series representation for the phase a line-to-neutral voltage waveform shown in Figure 2.28 as:

$$v_{as}(t) = \sum_{\substack{n=1 \\ n\neq 3k \\ k=1,2,3,\ldots}}^{\infty} C_n \cos\left(\frac{2\pi n}{T}t + \delta_n\right) \tag{2.72}$$

where $C_n = \sqrt{a_n{}^2 + b_n{}^2}$, and $\delta_n = \tan^{-1}\left(-\frac{b_n}{a_n}\right)$.

The equation used to calculate the Fourier series of the phase *a* line-to-negative DC bus voltage produced by two-level sinusoidal modulation (2.50) and the equation used to calculate the Fourier series of the phase *a* line-to-neutral voltage produced by two-level sinusoidal modulation (2.72) were both coded in MATLAB for the purpose of computing the harmonic content of each waveform for a given set of parameter values. The equations of the control signal, the carrier waveform, and the equations used to implement the method of multiple pulses were also coded in MATLAB. The following parameter values were used for the simulation: V_i = 270 V, V_{tri} = 10 V, V_{con} = 14 V, f_1 = 60 Hz, and f_s = 900 Hz.

PSPICE was used to verify the results from the MATLAB calculations by constructing a two-level sinusoidal PWM inverter simulation model using PSPICE ABM blocks. A Fourier analysis was then performed in PSPICE on the phase *a* line-to-negative DC bus voltage and the phase *a* line-to-neutral voltage. The parameters used in the PSPICE simulations were the same as the ones used in the MATLAB simulation.

Results of the MATLAB and PSPICE simulations are shown in Tables 2.15 and 2.16. The harmonic components found using the equations coded in MATLAB are similar to the ones found using the PSPICE model as illustrated by the results in Tables 2.15 and 2.16. Based on these results, (2.50) and (2.72) are correct and the method of multiple pulses is an accurate method used to find the harmonic components of the voltage waveforms produced by a two-level sinusoidal PWM inverter.

TABLE 2.15
LINE-TO-NEGATIVE DC BUS VOLTAGE COMPONENTS FOR m_a=1.4 and m_f=15

	V_{aN}	V_{aN}		V_{aN}	V_{aN}	
	Magnitude	**Magnitude**	**ΔV**	**Angle**	**Angle**	**Δθ**
Harmonic	PSPICE	MATLAB		PSPICE	MATLAB	
Number	(Volts)	(Volts)	(Volts)	(degrees)	(degrees)	(degrees)
DC	134.8817	134.9002	0.0185			
1	155.9	155.9006	0.0006	-0.239	-0.2342	0.0047
3	19.6	19.6244	0.0244	3.519	3.5087	0.0103
5	4.3825	4.36375	0.01875	176.100	176.1209	0.0209
7	3.7795	3.77035	0.00915	-132.400	-132.5015	0.1015
9	2.005	2.0074	0.0024	33.060	33.788	0.728
11	18.63	18.6404	0.0104	87.700	87.8266	0.1266
13	41.815	41.8013	0.0137	91.390	91.5182	0.1282
15	52.7	52.66405	0.03595	89.820	89.9667	0.1467
17	41.825	41.8104	0.0146	88.310	88.4674	0.1574
19	18.645	18.64535	0.00035	92.430	92.5775	0.1475
21	1.8655	1.85815	0.00735	143.900	143.55	0.35
23	6.245	6.255	0.01	-26.680	-26.3705	0.3095
25	17.55	17.5476	0.0024	0.798	1.0319	0.2341
27	21.77	21.75875	0.01125	2.872	3.131	0.259
29	10.035	10.02525	0.00975	-4.290	-3.9921	0.2979
31	10.01	10.00735	0.00265	-176.800	-176.5163	0.2837

TABLE 2.16
LINE-TO-NEUTRAL VOLTAGE COMPONENTS FOR m_a=1.4 and m_f=15

	V_{as}	V_{as}		V_{as}	V_{as}	
	Magnitude	**Magnitude**	**ΔV**	**Angle**	**Angle**	**Δθ**
Harmonic	PSPICE	MATLAB		PSPICE	MATLAB	
Number	(V)	(V)	(V)	(degrees)	(degrees)	(degrees)
DC						
1	155.9	155.9006	0.0006	-0.239	-0.2342	0.0047
3						
5	4.3825	4.36375	0.01875	176.100	176.1209	0.0209
7	3.7795	3.77035	0.00915	-132.400	-132.5015	0.1015
9						
11	18.63	18.6404	0.0104	87.700	87.8266	0.1266
13	41.815	41.8013	0.0137	91.390	91.5182	0.1282
15						
17	41.825	41.8104	0.0146	88.310	88.4674	0.1574
19	18.645	18.64535	0.00035	92.430	92.5775	0.1475
21						
23	6.245	6.255	0.01	-26.680	-26.3705	0.3095
25	17.55	17.5476	0.0024	0.798	1.0319	0.2341
27						
29	10.035	10.02525	0.00975	-4.290	-3.9921	0.2979
31	10.01	10.00735	0.00265	-176.800	-176.5163	0.2837

2.3.3 The Space Vector PWM Inverter

When the motor in Figure 2.22 is supplied from a three-phase space vector PWM inverter, the line-to-negative DC bus voltage waveforms produced under balanced operating conditions can be produced by comparing the three space vector control signals shifted 120° from each other with a triangular carrier waveform as illustrated in Figure 2.31. The resulting line-to-negative DC bus voltage waveforms are shown in Figure 2.32. The phase *a* line-to-neutral voltage waveform produced by the system in Figure 2.22 while supplied by a space vector PWM inverter is shown in Figure 2.33. It can be observed by comparing Figure 2.26 and Figure 2.28 with Figure 2.32 and Figure 2.33 that the waveforms are similar and the method of multiple pulses presented in Section 2.3.1

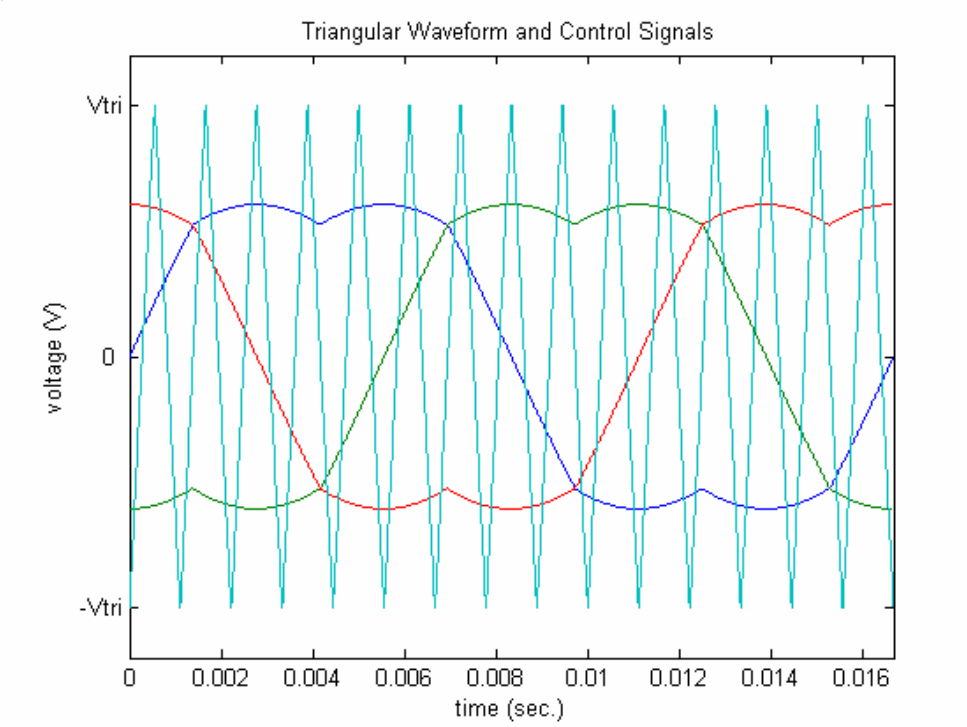

Figure 2.31: Space Vector PWM Control Signals and Carrier Waveform.

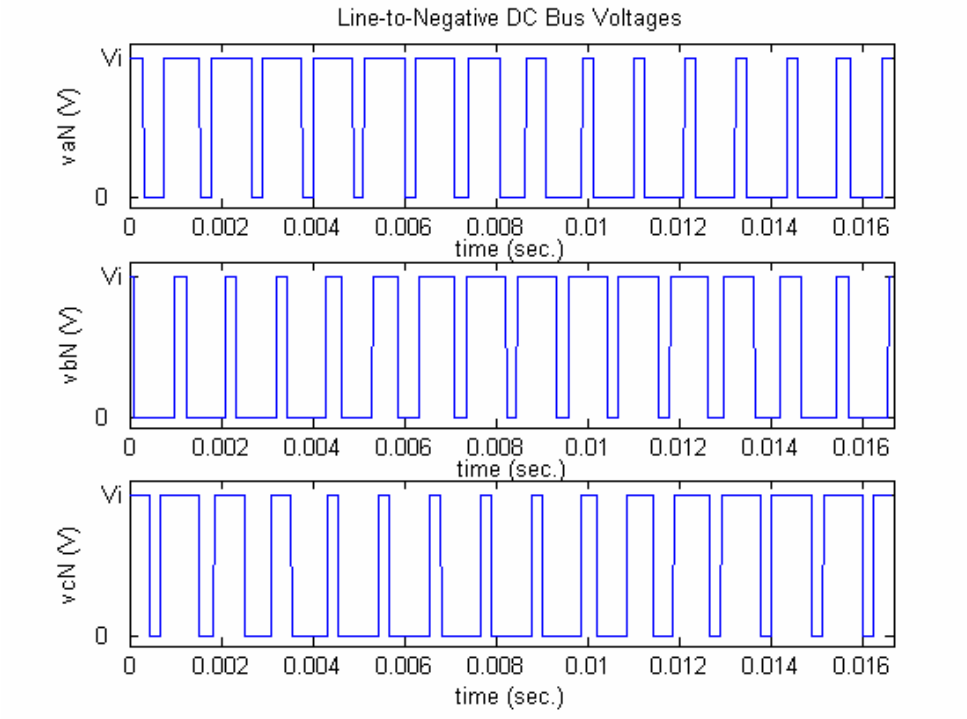

Figure 2.32: Line-to-Negative DC Bus Voltage Waveforms.

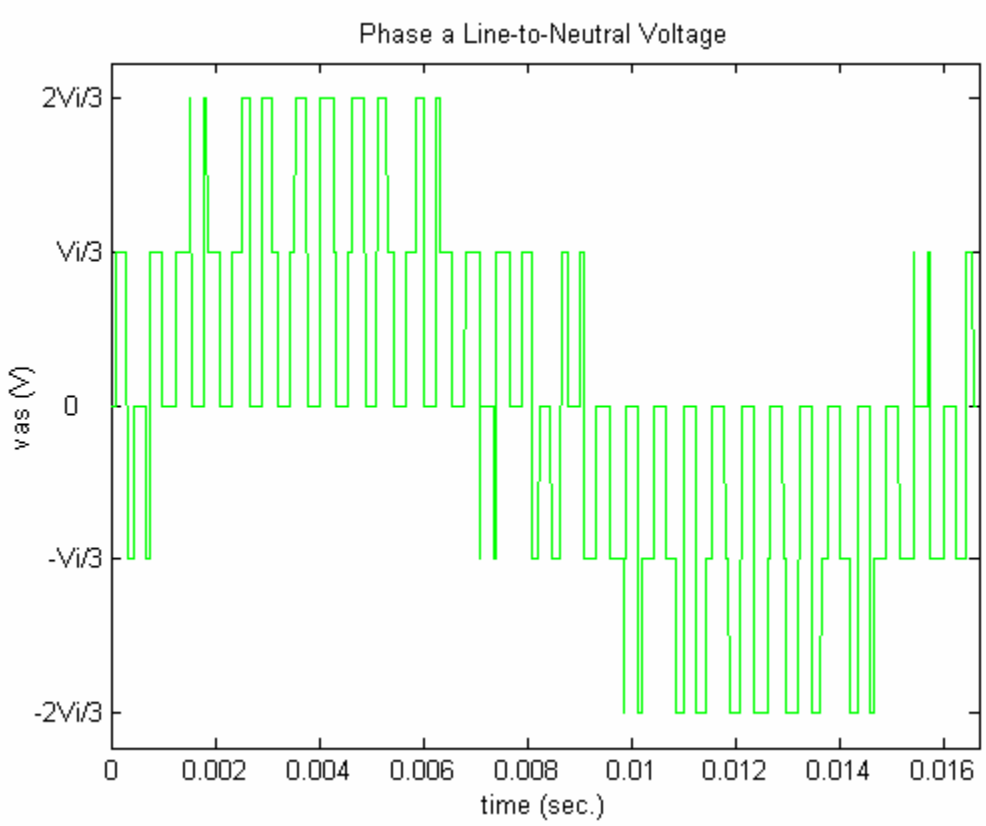

Figure 2.33: Phase *a* Line-to-Neutral Voltage Waveform.

can be used. The equation of the triangular waveform used to find the crossing points is the same as the one in (2.18) and the equation of the space vector control signal is given in (2.29). Using the method of multiple pulses from Section 2.3.1, the Fourier series of the phase *a* line-to-negative DC bus voltage produced by space vector modulation can be expressed as:

$$v_{aN}(t) = C_0 + \sum_{n=1}^{\infty} C_n \cos\left(\frac{2\pi n}{T}t + \delta_n\right) \tag{2.73}$$

where $C_0 = a_0$, $C_n = \sqrt{a_n{}^2 + b_n{}^2}$, and $\delta_n = \tan^{-1}\left(-\frac{b_n}{a_n}\right)$.

Because mf should be selected to be odd and a multiple of three, in order to cancel dominant harmonics [27], no triplen harmonics will appear in the line voltages. Therefore, the Fourier series of the phase a line-to-negative DC bus voltage of the space vector PWM inverter can be expressed as:

$$v_{as}(t) = \sum_{\substack{n=1 \\ n\neq 3k \\ k=1,2,3,\ldots}}^{\infty} C_n \cos\left(\frac{2\pi n}{T}t + \delta_n\right) \tag{2.74}$$

where $C_n = \sqrt{a_n{}^2 + b_n{}^2}$, and $\delta_n = \tan^{-1}\left(-\frac{b_n}{a_n}\right)$.

The Fourier series in (2.73) and (2.74) were both coded in MATLAB for the purpose of computing the harmonic content of the phase *a* line-to-negative DC bus voltage and the phase *a* line-to-neutral voltage produced by space vector modulation for a given set of parameter values. The equations of the space vector control signal, the carrier waveform, and the equations used to implement the method of multiple pulses were also coded in MATLAB. The following parameter values were used for the simulation: V_i = 270 V, M=0.7, f_1 = 60 Hz, and f_s = 900 Hz.

PSPICE was used to verify the results from the MATLAB calculations by constructing a space vector PWM inverter simulation model using PSPICE ABM blocks. A Fourier analysis was then performed in PSPICE on the phase *a* line-to-negative DC bus voltage and the phase *a* line-to-neutral voltage. The parameters used in the PSPICE simulations were the same as the ones used in the MATLAB simulation.

Results of the MATLAB and PSPICE simulations are shown in Tables 2.17 and 2.18. The harmonic components found using the equations coded in MATLAB are similar to the ones found using the PSPICE model as illustrated by the results in Tables 2.17 and

2.18. These results show that (2.73) and (2.74) are valid and that the method of multiple pulses is an accurate method used to find the harmonic components of the voltage waveforms produced by a space vector PWM inverter.

TABLE 2.17
LINE-TO-NEGATIVE DC BUS VOLTAGE COMPONENTS FOR M=0.7 and m_f=15

	V_{aN}	V_{aN}		V_{aN}	V_{aN}	
	Magnitude	**Magnitude**	**ΔV**	**Angle**	**Angle**	**Δθ**
Harmonic	PSPICE	Matlab		(PSPICE)	(Matlab)	
Number	(V)	(V)	(V)	(degrees)	(degrees)	(degrees)
DC	134.7298	134.7314	0.0016			
1	94.49	94.5005	0.0008	-0.021	-0.0173	0.00378
3	19.44	19.4392	0.0132	-0.551	-0.4735	0.0776
5	0.7296	0.7428	0.0018	-91.860	-91.3162	0.5438
7	0.9278	0.9296	0.00925	90.160	91.2928	1.1328
9	2.338	2.34725	0.00055	141.700	141.6784	0.0216
11	9.827	9.82645	0.02505	89.550	89.7153	0.1653
13	14.1	14.07495	0.05135	89.470	89.7296	0.2596
15	121.2	121.14865	0.02425	89.570	89.7477	0.1777
17	14.04	14.06425	0.0039	90.490	90.6927	0.2027
19	9.941	9.9449	0.0142	91.160	91.5545	0.3945
21	1.516	1.5302	0.01035	85.270	85.1494	0.1206
23	2.052	2.04165	0.0131	31.640	31.7633	0.1233
25	6.923	6.9099	0.0219	-9.223	-8.7861	0.4369
27	14.95	14.9281	0.03015	-1.691	-1.3571	0.3339
29	51.87	51.90015	0.026	-0.783	-0.4568	0.3261
31	51.91	51.884	0.026	178.800	179.1586	0.3586

TABLE 2.18
LINE-TO-NEUTRAL VOLTAGE COMPONENTS FOR M=0.7 and m_f=15

	V_{as}	V_{as}		V_{as}	V_{as}	
	Magnitude	**Magnitude**	**ΔV**	**Angle**	**Angle**	**Δθ**
Harmonic	PSPICE	Matlab		(PSPICE)	(Matlab)	
Number	(V)	(V)	(V)	(degrees)	(degrees)	(degrees)
DC						
1	94.49	94.5005	0.0105	-0.021	-0.0173	0.00378
3						
5	0.7296	0.7428	0.0132	-91.860	-91.3162	0.5438
7	0.9278	0.9296	0.0018	90.160	91.2928	1.1328
9						
11	9.827	9.82645	0.00055	89.550	89.7153	0.1653
13	14.1	14.07495	0.02505	89.470	89.7296	0.2596
15						
17	14.04	14.06425	0.02425	90.490	90.6927	0.2027
19	9.941	9.9449	0.0039	91.160	91.5545	0.3945
21						
23	2.052	2.04165	0.01035	31.640	31.7633	0.1233
25	6.923	6.9099	0.0131	-9.223	-8.7861	0.4369
27						
29	51.87	51.90015	0.03015	-0.783	-0.4568	0.3261
31	51.91	51.884	0.026	178.800	179.1586	0.3586

2.4 Summary

Two methods for finding the harmonic components of the output voltage of sinusoidal PWM inverters and space vector PWM inverters were presented in this chapter. The method of pulse pairs was the first method discussed. This method was shown to be applicable to different multilevel inverter types such as the two-level sinusoidal PWM inverter and the three-level sinusoidal PWM inverter. The method allowed direct calculation of harmonic magnitudes and angles without having to use linear approximations, iterative procedures, look-up tables, or Bessel functions. The main limitation of the method of pulse pairs is the possibility of a loss of symmetry in the

output voltage waveform of the inverter. To rectify this problem, the method of multiple pulses was developed. This method is entirely general and has the potential to be used to analyze the harmonic content of inverter output waveforms produced by various types of multilevel inverters and PWM schemes. There is no limitation of the method of multiple pulses due to loss of symmetry or the harmonic content of the inverter output voltage waveform. The line-to-neutral voltage Fourier series of the six-step, two-level sinusoidal PWM, and space vector PWM inverters were presented. The method of multiple pulses can be used to determine the harmonic content of the line-to-neutral voltages of all of the voltage source inverter types studied, including the space vector PWM inverter. This method will be utilized during MATLAB simulations conducted in Chapters 3 and 4.

CHAPTER 3

THE INVERTER-FED INDUCTION MOTOR

The focus of this chapter is on the inverter-fed induction motor. A steady-state harmonic model of the induction motor operating under balanced conditions is presented. The harmonic model is based on the T-type equivalent circuit of the induction motor, and is capable of being used to analyze induction motors supplied from nonsinusoidal sources. A simplified model of an inverter-fed induction motor that is based on the steady-state T-type equivalent circuit of the motor and the input-output relationships of the voltage source inverter is presented. A V-I load characteristic curve that allows the inverter, motor, and load to be replaced by a current-controlled voltage source is established. MATLAB and PSPICE simulation results are presented in order to validate the use of the simplified model.

3.1 Induction Motor Equivalent Circuit

All analysis and simulation in this dissertation are based on the steady-state T-type equivalent circuit model of the induction motor [40], shown in Figure 3.1a (note: all quantities have been reflected to the stator). This model is the positive-sequence equivalent circuit of the induction motor where balanced three-phase operation is assumed.

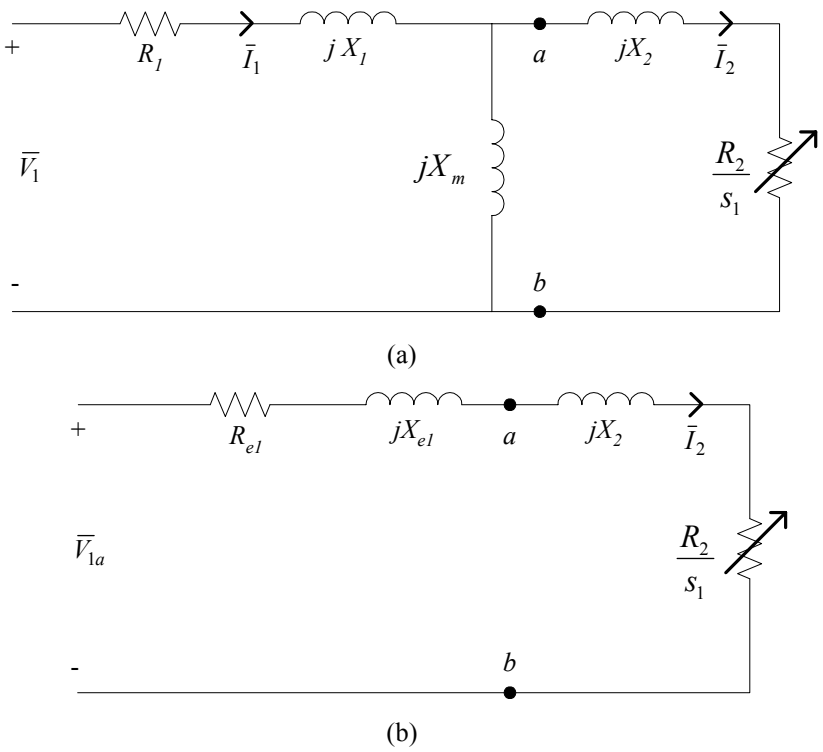

Figure 3.1: (a) Induction Motor T-Type Equivalent Circuit; (b) Thevenin Equivalent of (a).

Thevenin's theorem can be used to transform the network to the left of points *a* and *b* in Fig. 3.1a into an equivalent voltage source $\overline{V}_{1a}$ in series with an equivalent impedance $R_{e1}+jX_{e1}$ as shown in Figure 4.1b. The equivalent source voltage can be expressed as [40]:

$$\overline{V}_{1a} = \overline{V}_1 \frac{jX_m}{R_1 + j(X_1 + X_m)} \tag{3.1}$$

where $\overline{V}_1$ is the stator positive-sequence line-to-neutral voltage, X_m is the magnetizing reactance, R_1 is the stator resistance, and X_1 is the stator leakage reactance. The Thevenin-equivalent stator impedance is:

$$\overline{Z}_{e1} = R_{e1} + jX_{e1} = \frac{jX_m(R_1 + jX_1)}{R_1 + j(X_m + X_1)}. \tag{3.2}$$

From the Thevenin-equivalent circuit of Figure 3.1 (b), the magnitude of the rotor current referred to the stator is:

$$I_2 = \frac{V_{1a}}{\sqrt{\left(R_{e1} + \frac{R_2}{s_1}\right)^2 + (X_{e1} + X_2)^2}} \tag{3.3}$$

where R_2 is the rotor resistance, X_2 is the rotor leakage reactance, and s_1 is the fundamental slip.

The internal mechanical power developed by the motor can be expressed as [40]:

$$P_d = mI_2^2 R_2 \frac{1 - s_1}{s_1} \tag{3.4}$$

where m is the number of stator phases. The internal power (3.4) can also be written as:

$$P_d = T_e(1 - s_1)\omega_s \tag{3.5}$$

where T_e is the internal electromagnetic torque (N-m), and ω_s is the synchronous angular velocity (rad/s). The synchronous angular velocity is given as:

$$\omega_s = \frac{4\pi f}{P} \tag{3.6}$$

where f is the excitation frequency and P is the number of poles. Substituting (3.5) into (3.4) and solving for T_e yields an expression for the electromagnetic torque as follows:

$$T_e = \frac{m}{\omega_s} I_2^2 \frac{R_2}{s_1} \ . \tag{3.7}$$

Substituting (3.3) into (3.7) yields:

$$T_e = \frac{m}{\omega_s} \frac{V_{1a}^2 \frac{R_2}{s_1}}{\left(R_{e1} + \frac{R_2}{s_1}\right)^2 + (X_{e1} + X_2)^2} \tag{3.8}$$

Equation (3.8) can be rearranged and solved in terms of the slip as follows:

$$s_1 = \frac{-B \pm \sqrt{B^2 - 4AC}}{2A} \tag{3.9}$$

where $A = T_e \omega_s R_{e1}^2 + T_e \omega_s (X_{e1} + X_2)^2$, $B = 2T_e \omega_s R_2 R_{e1} - mR_2 V_{1a}^2$, and $C = T_e \omega_s R_2^2$.

The torque and rotor speed are related by [48]:

$$T_e = J \frac{2}{P} \frac{d\omega_r}{dt} + B_m \frac{2}{P} \omega_r + T_L \tag{3.10}$$

where J is the inertia of the rotor and the connected load, ω_r is the angular velocity of the rotor, B_m is the damping coefficient associated with the rotational system of the machine and mechanical load, and T_L is the load torque. The coefficient B_m is typically small and often neglected. Some simplifications of (3.10) can be made when considering the steady-state operation of the induction motor [48]. The speed is constant during steady-state operation and the acceleration is zero. Using these simplifications and the fact that B_m can be neglected, (3.10) becomes:

$$T_e = T_L \tag{3.11}$$

during steady-state operation. Substituting (3.11) into (3.9) produces an equation for the slip in terms of variables that are generally known.

The total impedance looking into the circuit of Figure 3.1 (a) is:

$$\overline{Z}_1 = R_1 + jX_1 + \frac{jX_m \left(\frac{R_2}{s_1} + jX_2 \right)}{\frac{R_2}{s_1} + j(X_m + X_2)} = Z_1 \angle \theta \tag{3.12}$$

The magnitude of the stator current can now be found using the following formula:

$$I_1 = \frac{V_1}{Z_1}. \tag{3.13}$$

The power factor can be found by taking the cosine of the angle from (3.12).

The equations developed in (3.1-3.13) are valid for the steady-state analysis of the induction motor under balanced operating conditions when the motor is supplied from a pure sinusoidal source. These equations can easily be modified to perform a harmonic analysis on an induction motor when supplied from a nonsinusoidal source. It is necessary to account for the kth harmonic number in (3.1-3.13) and define the slip for both positive and negative sequence harmonics. It should be noted that the frequency dependence of the motor resistances will be ignored in all analyses in this dissertation. Ignoring the frequency dependence of the resistances is a typical practice [8, 27, 40, and 43] that produces reasonable results for the practicing electrical engineer. For the interested researcher, a paper that investigates the frequency dependence of the rotor resistance of an inverter-fed induction motor can be found in [49].

The equivalent source voltage for the kth harmonic can be determined by examining Figure 3.2 and using Thevenin's theorem:

$$\overline{V}_{1a_k} = \overline{V}_k \frac{j\,kX_m}{R_1 + j(kX_1 + kX_m)} \tag{3.14}$$

where $\overline{V}_k$ is the kth harmonic stator line-to-neutral voltage. The kth harmonic Thevenin-equivalent stator impedance is:

$$\overline{Z}_{e1_k} = R_{e1_k} + jX_{e1_k} = \frac{jkX_m(R_1 + jkX_1)}{R_1 + j(kX_m + kX_1)} \tag{3.15}$$

The magnitude of the rotor current referred to the stator for the kth harmonic is:

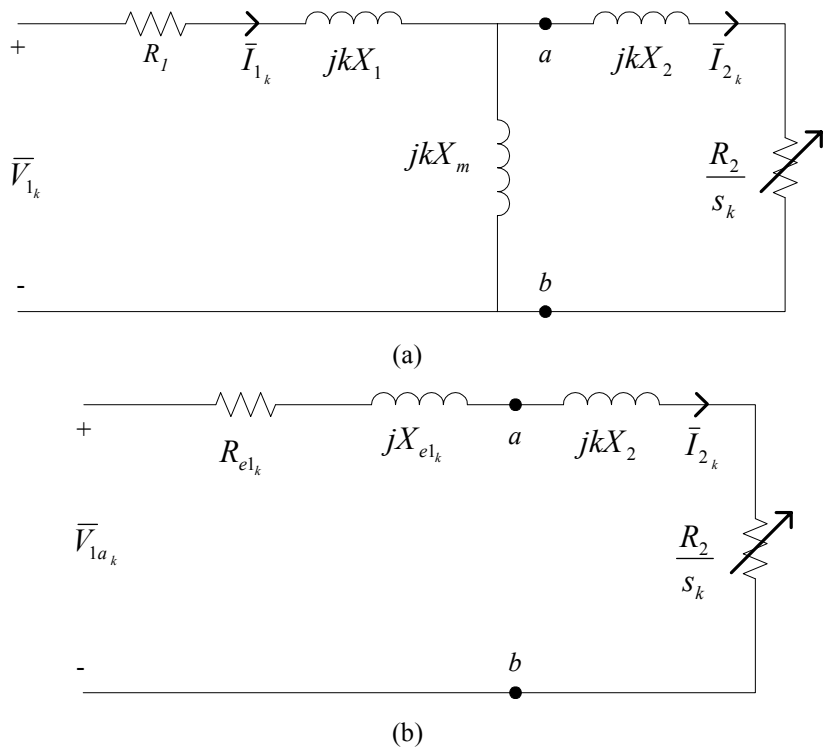

Figure 3.2: (a) Induction Motor Harmonic Equivalent Circuit; (b) Thevenin Equivalent of (a).

$$I_{2_k} = \frac{V_{1a_k}}{\sqrt{\left(R_{e1_k} + \frac{R_2}{s_k}\right)^2 + (kX_{e1_k} + kX_2)^2}} \tag{3.16}$$

where s_k is the k[th] harmonic slip. The internal mechanical power developed by the motor can be expressed as:

$$P_{d_k} = mI_{2_k}^2 R_2 \frac{1 - s_k}{s_k}. \tag{3.17}$$

The internal power (3.17) can also be written as:

$$P_{d_k} = T_{e_k}(1 - s_k)\omega_s. \tag{3.18}$$

Substituting (3.18) into (3.17) and solving for T_{ek} yields an expression for the k[th] harmonic electromagnetic torque as follows:

$$T_{e_k} = \pm \frac{m}{\omega_s} I_{2_k}^2 \frac{R_2}{s_k} \ . \tag{3.19}$$

The positive torque in (3.19) is produced by positive-sequence harmonics and the negative torque in (3.19) is produced by negative-sequence harmonics [8]. Substituting (3.16) into (3.19) yields:

$$T_{e_k} = \pm \frac{m}{\omega_s} \frac{V_{ka}^2 \frac{R_2}{s_k}}{\left(R_{e1} + \frac{R_2}{s_k} \right)^2 + (kX_{ek} + kX_2)^2} . \tag{3.20}$$

The total impedance looking into the circuit of Figure 3.2a is:

$$\overline{Z}_{1_k} = R_1 + jkX_1 + \frac{jkX_m \left(\frac{R_2}{s_k} + jkX_2 \right)}{\frac{R_2}{s_k} + j(kX_m + kX_2)} = Z_{1_k} \angle \theta_k \ . \tag{3.21}$$

The magnitude of the stator current for the k[th] harmonic can now be found using the following formula:

$$I_{1_k} = \frac{V_k}{Z_{1_k}} . \tag{3.22}$$

The positive-sequence harmonic equivalent circuit of the induction motor used for analysis and simulation purposes is shown in Figure 3.3, where k_p is the positive-sequence harmonic number and s_{k_P} is the slip for the k_p^{th} positive-sequence harmonic, which may be calculated using (3.23):

$$s_{k_p} = \frac{k_p - (1 - s_1)}{k_p}. \tag{3.23}$$

The negative-sequence harmonic equivalent circuit is shown in Figure 3.4, where k_n is the negative-sequence harmonic number and s_{k_n} is the slip for the k_n^{th} negative-sequence harmonic, which may be calculated using (3.24):

$$s_{k_n} = \frac{k_n + (1 - s_1)}{k_n}. \tag{3.24}$$

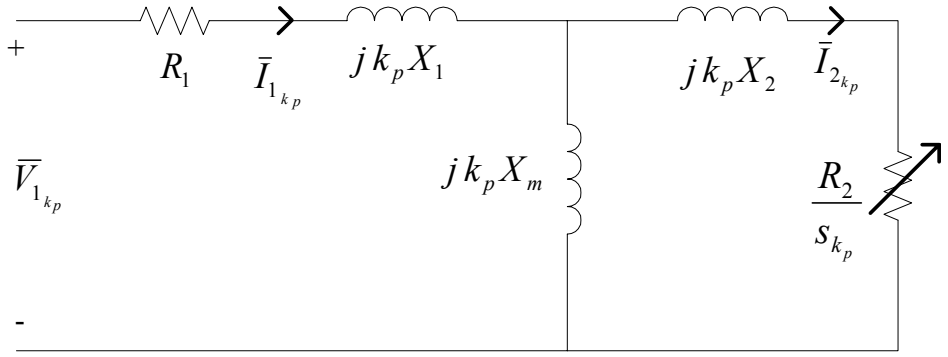

Figure 3.3. Positive-Sequence Harmonic Equivalent Circuit.

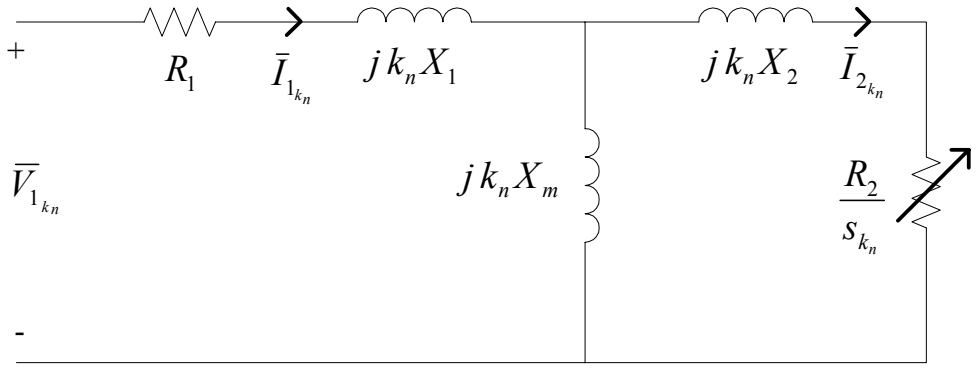

Figure 3.4. Negative-Sequence Harmonic Equivalent Circuit.

3.2 Verification of Induction Motor Harmonic Model

The equations of the induction motor based on the circuits shown in Figure 3.1 and Figure 3.2 were coded in MATLAB along with the six-step inverter output voltage Fourier series. A harmonic analysis was performed on a 50 HP, 3-phase induction motor with parameters listed in Table 3.1 using MATLAB. Results from a harmonic analysis of the induction motor operating at a speed of 1748.9 rpm while supplied by a six-step voltage source inverter with 180° conduction and a DC input voltage to the inverter of V_i=461V are shown in Table 3.2. This table also shows results from an EMAP simulation [50] for the same motor and operating conditions. Table 3.3 compares the results of the two simulations by showing the differences and percent errors between MATLAB analysis and EMAP. The EMAP values in Table 3.2 were assumed to be the base (or benchmark) values and the percent error listed in Table 3.3 was calculated as:

$$\%\,error = \frac{\left|EMAP\,value - MATLAB\,value\right|}{EMAP\,value}\,x100\%. \tag{3.25}$$

From Table 3.2 and Table 3.3, it can be observed that the MATLAB code produces results that are comparable to EMAP. The MATLAB code can be used in the analysis of an induction motor supplied by nonsinusoidal voltages.

3.3 Motor-Drive System Model

The proposed motor-drive system to be analyzed is shown in Figure 3.5. This figure shows a DC source connected to an inverter driving a three-phase induction motor with a load attached. In Figure 3.5, V_i is the inverter DC input voltage and I_i is the inverter DC input current.

TABLE 3.1
50 HP, 3-phase, Induction Motor Parameters

f = 60 Hz
number of poles = 4
$R_1 = 0.087\Omega$
$R_2 = 0.228\Omega$
$X_1 = 0.302\ \Omega$
$X_2 = 0.302\ \Omega$
$X_m = 13.08\ \Omega$
$J = 1.662$ kg-m^2
Machine Ratings: $V_{L\text{-}L}$= 460V Rated Speed = 1710 rpm Rated Torque = 200 N-m

Note: All quantities in Table 3.1 have been reflected to the stator.

TABLE 3.2
MATLAB AND EMAP SIX-STEP INVERTER RESULTS

		$\mathbf{V_{as}}$	$\mathbf{I_a}$		$\mathbf{V_{as}}$	$\mathbf{I_a}$
		(V)	(A)		(V)	(A)
Harmonic	**Slip**	(RMS)	(RMS)	**Slip**	(RMS)	(RMS)
Number	(EMAP)	(EMAP)	(EMAP)	(Matlab Code)	(Matlab Code)	(Matlab Code)
1	0.0284	207.53	29.75	0.0284	207.52	29.75
5	1.1943	41.52	13.85	1.1943	41.51	13.83
7	0.8612	29.66	7.07	0.8612	29.65	7.07
11	1.0883	18.89	2.87	1.0883	18.87	2.87
13	0.9253	16	2.06	0.9253	15.96	2.06
17	1.0572	12.25	1.21	1.0572	12.21	1.2
19	0.9489	10.97	0.97	0.9489	10.92	0.96
23	1.0422	9.08	0.66	1.0422	9.02	0.66
25	0.9611	8.37	0.56	0.9611	8.3	0.56
29	1.0335	7.23	0.42	1.0335	7.16	0.413
31	0.9687	6.78	0.37	0.9687	6.69	0.362

TABLE 3.3
DIFFERENCES AND PERCENT ERRORS

				Slip	V_{as}	I_a
Harmonic		**ΔVas**	**ΔI_a**	**% error**	**% error**	**% error**
Number	**ΔSlip**	(V)	(A)	(% of EMAP)	(% of EMAP)	(% of EMAP)
1	0	0.01	0	0	0.00	0.00
5	0	0.01	0.02	0	0.02	0.14
7	0	0.01	0	0	0.03	0.00
11	0	0.02	0	0	0.11	0.00
13	0	0.04	0	0	0.25	0.00
17	0	0.04	0.01	0	0.33	0.83
19	0	0.05	0.01	0	0.46	1.03
23	0	0.06	0	0	0.66	0.00
25	0	0.07	0	0	0.84	0.00
29	0	0.07	0.007	0	0.97	1.67
31	0	0.09	0.008	0	1.33	2.16

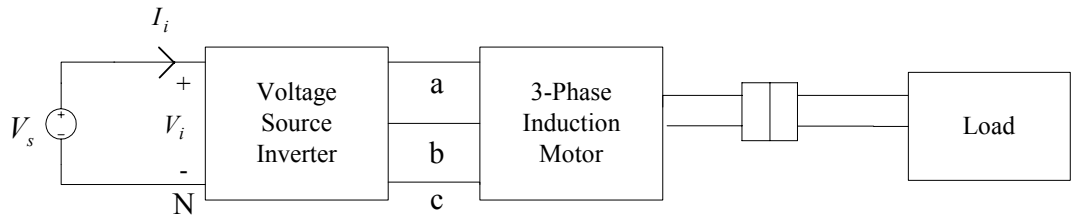

Figure 3.5. Motor-Drive System Model.

It is possible to develop a simplified model of the system shown in Figure 3.5 using the induction motor equivalent circuits and a power balance at the input and output terminals of the voltage source inverter. If a value of V_i is assumed at the input terminals of the inverter in Figure 3.5, a corresponding voltage value on the output side of the inverter can be found using a power balance as follows:

$$V_i I_i = \sum_{k=1}^{\infty} \frac{3}{2} V_k I_k \cos\theta_k \tag{3.26}$$

where V_k is the kth harmonic stator line-to-neutral voltage and I_k is the kth harmonic stator current. Power inverters used in practical applications are not 100% efficient and inverter losses would need to be included in a power balance. However, it should be noted that all inverters analyzed in this dissertation are assumed to be ideal inverters that are 100% efficient and (3.26) applies.

Assuming a value of V_i at the input terminals of the inverter will allow the line-to-neutral voltage at the input terminals of the induction motor to be found regardless of the PWM scheme employed in the inverter. The induction motor can be analyzed from knowledge of the line-to-neutral voltage and the load torque (or the line-to-neutral voltage and the motor speed) using the standard equations of the induction motor (3.1-3.24). Once the harmonic analysis of the induction motor has been completed for an assumed value of V_i, the corresponding value of the DC input current I_i can be found from (3.26).

For any value of V_i in Figure 3.5, a corresponding value of I_i can be found from (3.26) using the process described in the previous paragraph. If this process is continually repeated, a *V-I* load characteristic curve can be generated at the input terminals of the inverter in Figure 3.5. For a six-step inverter, PSPICE and MATLAB simulations have shown that the resulting *V-I* load characteristic curve has the following form:

$$V(I_i) = aI_i^2 + bI_i + c \tag{3.27}$$

where *a*, *b*, and *c* are constants determined using the *polyfit* command in MATLAB which fits a curve to the generated *V-I* data. To illustrate why a quadratic was used to curve fit the generated *V-I* data, the equations of the induction motor and six-step inverter (180° conduction) relationships were coded in MATLAB for the purpose of simulating

the system shown in Figure 3.5. The source voltage of Figure 3.5 was varied over a range of 478V-577V with all other parameters remaining unchanged. The motor used in the simulation was a 50 Hp, three-phase induction motor having parameters as listed in Table 3.1. A graph of the generated *V-I* data is shown in Figure 3.6. The data was initially fit with a linear curve in Excel as shown in Figure 3.7. Excel calculates an R^2 value when a curve fit is performed. The R^2 value is the square of the correlation coefficient. The correlation coefficient provides a measure of the reliability of the curve fit. The closer the R^2 value is to 1, the better the curve fit. The R^2 value for the linear curve fit was R^2=0.9973. The *V-I* data was then fit with a quadratic curve as shown in Figure 3.8. The R^2 value for the quadratic curve fit was R^2=1. The system in Figure 3.5 can now be replaced by a current-controlled voltage source having the characteristics of (3.27). The simplified model of the inverter drive system is shown in Figure 3.9. The current-controlled voltage source shown in this figure represents all system components to the right of V_i (inverter, motor, and load) in Figure 3.5.

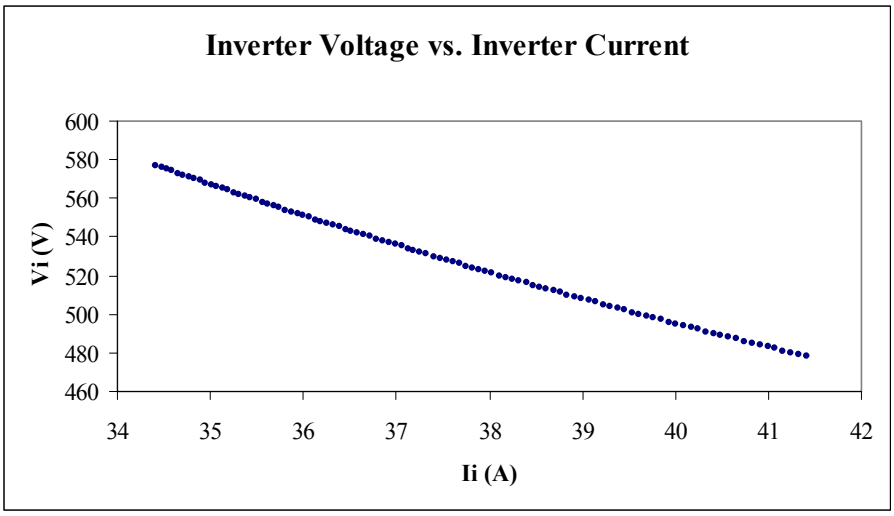

Figure 3.6: *V-I* Data Points.

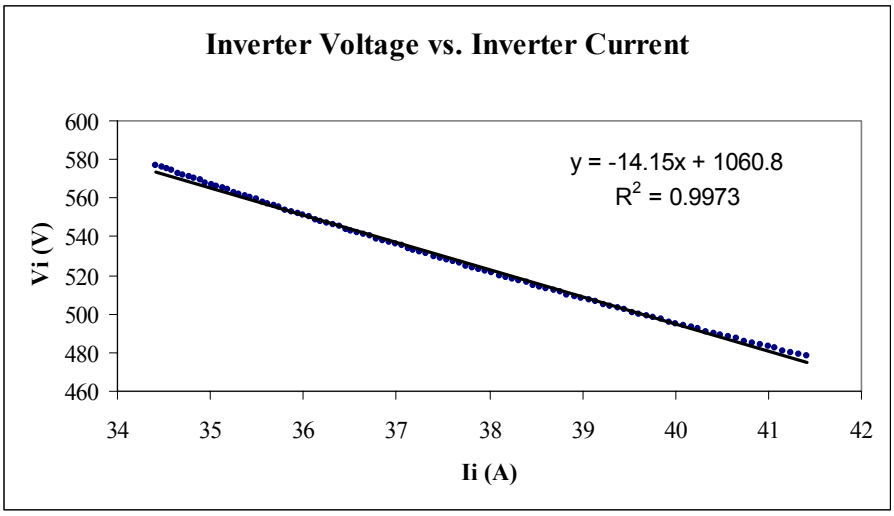

Figure 3.7: Linear Curve Fit.

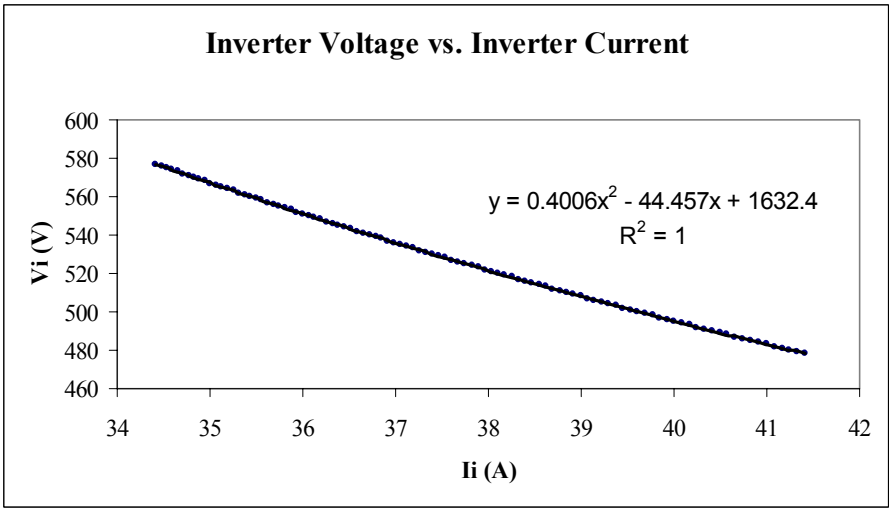

Figure 3.8: Quadratic Curve Fit.

3.3.1 Simplified Model Simulation Results

The purpose of this section is to demonstrate using PSPICE and MATLAB that the system shown in Figure 3.5 can be replaced by a V-I load characteristic curve that allows the inverter, motor, and load to be replaced by a current-controlled voltage source.

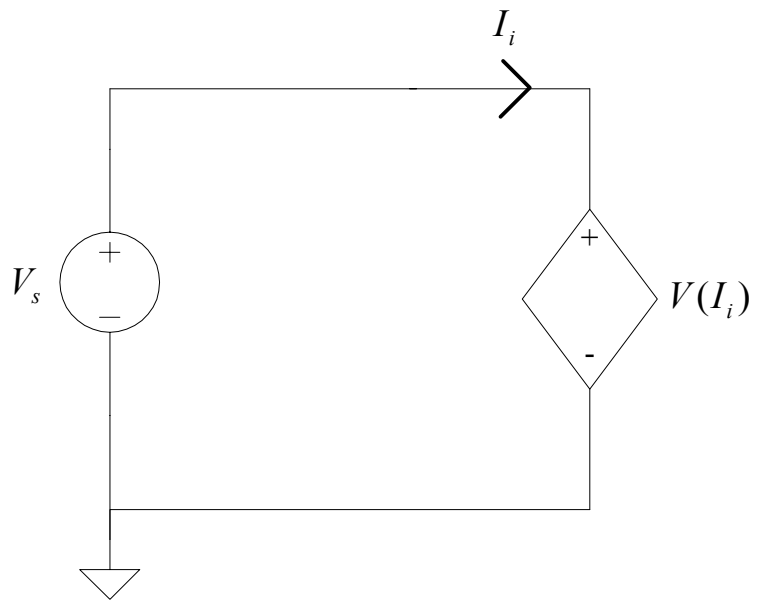

Figure 3.9: Simplified System Model.

Simulation results are shown for the six-step inverter (180° conduction), the two-level sinusoidal PWM inverter, and the space vector inverter.

3.3.2 Six-Step Inverter Results

The equations of the induction motor and six-step inverter (180° conduction) relationships were coded in MATLAB for the purpose of simulating the system shown in Figure 3.5. The source voltage of Figure 3.5 was varied over a range of 240V-480V with all other parameters remaining unchanged. The parameters of the motor studied were: R_1=0.25Ω, R_2=0.28Ω, X_1=0.754Ω, X_2=0.85Ω, X_m=18Ω, J=0.1kg m^2, P=4, and HP=5. Using MATLAB, the V-I characteristic found for this motor and inverter is:

$$V(I_i) = 0.7197 I_i^2 - 44.526 I_i + 904.26 . \quad (3.28)$$

A plot of (3.28) is shown in Figure 3.10. Equation (3.28) represents everything to the right of the inverter input voltage (V_i in Figure 3.5).

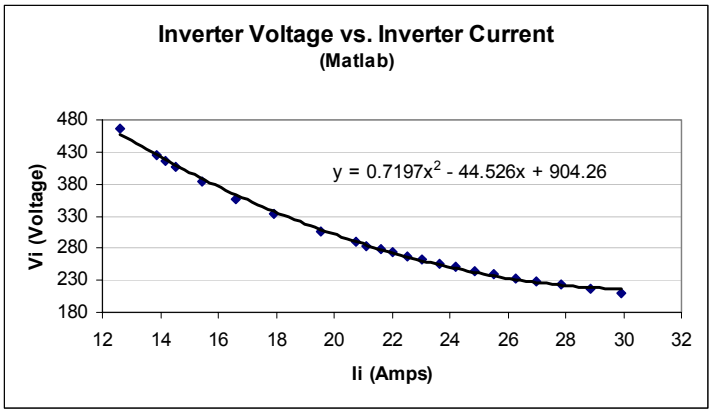

Figure 3.10: V-I Load Curve Produced From MATLAB Code.

A PSPICE model of the system shown in Figure 3.5 was simulated in order to produce a *V-I* characteristic curve. The load applied to the motor during simulations was a pulsed torque load with the following characteristics: T_L=30N-m, T=6s, and D=2/3. Where T is the pulse period and D is the duty cycle. During PSPICE simulation tests, the source voltage of Figure 3.5 was varied over a range of 240V-480V with all other parameters remaining unchanged. The motor parameters were the same as the ones used in the MATLAB analysis. After conducting each simulation, the DC components of the inverter input voltage and inverter input current were recorded. These components were used to produce a plot of inverter input voltage vs. inverter input current as shown in Figure 3.11. The *V-I* load characteristic curve that resulted is as follows:

$$V(I_i) = 0.7089I_i^2 - 44.106I_i + 899.34. \tag{3.29}$$

It can be seen from Figures 3.10 and 3.11 that the MATLAB code produces results that are similar to PSPICE. Based on these results, there is a potential to use a V-I characteristic curve to represent a motor-drive load in a DC power flow analysis.

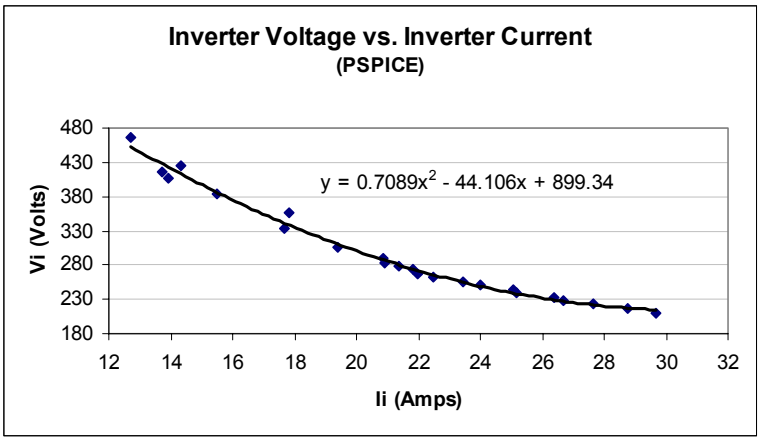

Figure 3.11: V-I Load Curve Produced From PSPICE Simulations.

3.3.3 Two-Level Sinusoidal PWM Inverter Simulation Results

The equations of the induction motor and the two-level sinusoidal PWM inverter were coded in MATLAB for the purpose of simulating the system shown in Figure 3.5. The source voltage of Figure 3.5 was varied over a range of 401V-500V with all other parameters remaining unchanged. The parameters of the 50 HP, three-phase, induction motor used to conduct the simulation study presented in this section are listed in Table 3.1. Other parameters used for the simulation were: $f_1 = 60$ Hz, m_a=1.4, m_f=15, and a constant load torque of T_L=100 N-m. The V-I characteristic curve that results from the MATLAB simulation is shown in Figure 3.12. A quadratic curve fit of the V-I characteristic curve is shown in Figure 3.13. Using the *polyfit* command in MATLAB, the following V-I characteristic can be developed for this motor and inverter:

$$V(I_i) = 0.24I_i^2 - 31I_i + 1300. \tag{3.30}$$

Equation (3.30) represents everything to the right of the inverter input voltage (V_i in Figure 3.5). As can be observed from Figure 3.13, the quadratic fit matches the original

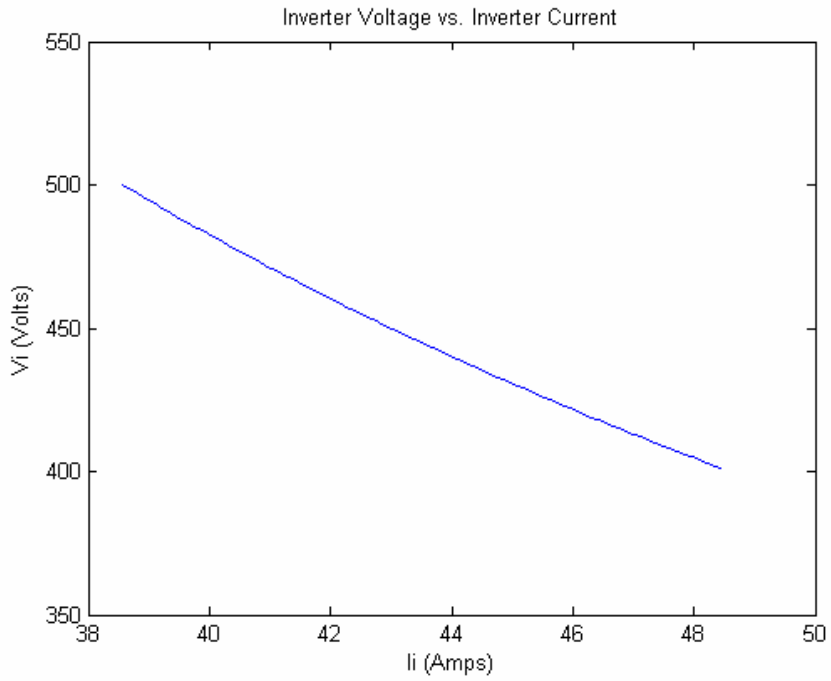

Figure 3.12: V-I Characteristic Curve for a Sinusoidal PWM Inverter with T_L=100 N-m.

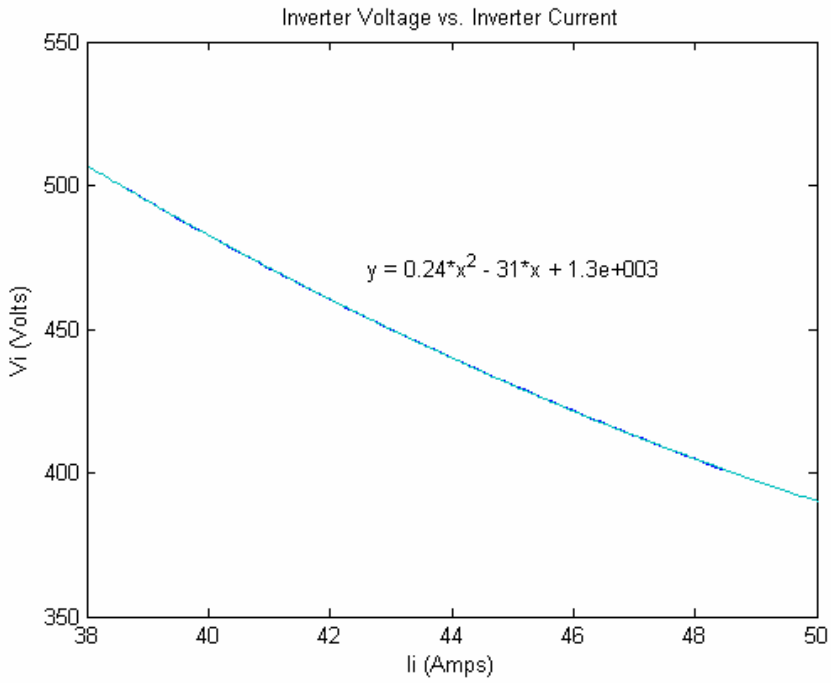

Figure 3.13: Quadratic Curve Fit for T_L=100 N-m.

curve very well, which illustrates that the V-I characteristic curve of a two-level sinusoidal PWM inverter drive can be fit with a quadratic curve with good results.

3.3.4 Space Vector PWM Inverter Simulation Results

The equations of the induction motor and the space vector PWM inverter were coded in MATLAB for the purpose of simulating the system shown in Figure 3.5. The source voltage of Figure 3.5 was varied over a range of 401V-500V with all other parameters remaining unchanged. The parameters of the 50 HP, three-phase, induction motor used to conduct the simulation study presented in this section are listed in Table 3.1. Other parameters used for the simulation were: $f_1 = 60$ Hz, M=0.7, m_f=15, and a constant load torque of T_L=80 N-m. The V-I characteristic curve that results from the MATLAB simulation is shown in Figure 3.14. A quadratic curve fit of the V-I characteristic curve is shown in Figure 3.15. Using the *polyfit* command in MATLAB, the V-I characteristic for this motor and inverter is as follows:

$$V(I_i) = 0.37I_i^2 - 39I_i + 1300. \tag{3.31}$$

Equation (3.31) represents everything to the right of the inverter input voltage (V_i in Figure 3.5). As can be observed from Figure 3.15, the quadratic fit matches the original curve very well. This shows that the V-I characteristic curve of a space vector PWM inverter drive can be fit with a quadratic curve with good results.

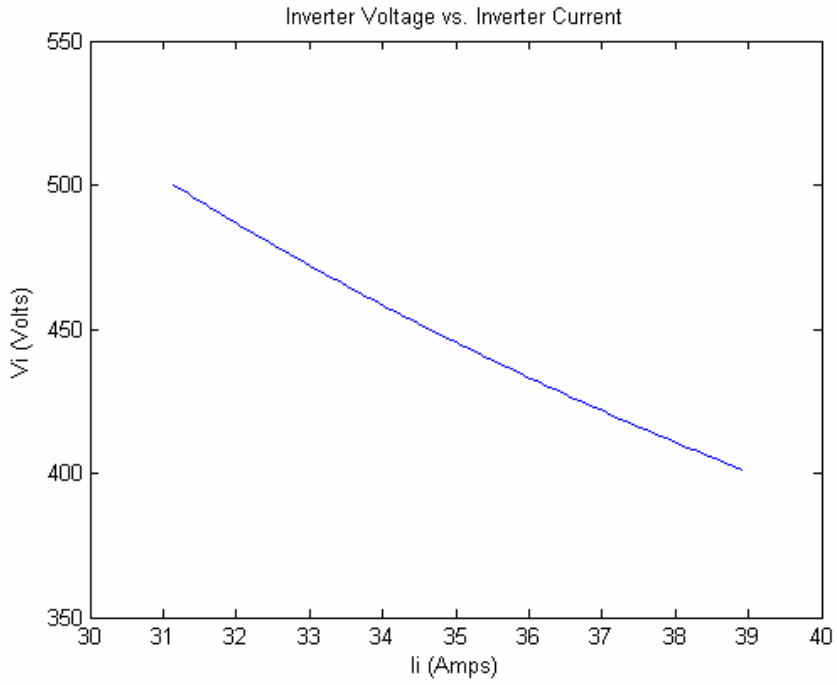

Figure 3.14: V-I Curve for a Space Vector PWM Inverter with T_L=80 N-m.

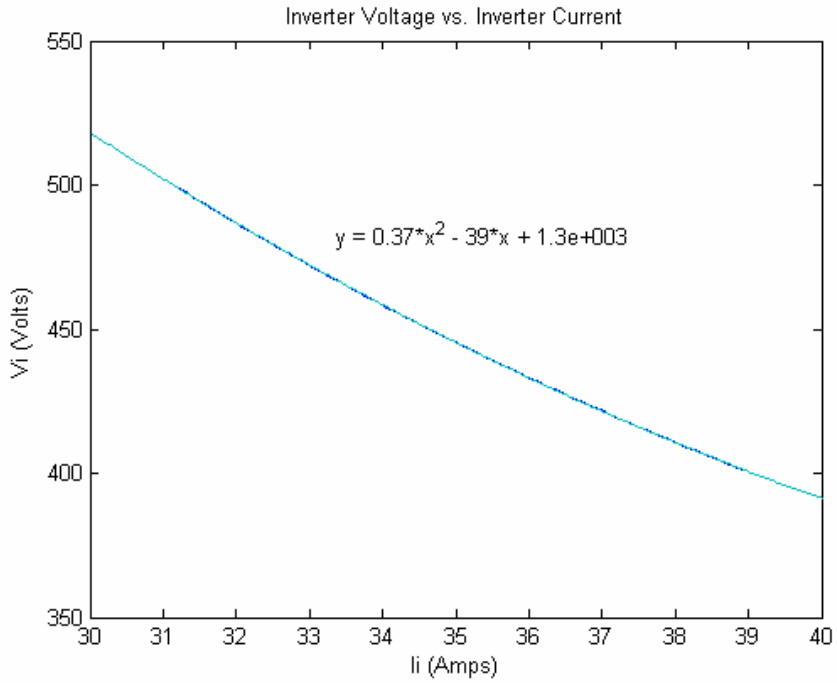

Figure 3.15: Quadratic Curve Fit for T_L=80 N-m.

3.4 Summary

A harmonic model of the induction motor operating under balanced, steady-state conditions was presented in this chapter. The model that was presented was shown to be applicable to induction motors supplied from nonsinusoidal sources. It was shown in this chapter that a motor-drive system can be represented by a simplified model. In this simplified model, a V-I load characteristic curve was established that allowed the inverter, motor, and load to be replaced by a current-controlled voltage source. It was determined through model simulations that the current-controlled voltage source should be a quadratic function of the inverter current. The model was shown to be applicable to six-step, sinusoidal PWM, and space vector PWM inverters.

CHAPTER 4

MULTIPLE MOTOR-DRIVE SYSTEMS

This chapter focuses on the analysis of a DC power system containing multiple motor-drive loads. An iterative procedure is presented that incorporates the simplified model from Chapter 3 into an algorithm used to perform a power flow analysis on a DC power system. The power flow algorithm presented is verified by conducting a power flow analysis on a 4-bus DC power system. The algorithm is then coded in MATLAB and power flow analyses are conducted on a 10-bus DC power system containing six-step inverter-drive loads and PWM inverter-drive loads. PSPICE simulation results are compared to the MATLAB power flow results for verification purposes. This chapter also includes a study conducted on an individual six-step inverter drive system that examines the effects on a system caused by larger line resistance values. A system with higher line resistances is simulated in PSPICE and the results are used to examine the effects of higher line resistances on a multiple motor-drive system. A 10-bus DC power system containing six-step inverter drive loads and higher line resistance values is also investigated. The chapter concludes with a summary of simulation results and findings from the study conducted on a system containing higher line resistance values.

4.1 DC Power Flow

A DC power system containing motor-drive loads is shown in Figure 4.1. The simplified model discussed in the previous chapter can be extended to a system containing more than one motor drive. MATLAB can be used to produce a *V-I* load characteristic curve for each motor drive load in a DC power system that can be incorporated into an iterative procedure to conduct a power flow analysis.

The network shown in Figure 4.1 can be represented as [51]:

$$\widetilde{I} = G\widetilde{V} \tag{4.1}$$

where $\widetilde{I}$ is the current vector *(nx*1*)*, *G* is the network conductance matrix *(nxn)*, $\widetilde{V}$ is the bus voltage vector *(nx*1*)*, and *n* is the number of buses. The system studied contains motor-drive loads only and each bus voltage element of $\widetilde{V}$ (except for the swing bus) will be of the same form as (3.26):

$$\widetilde{V} = \begin{bmatrix} V_1 \\ V_2 \\ V_3 \\ \vdots \\ V_n \end{bmatrix} = \begin{bmatrix} V_1 \\ a_2 I_2^2 + b_2 I_2 + c_2 \\ a_3 I_3^2 + b_3 I_3 + c_3 \\ \vdots \\ a_n I_n^2 + b_n I_n + c_n \end{bmatrix} \tag{4.2}$$

where bus 1 was chosen as the swing bus. Note that the currents in (4.2) are the DC inverter input currents of each individual motor drive load at the specified bus. The conductance matrix can be formed using the following rules [52]:

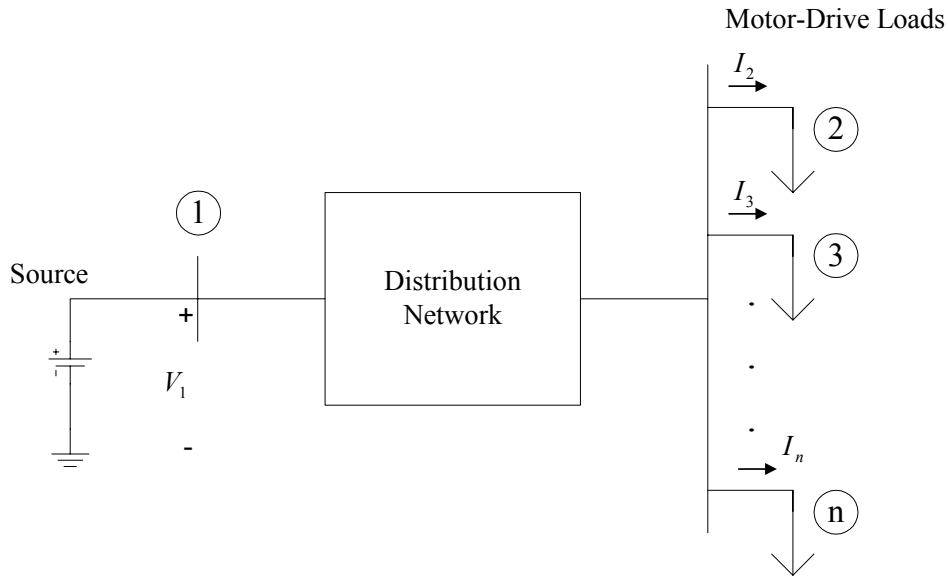

Figure 4.1: DC Power System Model.

$$G_{ij} = -\frac{1}{R_{ij}} \quad , \quad (i \neq j), \tag{4.3}$$

$$G_{ii} = \sum_{\substack{j=1 \\ j \neq i}}^{n} \frac{1}{R_{ij}}, \tag{4.4}$$

where R_{ij} is the line resistance between bus number i and bus number j.

When the conductance matrix has been formed and the DC network equations placed in the form of (4.1), Kron reduction can be used to eliminate all non-contributing buses using the following formula [47]:

$$G_{ij}^{new} = G_{ij} - \frac{G_{ik} G_{kj}}{G_{kk}} \quad , \quad i, j = 1,..,n \ , \ i, j \neq k \ . \tag{4.5}$$

It should be noted that non-contributing buses are buses that have no external load or source connected. The voltage is normally not of interest at a non-contributing bus, and the bus can be eliminated. A Kron-reduced system can now be formed as follows:

$$\widetilde{I}_{Kron} = G_{Kron}\widetilde{V}_{Kron} \tag{4.6}$$

where $\widetilde{I}_{Kron}$ is an *(n-m)x*1 vector, G_{Kron} is an *(n-m)x(n-m)* matrix, $\widetilde{V}_{Kron}$ is an *(n-m)x*1 vector, and *m* is the number of non-contributing buses.

An iterative method based on the Newton-Raphson method [51] is well suited to solve for the load currents, because (4.6) represents a system of simultaneous nonlinear algebraic equations [53]. Moving all of the variables in (4.6) to one side and setting them equal to zero will produce a system of *(n-m)* nonlinear equations in *(n-m)* unknowns as:

$$\begin{aligned} &f_1(I_3, I_4, \ldots, I_{n-m}) = 0, \\ &f_3(I_3, I_4, \ldots, I_{n-m}) = 0, \\ &\qquad \vdots \\ &f_{n-m}(I_3, I_4, \ldots, I_{n-m}) = 0 \end{aligned} \tag{4.7}$$

where the notation in (4.7) is based on the assumption that bus 1 is the swing bus and bus 2 is a non-contributing bus. In vector form, (4.7) becomes:

$$\widetilde{f}_{n-m}^{(k)}(\widetilde{I}_{n-m}^{(k)}) = 0 \tag{4.8}$$

where *k* is the k^{th} iteration value. The system Jacobian matrix (based on (4.7)) is:

$$J^{(k)} = \begin{bmatrix} \dfrac{\partial f_1^{(k)}}{\partial I_3} & \dfrac{\partial f_1^{(k)}}{\partial I_4} & \cdots & \dfrac{\partial f_1^{(k)}}{\partial I_{n-m}} \\ \dfrac{\partial f_3^{(k)}}{\partial I_3} & \dfrac{\partial f_3^{(k)}}{\partial I_4} & \cdots & \dfrac{\partial f_3^{(k)}}{\partial I_{n-m}} \\ \vdots & \vdots & & \vdots \\ \dfrac{\partial f_{n-m}^{(k)}}{\partial I_3} & \dfrac{\partial f_{n-m}^{(k)}}{\partial I_4} & \cdots & \dfrac{\partial f_{n-m}^{(k)}}{\partial I_{n-m}} \end{bmatrix}. \tag{4.9}$$

The load current correction for the k^{th} iteration is:

$$\left[\Delta\widetilde{I}_{n-m}\right]^{(k)} = -\left[J^{(k)}\right]^{-1}\Big|_{\widetilde{I}_{n-m}^{(k)}}\left[\widetilde{f}_{n-m}^{(k)}(\widetilde{V}_1, \widetilde{I}_{n-m}^{(k)})\right]\Big|_{\widetilde{I}_{n-m}^{(k)}} . \tag{4.10}$$

The values of the new updated load currents are:

$$\widetilde{I}_{n-m}^{(k+1)} = \widetilde{I}_{n-m}^{(k)} + \Delta\widetilde{I}_{n-m}^{(k)} . \tag{4.11}$$

Once the initial estimates for the load currents are made, (4.8-4.11) can be used to iteratively compute the load currents of a DC power system containing motor drive loads. Convergence of the power flow iterations is based on the following criteria:

$$\left|\widetilde{I}_{n-m}^{(k)} - \widetilde{I}_{n-m}^{(k-1)}\right| < \varepsilon \tag{4.12}$$

where ε is the convergence tolerance. To determine convergence, each current vector element of the present iteration is compared to the previous iteration element value. When the absolute value of the difference between these elements is less than ε in (4.12), the currents have converged. After the currents have converged, the individual bus voltages can be found using (4.2).

4.2 Verification of the Power Flow Algorithm

The 4-bus system in Figure 4.2 is utilized to demonstrate that the iterative method described in Section 4.1 can be used to conduct power flow studies on a DC power system containing motor-drive loads. Bus 1 in Figure 4.2 is the swing bus, bus 2 is a non-contributing bus, and bus 3 and bus 4 are load buses with motor-drive loads attached. The line resistances and load torques for the system are shown in Table 4.1. The motors used in the system were 50 Hp motors with parameters as listed in Table 3.1. The inverters used in the system in Figure 4.2 are six-step voltage source inverters with 180° conduction, and the swing bus in Figure 4.2 has a value of 550V.

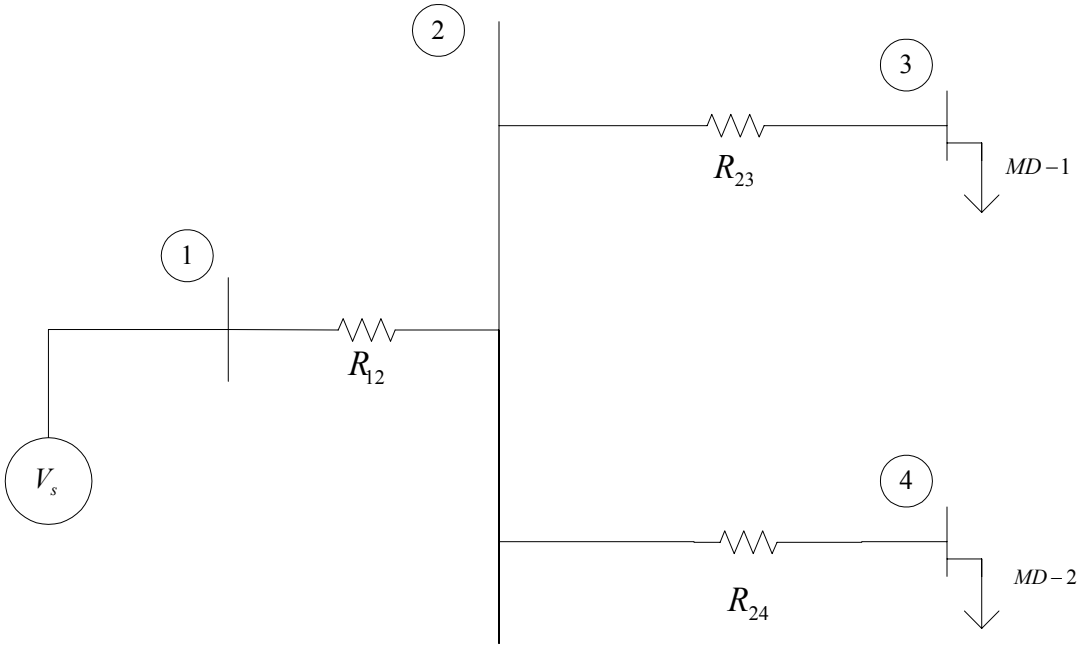

Figure 4.2: Four-Bus DC Power System.

TABLE 4.1
4-BUS SYSTEM LINE RESISTANCES AND LOAD TORQUES

Bus Number	Load Torque (N-m)		Line Section	Line Resistance (Ω)
1				
2			1 - 2	0.1
3	75		2 - 3	0.4
4	40		2 - 4	0.6

To begin the analysis of the system in Figure 4.2, the network conductance matrix must be formed using the rules listed in (4.3) and (4.4). Using these rules, the conductance matrix entries are:

$$G_{12} = -\frac{1}{R_{12}} = -\frac{1}{0.1}, \tag{4.13}$$

$$G_{12} = G_{21} = -10\,, \tag{4.14}$$

$$G_{13} = G_{31} = 0\,, \tag{4.15}$$

$$G_{14} = G_{41} = 0\,, \tag{4.16}$$

$$G_{22} = \frac{1}{R_{12}} + \frac{1}{R_{23}} + \frac{1}{R_{24}} = \frac{1}{0.1} + \frac{1}{0.4} + \frac{1}{0.6}\,, \tag{4.17}$$

$$G_{22} = 14.1667\,, \tag{4.18}$$

$$G_{23} = -\frac{1}{R_{23}} = -\frac{1}{0.4}\,, \tag{4.19}$$

$$G_{23} = G_{32} = -2.5\,, \tag{4.20}$$

$$G_{24} = -\frac{1}{R_{24}} = -\frac{1}{0.6}\,, \tag{4.21}$$

$$G_{24} = G_{42} = -1.6667\,, \tag{4.22}$$

$$G_{33} = \frac{1}{R_{23}} = \frac{1}{0.4}\,, \tag{4.23}$$

$$G_{33} = 2.5\,, \tag{4.24}$$

$$G_{34} = G_{43} = 0\,, \tag{4.25}$$

$$G_{44} = \frac{1}{R_{24}} = \frac{1}{0.6}\,, \tag{4.26}$$

$$G_{44} = 1.6667\,. \tag{4.27}$$

From these results, the conductance matrix for the system in Figure 4.2 can be formed as follows:

$$G = \begin{bmatrix} 10 & -10 & 0 & 0 \\ -10 & 14.1667 & -2.5 & -1.6667 \\ 0 & -2.5 & 2.5 & 0 \\ 0 & -1.6667 & 0 & 1.6667 \end{bmatrix}. \tag{4.28}$$

Since bus 2 is a non-contributing bus, it can now be eliminated using the Kron reduction formula in (4.5). The entries of the Kron reduced conductance matrix can be found as follows:

$$G_{11}^{new} = G_{11} - \frac{G_{12}G_{21}}{G_{22}} = 10 - \frac{(-10)(-10)}{14.1667}, \tag{4.29}$$

$$G_{11}^{new} = 2.9412, \tag{4.30}$$

$$G_{13}^{new} = G_{13} - \frac{G_{12}G_{23}}{G_{22}} = 0 - \frac{(-10)(-2.5)}{14.1667}, \tag{4.31}$$

$$G_{13}^{new} = G_{31}^{new} = -1.7647, \tag{4.32}$$

$$G_{14}^{new} = G_{14} - \frac{G_{12}G_{24}}{G_{22}} = 0 - \frac{(-10)(-1.6667)}{14.1667}, \tag{4.33}$$

$$G_{14}^{new} = G_{41}^{new} = -1.1765, \tag{4.34}$$

$$G_{33}^{new} = G_{33} - \frac{G_{32}G_{23}}{G_{22}} = 2.5 - \frac{(-2.5)(-2.5)}{14.1667}, \tag{4.35}$$

$$G_{33}^{new} = 2.0588, \tag{4.36}$$

$$G_{34}^{new} = G_{34} - \frac{G_{32}G_{24}}{G_{22}} = 0 - \frac{(-2.5)(-1.6667)}{14.1667}, \tag{4.37}$$

$$G_{34}^{new} = G_{43}^{new} = -0.2941, \tag{4.38}$$

$$G_{44}^{new} = G_{44} - \frac{G_{42}G_{24}}{G_{22}} = 1.6667 - \frac{(-1.6667)(-1.6667)}{14.1667}, \tag{4.39}$$

$$G_{44}^{new} = 1.4706 . \tag{4.40}$$

The Kron reduced matrix is:

$$G_{Kron} = \begin{bmatrix} 2.9412 & -1.7647 & -1.1765 \\ -1.7647 & 2.0588 & -0.2941 \\ -1.1765 & -0.2941 & 1.4706 \end{bmatrix}. \tag{4.41}$$

Bus 2 has now been eliminated from (4.1), and the system can be expressed as shown in (4.6). Because only the load buses are of interest in this example problem, the entire swing bus row of the Kron-reduced conductance matrix and the current for bus 1 can be removed. This leaves only the two load bus currents to be solved for. The new system can be expressed as:

$$\begin{bmatrix} I_3 \\ I_4 \end{bmatrix} = \begin{bmatrix} -1.7647 & 2.0588 & -0.2941 \\ -1.1765 & -0.2941 & 1.4706 \end{bmatrix} \begin{bmatrix} 550 \\ V_3 \\ V_4 \end{bmatrix}. \tag{4.42}$$

The loads in the system in Figure 4.2 are motor-drive loads and the voltages V_3 and V_4 have the same form as the voltages shown in (4.2). This means that the loads at buses 3 and 4 can be replaced by current-controlled voltage sources as demonstrated in Chapter 3. All that is required now is to find the V-I load characteristic for each individual motor-drive load in Figure 4.2. MATLAB is utilized to produce the V-I characteristic curves for the two motor-drive loads in the system. The equations of the induction motor and the six-step inverter relationships were coded in MATLAB, and all of the known parameters were entered. To develop the V-I characteristic curve for the 75 N-m constant torque load at bus 3, the voltage at bus 3 at the inverter input terminals was varied over a range of 478V-577V with all other parameters remaining unchanged. The V-I load characteristic curve produced is shown in Figure 4.3. The *polyfit* command in

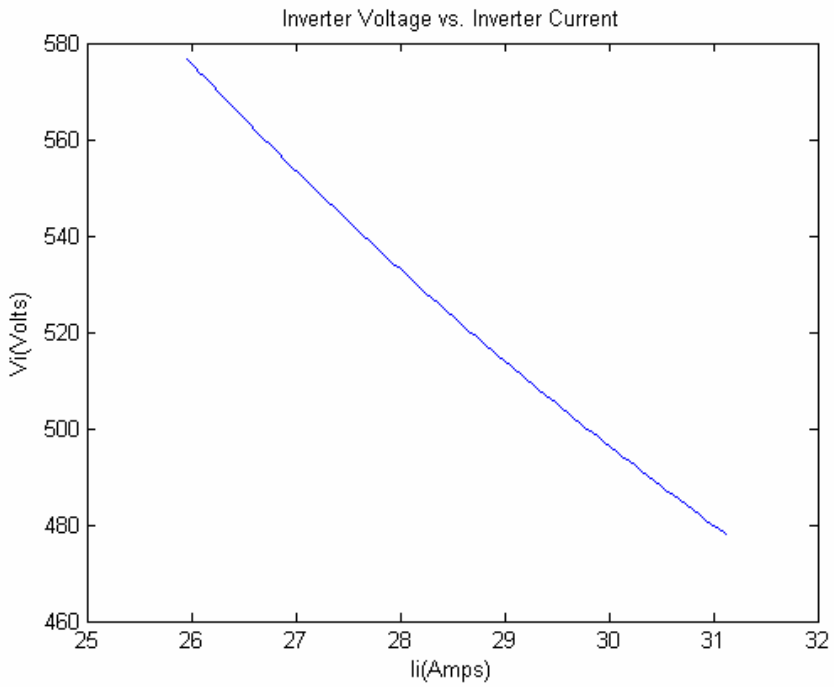

Figure 4.3: V-I Characteristic Curve for T_L=75 N-m.

MATLAB was used to determine the coefficients of the quadratic curve fit of the V-I data. The V-I characteristic for the motor-drive load at bus 3 was:

$$V_3(I_3) = 0.73235I_3^2 - 60.86I_3 + 1{,}663. \tag{4.43}$$

The quadratic curve fit of Figure 4.3 is shown in Figure 4.4. To produce the V-I characteristic curve for the 40 N-m constant torque load at bus 4, the voltage at the inverter terminals was varied over a range of 478V-577V with all other parameters unchanged. The V-I load characteristic curve produced is shown in Figure 4.5. The *polyfit* command was again used to find the coefficients of the quadratic curve fit of the V-I data. The V-I characteristic for the motor-drive load at bus 4 was:

$$V_4(I_4) = 2.7951I_4^2 - 123.64I_4 + 1{,}767.3. \tag{4.44}$$

The quadratic curve fit of Figure 4.5 is shown in Figure 4.6. The relationships in (4.43) and (4.44) can be substituted back into (4.42) and put into the form of (4.9) as follows:

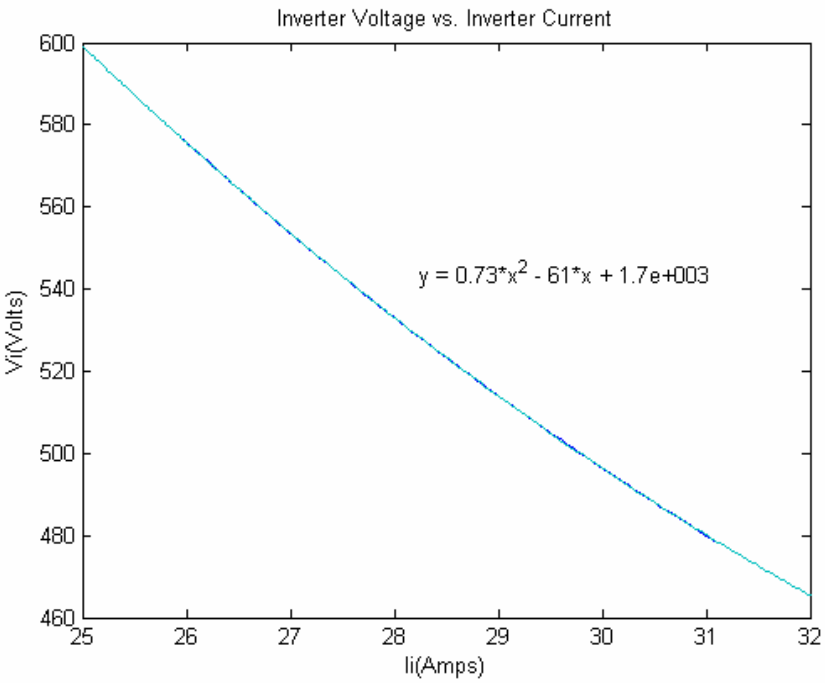

Figure 4.4: Quadratic Curve Fit for T_L=75 N-m.

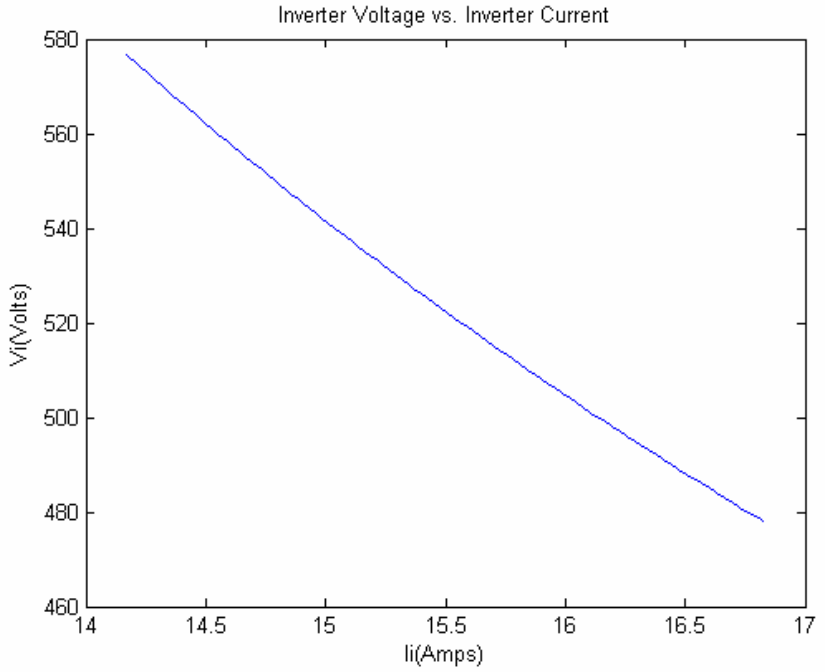

Figure 4.5: V-I Characteristic Curve for T_L=40 N-m.

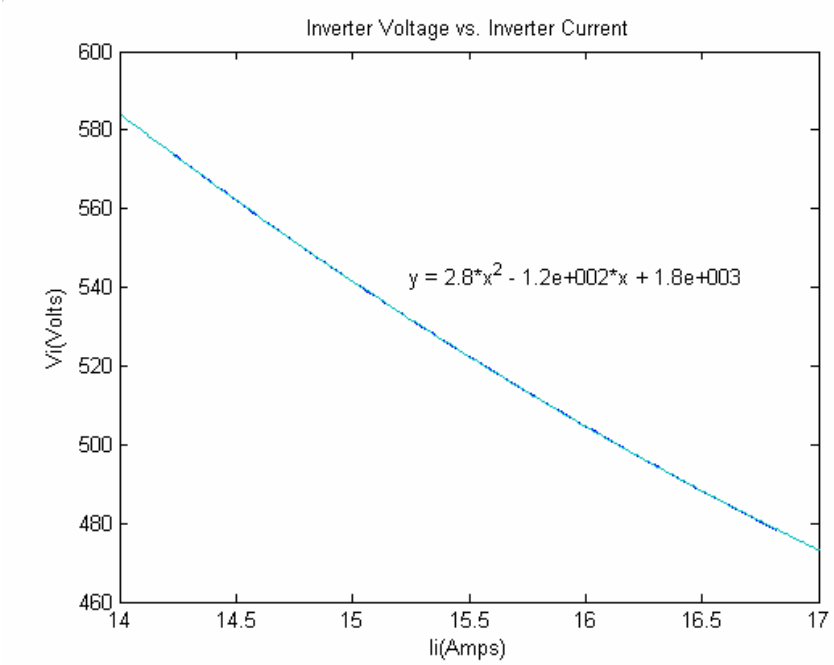

Figure 4.6: Quadratic Curve Fit for T_L=40 N-m.

$$f_3(I_3, I_4) = 1.5078I_3^2 - 124.2986I_3 - 0.822I_4^2 + 36.3625I_4 + 1{,}933.4365, \tag{4.45}$$

$$f_4(I_3, I_4) = -0.2154I_3^2 + 17.8989I_3 + 4.1105I_4^2 - 180.825I_4 + 1{,}462.8281. \tag{4.46}$$

The elements of the Jacobian matrix can be found using (4.9):

$$\frac{\partial f_3}{\partial I_3} = 3.0156I_3 - 124.2986, \tag{4.47}$$

$$\frac{\partial f_3}{\partial I_4} = -1.644I_4 + 36.3625, \tag{4.48}$$

$$\frac{\partial f_4}{\partial I_3} = -0.4308I_3 + 17.8989, \tag{4.49}$$

$$\frac{\partial f_4}{\partial I_4} = 8.221I_4 - 180.825. \tag{4.50}$$

The Jacobian matrix can now be formed as follows:

$$J = \begin{bmatrix} 3.0156I_3 - 124.2986 & -1.644I_4 + 36.3625 \\ -0.4308I_3 + 17.8989 & 8.221I_4 - 180.825 \end{bmatrix}. \tag{4.51}$$

An initial estimate can be made for the currents at buses 3 and 4. The two load buses were estimated to be at 530V each based on the swing bus having a value of 550V. The value of 530V was placed into (4.43) to determine the initial estimate for I_3 as:

$$I_3^{(0)} = \frac{-b_3 - \sqrt{b_3^2 - 4a_3(c_3 - V_3^{(0)})}}{2a_3}, \tag{4.52}$$

$$I_3^{(0)} = \frac{60.86 - \sqrt{(-60.86)^2 - 4(0.73235)(1663 - 530)}}{2(0.73235)}, \tag{4.53}$$

$$I_3^{(0)} = 28.16\,A. \tag{4.54}$$

The initial estimate for I_4 was determined to be:

$$I_4^{(0)} = \frac{123.64 - \sqrt{(-123.64)^2 - 4(2.7951)(1767.3 - 530)}}{2(2.7951)}, \tag{4.55}$$

$$I_4^{(0)} = 15.3\,A. \tag{4.56}$$

It should be noted that the currents could have been arbitrarily chosen and the system currents would still converge. This is due to the fact that Newton-Raphson based methods have a fast rate of convergence and produce accurate results unless the first estimates of the currents are very poor [51]. The convergence tolerance for the power flow analysis was selected to be ε = 0.001A. At this point, all essential information is known and the iterations can now begin.

First Iteration:

The initial current estimates from (4.54) and (4.56) can be substituted into (4.51) to find $J^{(0)}$ as:

$$J^{(0)} = \begin{bmatrix} -39.3793 & 11.2093 \\ 5.7676 & -55.0437 \end{bmatrix}. \tag{4.57}$$

The initial current estimates from (4.54) and (4.56) can then be substituted into (4.45) to find $f_3^{(0)}(I_3,I_4)$:

$$f_3^{(0)}(I_3, I_4) = -7.2241. \tag{4.58}$$

The initial current estimates from (4.54) and (4.56) can be substituted into (4.46) to find $f_4^{(0)}(I_3,I_4)$ as follows:

$$f_4^{(0)}(I_3, I_4) = -8.3435. \tag{4.59}$$

The values in (4.57), (4.58), and (4.59) can be substituted into (4.10) to find the current corrections as:

$$\begin{bmatrix} \Delta I_3 \\ \Delta I_4 \end{bmatrix}^{(0)} = \begin{bmatrix} -0.2336 \\ -0.1761 \end{bmatrix}. \tag{4.60}$$

The updated current values can be found using (4.11):

$$\begin{bmatrix} I_3 \\ I_4 \end{bmatrix}^{(1)} = \begin{bmatrix} 28.16 \\ 15.3 \end{bmatrix} + \begin{bmatrix} -0.2336 \\ -0.1761 \end{bmatrix}, \tag{4.61}$$

$$\begin{bmatrix} I_3 \\ I_4 \end{bmatrix}^{(1)} = \begin{bmatrix} 27.9264A \\ 15.1239A \end{bmatrix}. \tag{4.62}$$

The convergence tolerance can be checked using (4.12) as follows:

$$\begin{vmatrix} 27.9264 - 28.16 \\ 15.1239 - 15.3 \end{vmatrix} < 0.001, \tag{4.63}$$

$$\begin{vmatrix} 0.2336 \\ 0.1761 \end{vmatrix} < 0.001. \tag{4.64}$$

It can be seen that the statement in (4.64) is not satisfied. So, more iterations must be performed.

Second Iteration:

The first iteration current values can be substituted into (4.51) to find $J^{(1)}$ as:

$$J^{(1)} = \begin{bmatrix} -40.0837 & 11.4988 \\ 5.8682 & -56.4914 \end{bmatrix}. \tag{4.65}$$

The first iteration current values from (4.62) can now be substituted into (4.45) to find $f_3^{(1)}(I_3,I_4)$ as:

$$f_3^{(1)}(I_3, I_4) = 0.0577. \tag{4.66}$$

The first iteration current values from (4.62) can be substituted into (4.46) to find $f_4^{(1)}(I_3,I_4)$ as follows:

$$f_4^{(1)}(I_3, I_4) = 0.1181. \tag{4.67}$$

The values in (4.65), (4.66), and (4.67) can be substituted into (4.10) to find the current corrections as:

$$\begin{bmatrix} \Delta I_3 \\ \Delta I_4 \end{bmatrix}^{(1)} = \begin{bmatrix} 0.0021 \\ 0.0023 \end{bmatrix}. \tag{4.68}$$

The updated current values can be found using (4.11):

$$\begin{bmatrix} I_3 \\ I_4 \end{bmatrix}^{(2)} = \begin{bmatrix} 27.9264 \\ 15.1239 \end{bmatrix} + \begin{bmatrix} 0.0021 \\ 0.0023 \end{bmatrix}, \tag{4.69}$$

$$\begin{bmatrix} I_3 \\ I_4 \end{bmatrix}^{(2)} = \begin{bmatrix} 27.9285A \\ 15.1262A \end{bmatrix}. \tag{4.70}$$

The convergence tolerance can be checked using (4.12) as follows:

$$\left|\begin{matrix}27.9285-27.9264\\15.1239-15.1262\end{matrix}\right|<0.001, \tag{4.71}$$

$$\left|\begin{matrix}0.0021\\0.0023\end{matrix}\right|<0.001. \tag{4.72}$$

It can be seen that the statement in (4.72) is not satisfied. So, another iteration must be performed.

Third Iteration:

The second iteration current values can be substituted into (4.51) to find $J^{(2)}$ as:

$$J^{(2)}=\begin{bmatrix}-40.0774 & 11.495\\ 5.8673 & -56.4725\end{bmatrix}. \tag{4.73}$$

The second iteration current values from (4.70) can now be substituted into (4.45) to find $f_3^{(2)}(I_3,I_4)$ as:

$$f_3^{(2)}(I_3,I_4)=-0.000009. \tag{4.74}$$

The second iteration current values from (4.70) can be substituted into (4.46) to find $f_4^{(2)}(I_3,I_4)$ as follows:

$$f_4^{(2)}(I_3,I_4)=0.0305. \tag{4.75}$$

The values in (4.73), (4.74), and (4.75) can be substituted into (4.10) to find the current corrections as:

$$\begin{bmatrix}\Delta I_3\\ \Delta I_4\end{bmatrix}^{(2)}=\begin{bmatrix}0.00016\\0.00056\end{bmatrix}. \tag{4.76}$$

The updated current values can be found using (4.11):

$$\begin{bmatrix}I_3\\ I_4\end{bmatrix}^{(3)}=\begin{bmatrix}27.9285\\15.1262\end{bmatrix}+\begin{bmatrix}0.00016\\0.00056\end{bmatrix}, \tag{4.77}$$

$$\begin{bmatrix} I_3 \\ I_4 \end{bmatrix}^{(3)} = \begin{bmatrix} 27.9287A \\ 15.1268A \end{bmatrix}. \tag{4.78}$$

The convergence tolerance can be checked using (4.12) as follows:

$$\left| \begin{matrix} 27.9287 - 27.9285 \\ 15.1268 - 15.1262 \end{matrix} \right| < 0.001, \tag{4.79}$$

$$\left| \begin{matrix} 0.0002 \\ 0.0006 \end{matrix} \right| < 0.001. \tag{4.80}$$

The statement in (4.80) has now been satisfied. Therefore, the currents have converged and no other iterations are necessary. After three iterations, the currents converged to the following values: I_3=27.9287 A and I_4=15.1268 A. These current values can now be substituted into (4.43) and (4.44) to solve for the bus voltages at buses 3 and 4 as follows:

$$V_3(27.9287) = 0.73235(27.9287)^2 - 60.86(27.9287) + 1{,}663, \tag{4.81}$$

$$V_3(27.9287) = 534.5013V, \tag{4.82}$$

$$V_4(15.1268) = 2.7951(15.1268)^2 - 123.64(15.1268) + 1{,}767.3, \tag{4.83}$$

$$V_4(15.1268) = 536.5974V. \tag{4.84}$$

After three iterations, the voltages converged to the following values: V_3=534.5013 V and V_4=536.5974 V.

For comparison purposes, the system in Figure 4.2 was simulated in PSPICE. The PSPICE model of the system is shown in Figure 4.7. Each block in Figure 4.7 contains an induction motor drive as shown in Figure 4.8. The induction motor part shown in Figure 4.9 was developed by Dr. Michael Giesselmann [42] and used in all PSPICE simulations of the system in Figure 4.2 due to the accuracy of the induction motor model represented by the part. The part in Figure 4.9 is only the top-level portion of the

PSPICE induction motor part. All of the parameters in the PSPICE model were the same as the ones used for the hand calculations. The results of the PSPICE simulation are shown in Table 4.2, which also lists the converged currents and voltages from the hand calculations. As can be observed from the table, the results from the hand calculations match the PSPICE results very well. Therefore, the iterative procedure presented in this section is comparable in accuracy to PSPICE, which indicates that this algorithm can be used to analyze multiple-bus DC power systems with reasonable results.

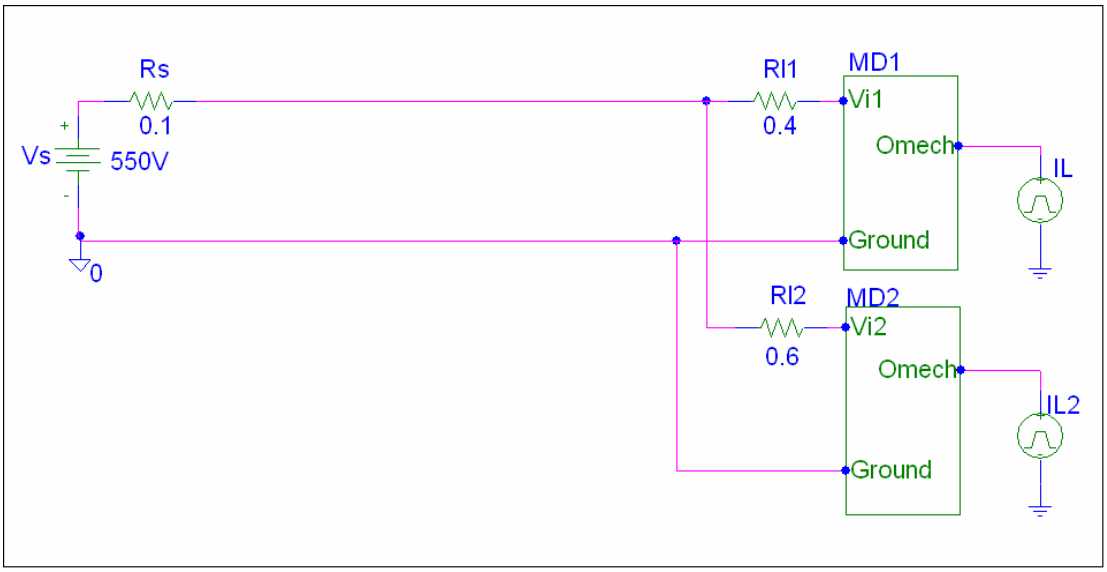

Figure 4.7: PSPICE 4-bus System Model.

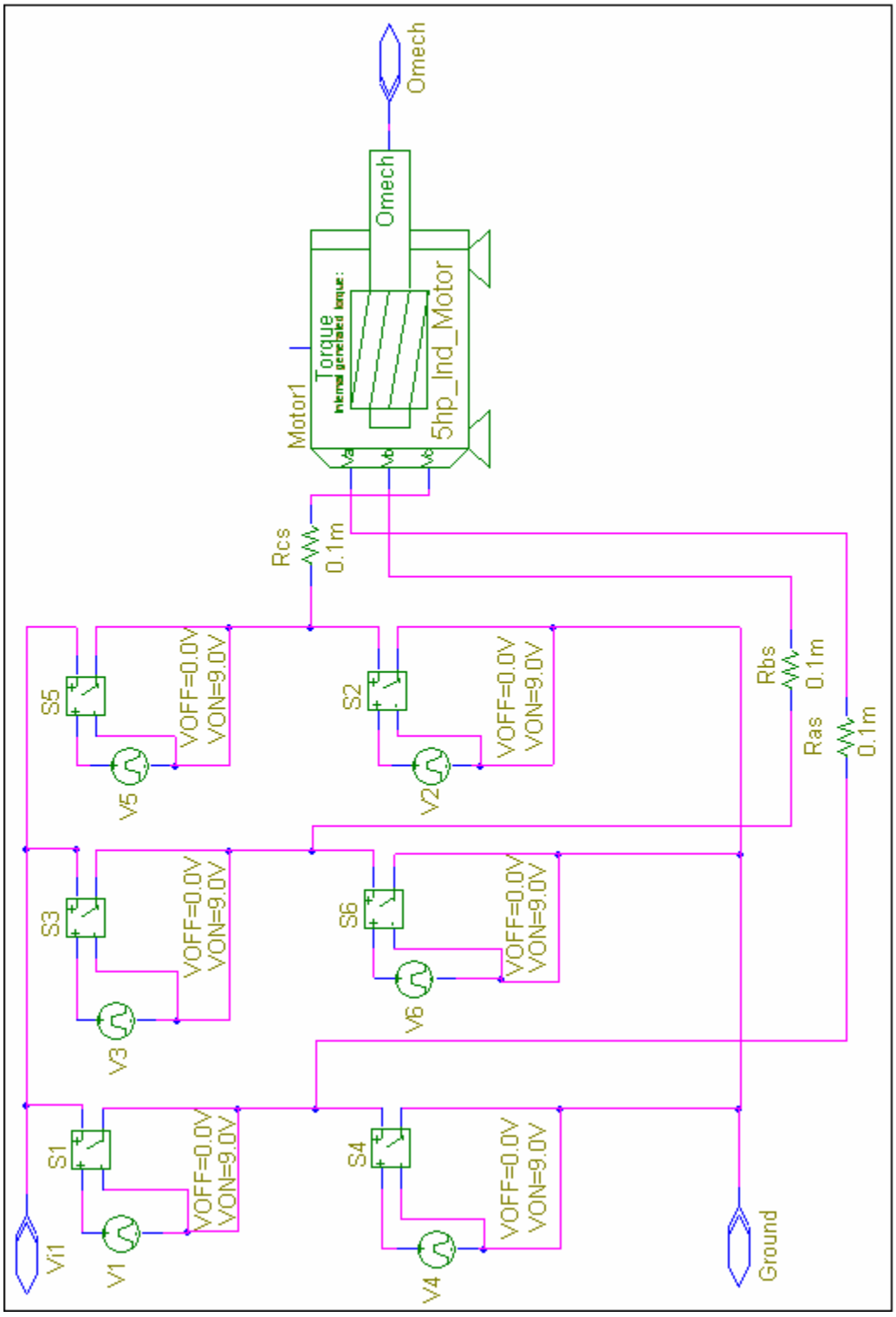

Figure 4.8: PSPICE Six-Step Motor-Drive Model.

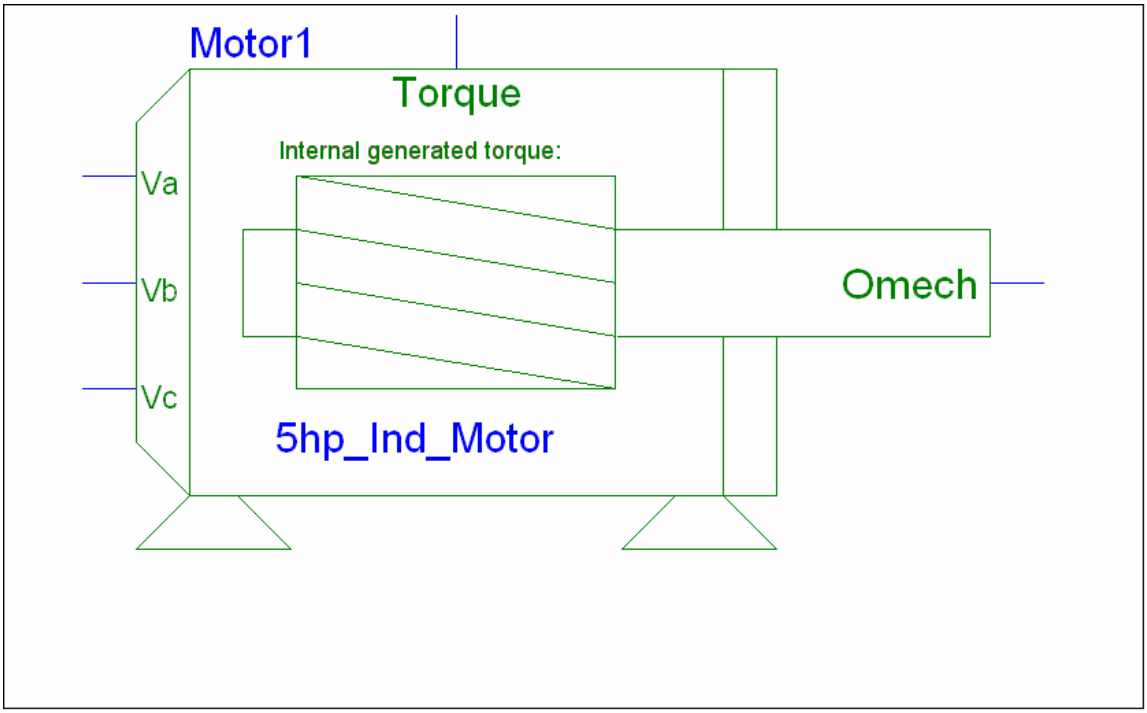

Figure 4.9: PSPICE Induction Motor Part.

TABLE 4.2

POWER FLOW RESULTS FOR THE 4-BUS SYSTEM

	Current	Converged		Current	Voltage	Converged		Voltage
	from	Current		Percent	from	Voltage		Percent
Bus	PSPICE	(Hand Calculations)	ΔI	Error	PSPICE	(Hand Calculations)	ΔV	Error
Number	(A)	(A)	(A)	(% of PSPICE)	(V)	(V)	(V)	(% of PSPICE)
3	27.6632	27.9287	0.2655	0.9597	534.6356	534.5013	0.13430	0.025120
4	15.3282	15.1268	0.2014	1.3140	536.5039	536.5974	0.09350	0.017428

4.3 Six-Step Simulation Results for a 10-bus System

The algorithm presented in Section 4.2 was coded in MATLAB for the purpose of conducting a power flow analysis on a larger DC system such as the one shown in Figure 4.10. The system shown in Figure 4.10 contains ten buses. Bus 1 is the swing bus, bus 2 is a non-contributing bus, and buses 3-10 all have motor-drive loads attached. The first

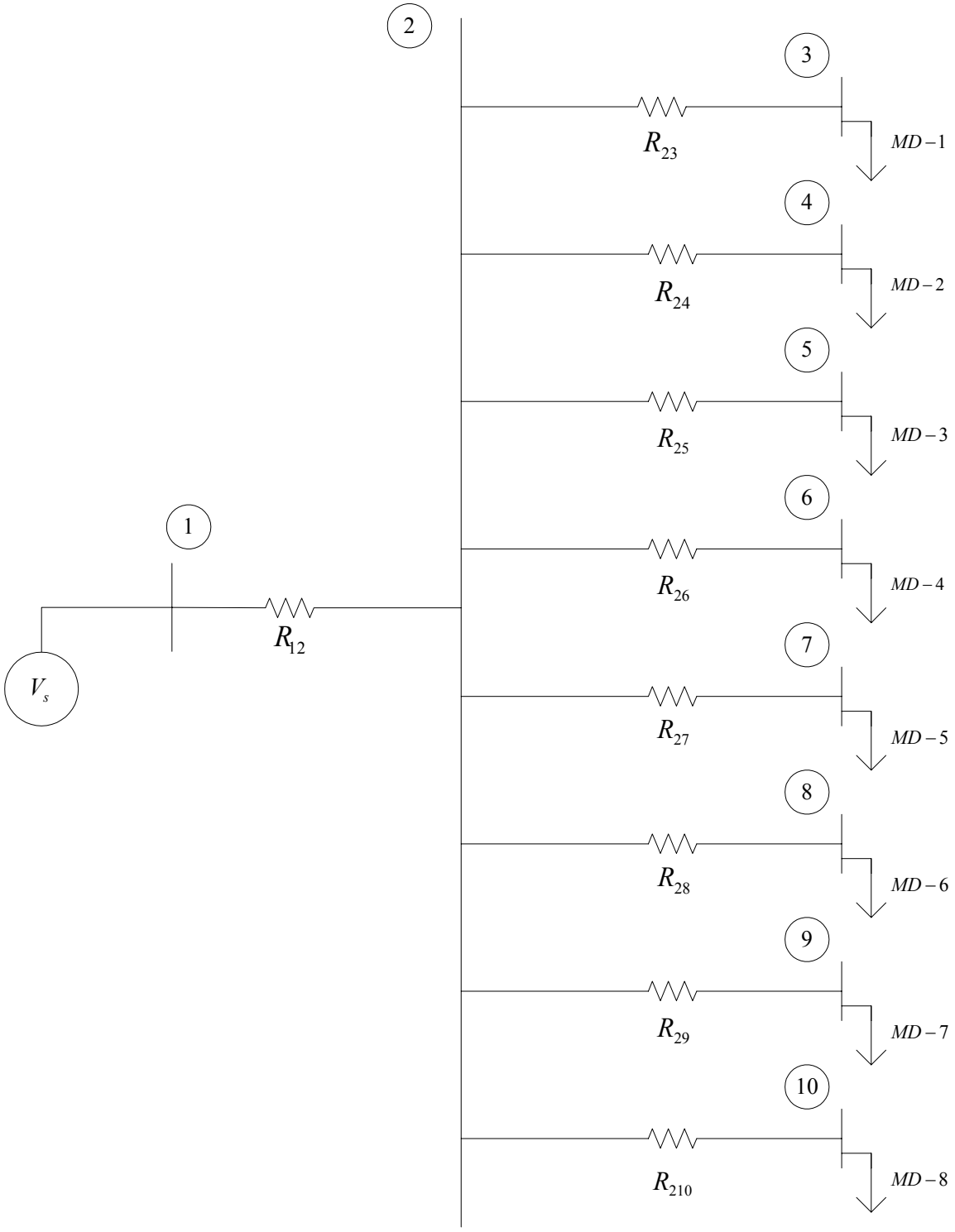

Figure 4.10: 10-bus DC Power System Model.

simulation of the system shown in Figure 4.10 was conducted with six-step voltage source inverters (180° conduction) with all of the induction motors in the system having the specifications listed in Table 3.1. The swing bus voltage was chosen to be 550V, with all of the line resistance values and load torques for the first simulation provided in Table 4.3.

The induction motor equations, six-step inverter relationships, and the power flow equations were all coded in MATLAB for the purpose of simulating the system in Figure 4.10. The voltage at each load bus of the system in Figure 4.10 was varied over a range of 496V-595V with all other parameters remaining unchanged. For comparison purposes and to verify the MATLAB power flow results, a PSPICE model of the DC power system in Figure 4.10 was constructed. The PSPICE model of the 10-bus system is in Figure 4.11. All parameters used in the PSPICE model were the same as the ones in MATLAB.

The converged voltages and currents from the MATLAB power flow program are shown in Table 4.4. The bus currents and bus voltages that resulted from the PSPICE simulation of the 10-bus system in Figure 4.10 are shown in Table 4.4. It can be observed from Table 4.4 that the MATLAB and PSPICE values for the bus voltages and currents closely match each other. This verifies that the simplified model discussed in Chapter 3 can be extended to a larger multiple-bus DC power system containing six-step voltage source inverter drive loads.

TABLE 4.3
SYSTEM LINE RESISTANCES AND LOAD TORQUES

	Load			Line
Bus	Torque		Line	Resistance
Number	(N-m)		Section	(mΩ)
1				
2			1 - 2	0.1
3	70		2 - 3	0.2
4	65		2 - 4	0.3
5	10		2 - 5	0.4
6	60		2 - 6	0.5
7	50		2 - 7	0.6
8	40		2 - 8	0.7
9	30		2 - 9	0.8
10	20		2 - 10	0.9

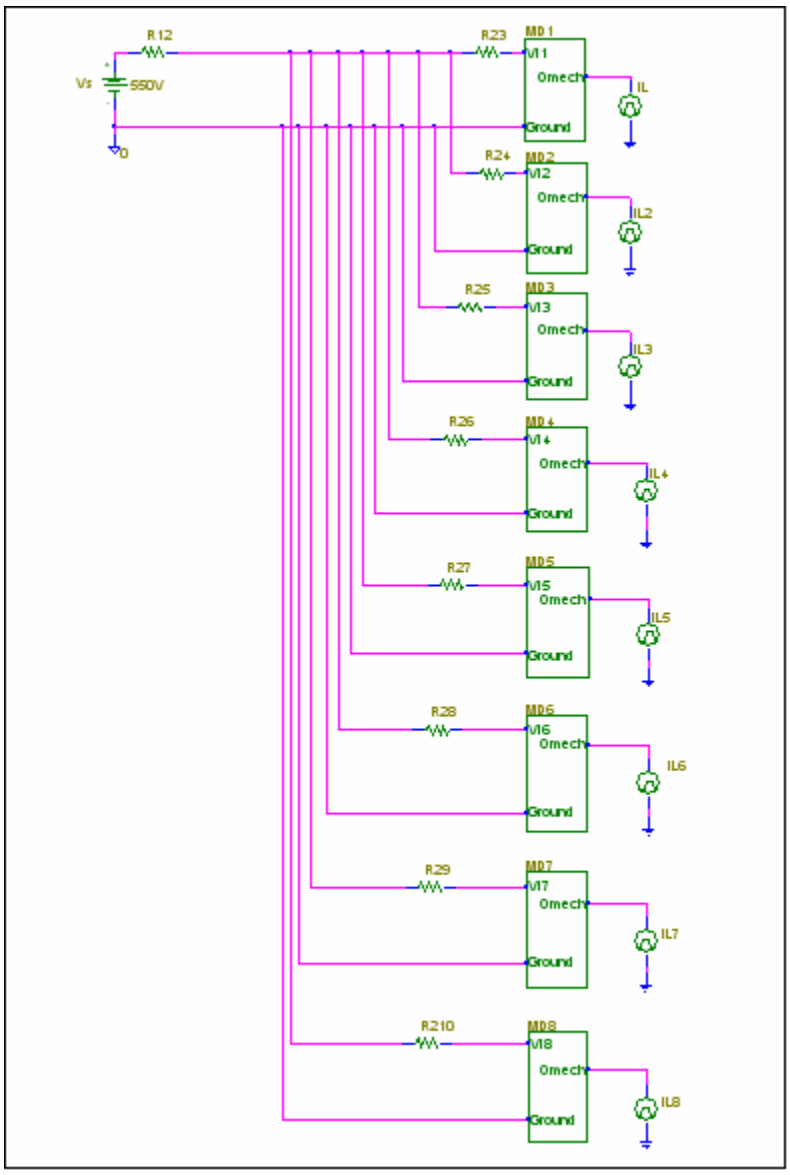

Figure 4.11: PSPICE 10-bus Power System Model.

TABLE 4.4
POWER FLOW RESULTS FOR THE SIX-STEP INVERTER

	Current	Converged		Current	Voltage	Converged		Voltage
	from	Current		Percent	from	Voltage		Percent
Bus	PSPICE	(Matlab)	ΔI	Error	PSPICE	(Matlab)	ΔV	Error
Number	(A)	(A)	(A)	(%)	(V)	(V)	(V)	(%)
3	24.9224	24.8885	0.0339	0.1359	549.9825	549.9826	0.00010	0.000018
4	23.1865	23.1518	0.0347	0.1497	549.9805	549.9806	0.00010	0.000018
5	4.2002	4.1618	0.0384	0.9141	549.9858	549.9859	0.00010	0.000018
6	21.4528	21.417	0.0358	0.1669	549.9768	549.9768	0.00000	0.000000
7	17.9889	17.9522	0.0367	0.2038	549.9767	549.9768	0.00010	0.000018
8	14.5318	14.4944	0.0374	0.2571	549.9773	549.9774	0.00010	0.000018
9	11.0815	11.0434	0.0381	0.3438	549.9786	549.9787	0.00010	0.000018
10	7.6380	7.5992	0.0388	0.5084	549.9806	549.9807	0.00010	0.000018

4.4 Two-Level Sinusoidal PWM Simulation Results

A simulation of the system in Figure 4.10 was conducted with two-level sinusoidal PWM voltage source inverters and induction motors with parameters as listed in Table 3.1. Bus 1 is the swing bus, bus 2 is a non-contributing bus, and the other buses are load buses with motor drive loads attached. The swing bus voltage was chosen to be 550V, with all of the line resistance values and load torques listed in Table 4.5. The inverter parameters used for all of the inverters in the system were: f_1=60 Hz, m_a=1.4, and m_f=15.

The induction motor equations, the two-level PWM inverter relationships, and the power flow equations were all coded in MATLAB in order to simulate the system in Figure 4.10. The voltage at each load bus of the system was again varied over the range of 496V-595V, with all other parameters in the system remaining unchanged. For comparison purposes and to verify the MATLAB power flow results, a PSPICE model of the DC power system in Figure 4.10 was constructed. This model was the same as the one in Figure 4.11 except that each block in the figure contained a two-level sinusoidal PWM inverter as shown in Figure 4.12.

TABLE 4.5
SYSTEM LINE RESISTANCES AND LOAD TORQUES

Bus Number	Load Torque (N-m)		Line Section	Line Resistance (mΩ)
1				
2			1 - 2	10
3	70		2 - 3	20
4	65		2 - 4	30
5	100		2 - 5	40
6	60		2 - 6	50
7	50		2 - 7	60
8	40		2 - 8	70
9	30		2 - 9	80
10	80		2 - 10	90

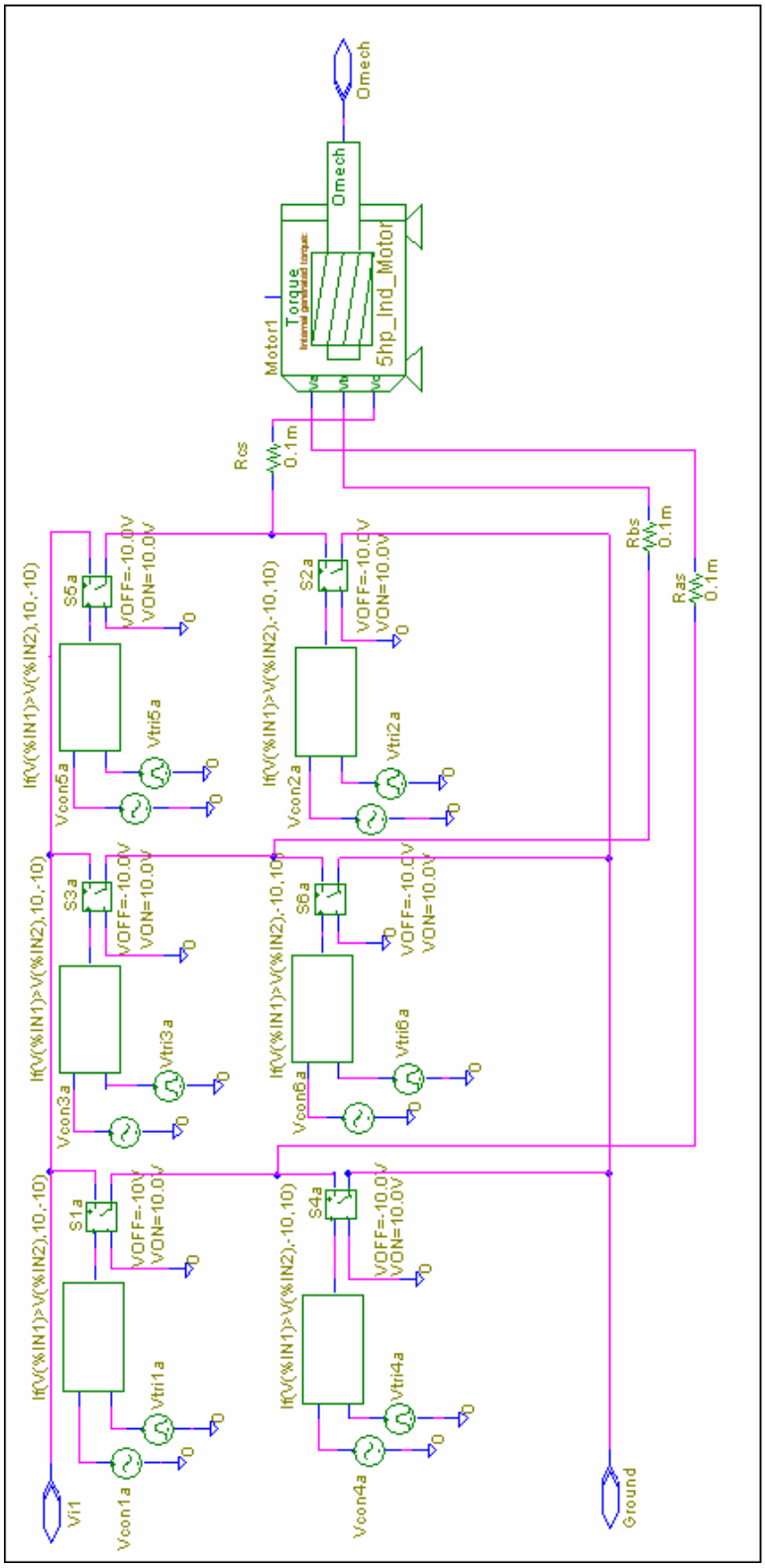

Figure 4.12: PSPICE Sinusoidal PWM Motor-Drive Model.

The converged voltages and currents from the MATLAB code are shown in Table 4.6. Simulation results from PSPICE for the bus voltages and currents are also shown in this table. These results verify that the simplified model discussed in Chapter 3 can also be extended to a larger multiple-bus DC power system containing sinusoidal PWM inverter drive loads.

TABLE 4.6
POWER FLOW RESULTS FOR THE TWO-LEVEL SINE PWM INVERTER

	Current	Converged		Current	Voltage	Converged		Voltage
	from	Current		Percent	from	Voltage		Percent
Bus	PSPICE	(Matlab)	ΔI	Error	PSPICE	(Matlab)	ΔV	Error
Number	(A)	(A)	(A)	(% of PSPICE)	(V)	(V)	(V)	(% of PSPICE)
3	24.6824	24.6512	0.0312	0.1262	547.7546	547.7583	0.00370	0.000675
4	22.9430	22.9104	0.0326	0.1422	547.5599	547.564	0.00410	0.000749
5	35.2968	35.253	0.0438	0.1241	546.8364	546.8412	0.00480	0.000878
6	21.2136	21.1773	0.0363	0.1710	547.1876	547.1924	0.00480	0.000877
7	17.7230	17.6864	0.0366	0.2063	547.1849	547.1901	0.00520	0.000950
8	14.2392	14.2022	0.0370	0.2595	547.2515	547.2571	0.00560	0.001023
9	10.7636	10.726	0.0376	0.3490	547.3871	547.3932	0.00610	0.001114
10	28.3157	28.2638	0.0519	0.1834	545.6998	545.7076	0.00780	0.001429

4.5 Power Flow Results for Systems with Higher Line Resistance Values

The focus of this section is on studying the behavior of a multiple-bus DC power system containing motor-drive loads when the line resistances in the system are increased. To begin the study, it is of interest to first analyze a single motor-drive system with a small line resistance such as the one shown in Figure 4.13. The inverter in this figure is a six-step voltage source inverter (180° conduction). The motor is a 50 HP induction motor with parameters as listed in Table 3.1. The source voltage is 460V, the line resistance is 0.1mΩ, and the load torque is 100 N-m. The PSPICE model, shown in Figure 4.13, was simulated for the purpose of studying the system behavior with a low

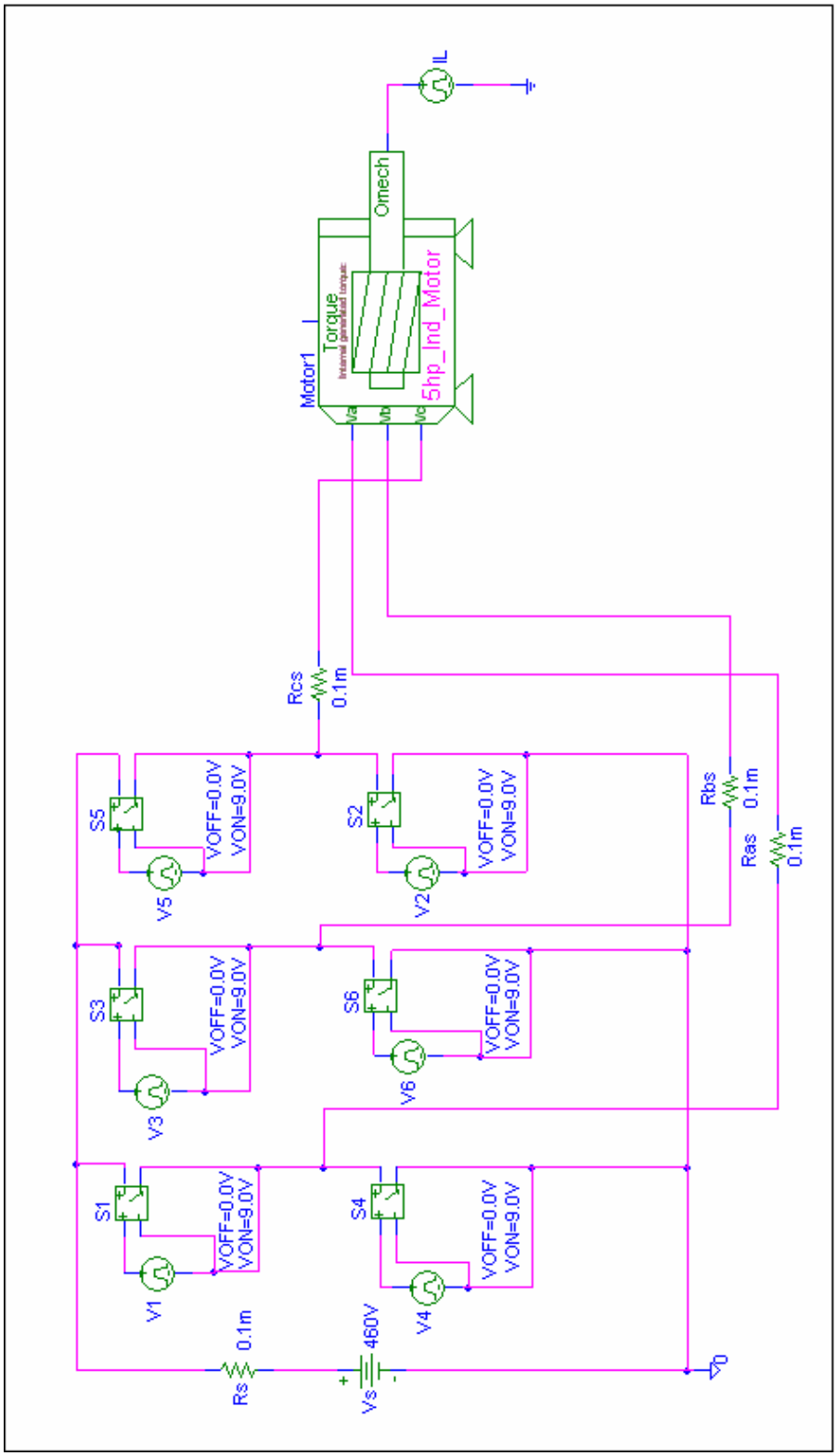

Figure 4.13: Six-Step Inverter System with a Low Line Resistance Value.

line resistance value. The line-to-line voltage waveforms that resulted from the simulation are shown in Figure 4.14. The inverter current and inverter voltage waveforms are shown in Figure 4.15.

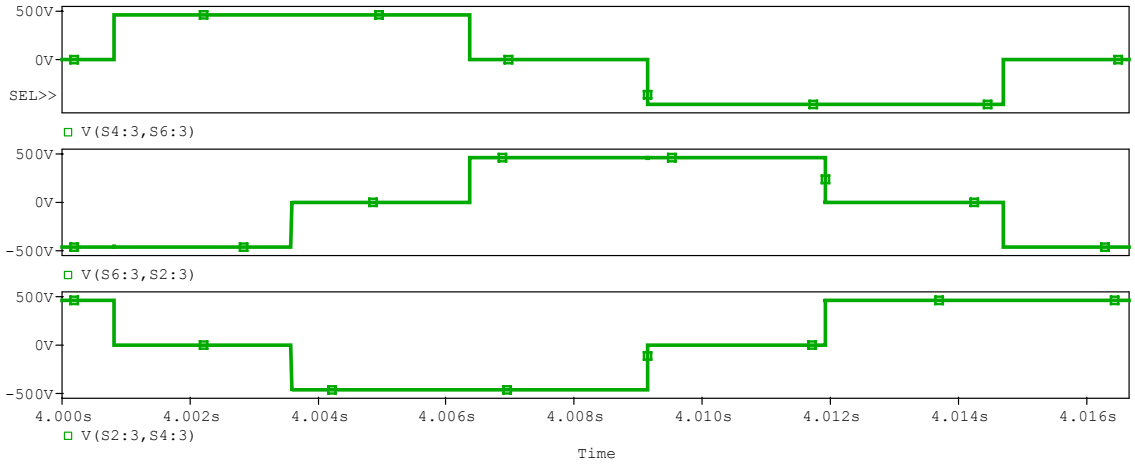

Figure 4.14: Line-to-Line Voltages with Low Line Resistance.

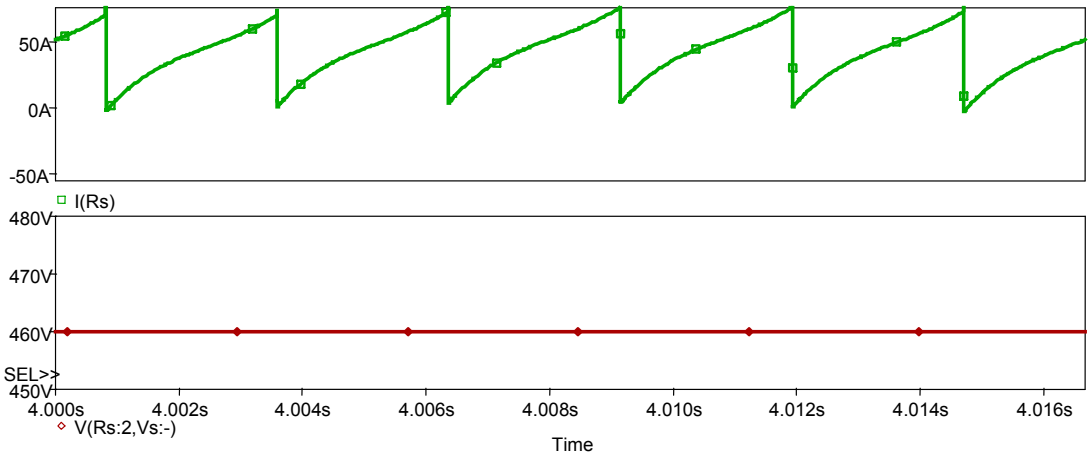

Figure 4.15: Inverter DC Input Current and Voltage with Low Line Resistance.

The line resistance of the system in Figure 4.13 was changed to 0.3 Ω as shown in Figure 4.16 and the system was simulated again in PSPICE to investigate the effects of increasing the line resistance on the behavior of the system. The line-to-line voltage waveform V_{ab} that resulted from the simulation is shown in Figure 4.17. As can be seen in Figure 4.17, the line-to-line voltage is beginning to deviate from the shape shown in Figure 4.14. The inverter input voltage waveform that resulted from the simulation is shown in Figure 4.18. It can be seen from this figure that the inverter input voltage is no longer a stiff DC voltage. The inverter input current waveform is shown in Figure 4.19.

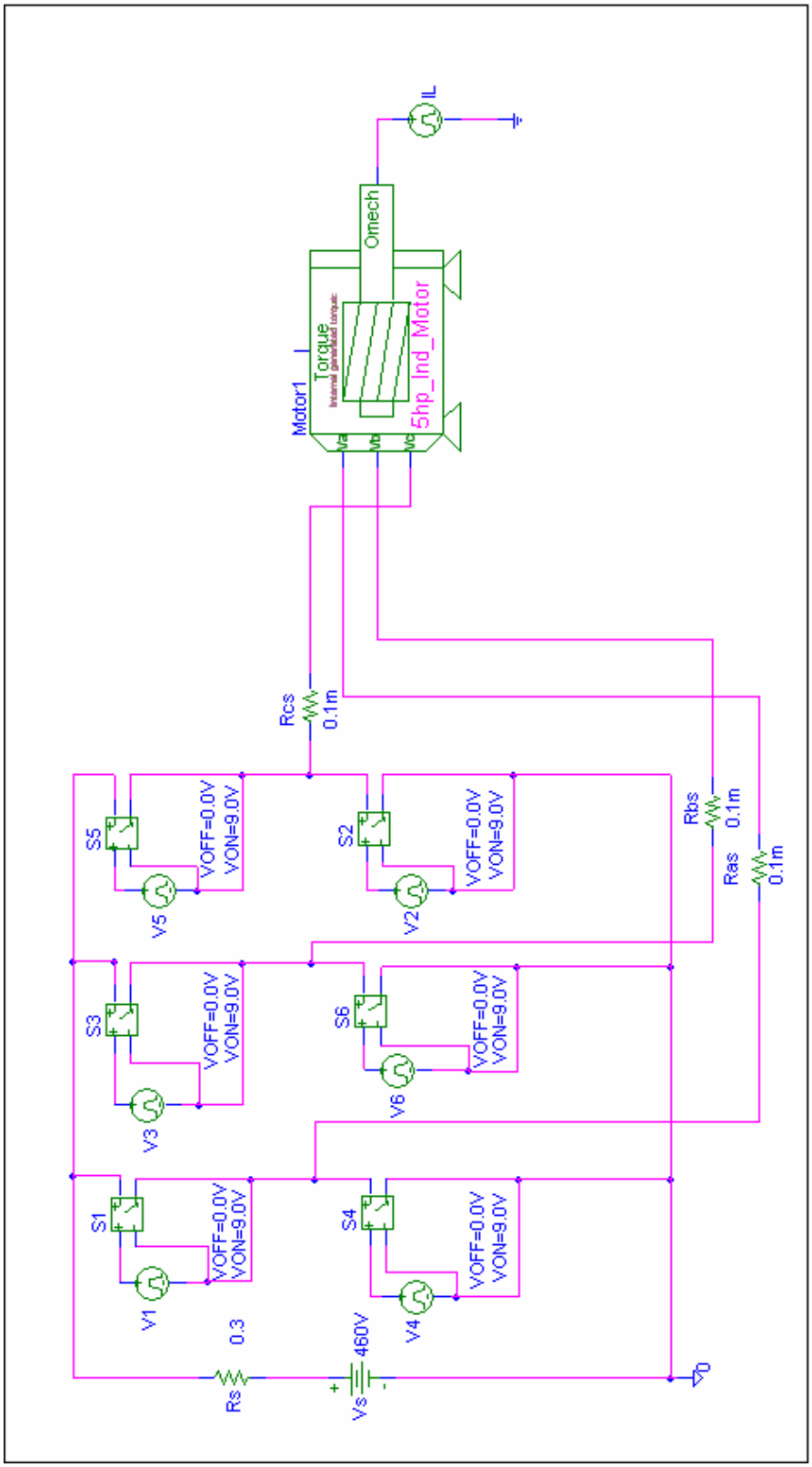

Figure 4.16: Six-Step Inverter System with a Higher Line Resistance Value.

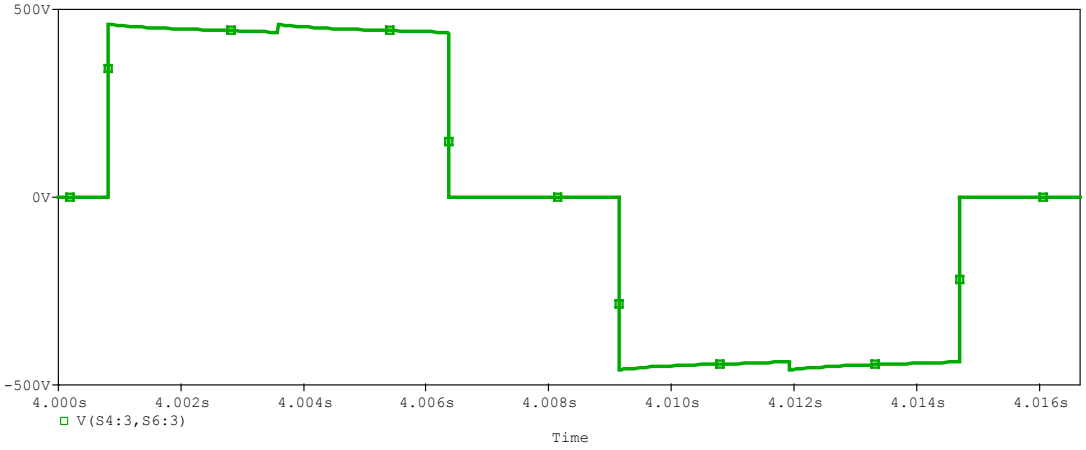

Figure 4.17: Line-to-Line Voltage (V_{ab}) with a Higher Line Resistance.

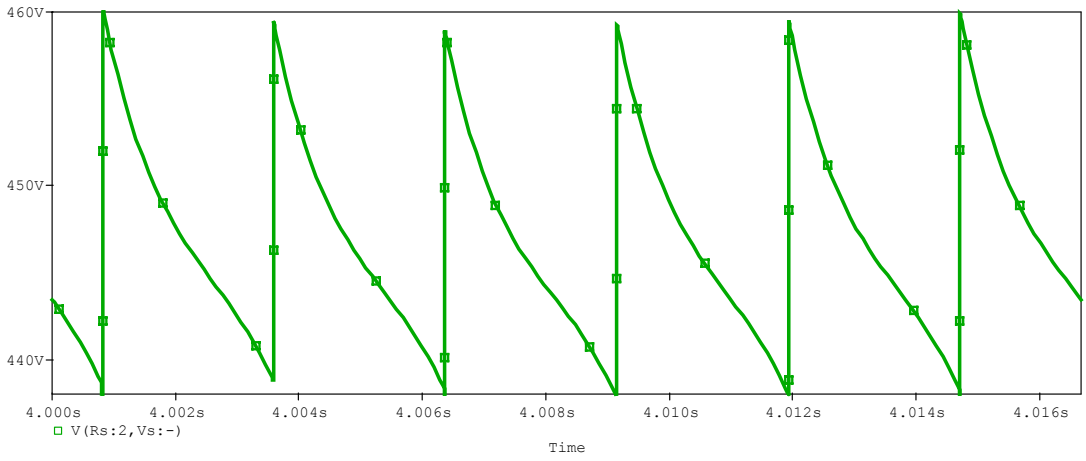

Figure 4.18: Inverter Input Voltage with a Higher Line Resistance.

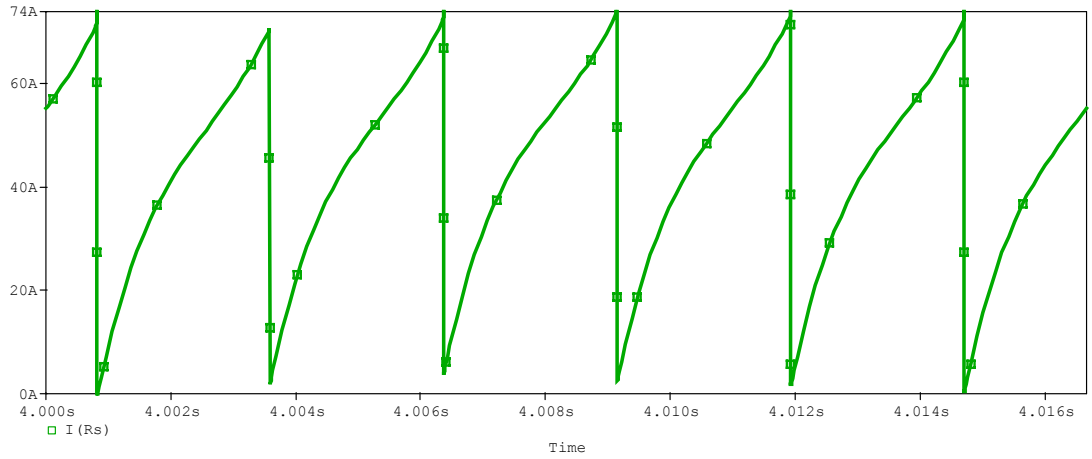

Figure 4.19: Inverter Input Current with a Higher Line Resistance.

A Fourier analysis was conducted as part of the PSPICE simulation on the inverter input current and inverter input voltage. The results of this Fourier analysis are shown in Table 4.7. It can be seen that the inverter input current and voltage are both rich in even harmonic content. Harmonics with multiples of six are present in both waveforms. It is obvious from these results that the distortion in the inverter input voltage will effect the output voltage waveforms of the inverter as shown in Figure 4.17.

In order to examine the effects of the presence of even harmonics on the input side of the inverters in a multiple-bus DC power system, the system in Figure 4.10 was modeled using the line resistance and load torque values listed in Table 4.8. The PSPICE model was constructed the same as in Figure 4.11 except for the line resistance values. The new system was also coded in MATLAB using the new line resistance values shown in Table 4.8. The results of the PSPICE simulation and the MATLAB power flow are shown in Table 4.9. As can be seen in this table, the presence of even harmonics on the input side of the inverters produces some larger differences between the MATLAB and PSPICE

TABLE 4.7
HARMONIC CONTENT OF INVERTER CURRENT AND VOLTAGE

	Inverter Input	**Inverter Input**			**Inverter Input**	**Inverter Input**
Harmonic	**Voltage**	**Voltage**		**Harmonic**	**Current**	**Current**
Number	**Magnitude**	**Angle**		**Number**	**Magnitude**	**Angle**
	(V)	(degrees)			(A)	(degrees)
DC	446.8914			DC	43.69524	
6	5.598	-94		1	1.557	-100.3
12	3.254	153.5		2	1.35	99.05
18	2.23	45.13		6	18.66	86
24	1.692	-62.17		8	1.107	-20.55
30	1.362	-169.2		12	10.85	-26.54
				14	1.013	-127.1
				18	7.434	-134.9
				22	1.002	32.53
				24	5.638	117.8
				28	1.057	-74.12
				30	4.54	10.85

TABLE 4.8
SYSTEM LINE RESISTANCES AND LOAD TORQUES

	Load			Line
Bus	Torque		Line	Resistance
Number	(N-m)		Section	(Ω)
1				
2			1 - 2	0.1
3	70		2 - 3	0.0009
4	65		2 - 4	0.1
5	35		2 - 5	0.15
6	60		2 - 6	0.2
7	50		2 - 7	0.25
8	40		2 - 8	0.3
9	30		2 - 9	0.35
10	25		2 - 10	0.4

TABLE 4.9
POWER FLOW RESULTS WITH LARGER LINE RESISTANCES

	Current	Converged		Current	Voltage	Converged		Voltage
	from	Current		Percent	from	Voltage		Percent
Bus	PSPICE	(MATLAB)	ΔI	Error	PSPICE	(MATLAB)	ΔV	Error
Number	(A)	(A)	(A)	(% of PSPICE)	(V)	(V)	(V)	(% of PSPICE)
3	26.0388	26.0361	0.0026	0.0102	535.5256	535.7882	0.26260	0.049036
4	24.4279	24.3197	0.1082	0.4429	533.1062	533.3797	0.27350	0.051303
5	13.7282	13.3794	0.3488	2.5409	533.4898	533.8048	0.31500	0.059045
6	22.7914	22.5762	0.2152	0.9441	530.9907	531.2964	0.30570	0.057572
7	19.2409	18.9213	0.3196	1.6609	530.7388	531.0813	0.34250	0.064533
8	15.7097	15.2617	0.4480	2.8518	530.8361	531.2332	0.39710	0.074807
9	12.1906	11.6049	0.5857	4.8047	531.2823	531.7499	0.46760	0.088013
10	10.3826	9.7839	0.5987	5.7665	531.3959	531.8981	0.50220	0.094506

results. The code written in MATLAB does not model the effects of the even harmonics, but PSPICE does account for the impact of even harmonics on the system. However, it can be observed from Table 4.9 that the higher line resistance values and the presence of even harmonics on the input side of the inverter did not significantly impact the accuracy of the MATLAB results. In practical applications, the line resistances in a system such as the one shown in Figure 4.10 are small due to the fact that the cable length between each drive and motor is typically less than 50 feet [54-56]. With cable lengths greater than 50 feet, it is possible to experience a voltage wave reflection at the motor terminals up to two times the applied voltage [57, 58]. This effect can be shown by using transmission line theory [54]. The line resistances that would result from the cable requirements outlined in [54-56] would be in a range similar to the ones listed in Table 4.5. In this line resistance range, the MATLAB code produced excellent results as can be seen in Table 4.6.

4.6 Summary

In this chapter, an iterative procedure was presented that can be used to conduct a power flow analysis on a DC power system containing motor-drive loads. It was shown that a V-I load characteristic curve can be developed for each motor-drive load and can then be incorporated into an iterative procedure to conduct a power flow analysis on a given system. The power flow algorithm was verified by conducting a power flow analysis on a 4-bus DC power system using hand calculations. The algorithm was coded in MATLAB and power flow results were presented for a 10-bus DC power system containing six-step voltage source inverter drive loads and a 10-bus DC power system containing sinusoidal PWM inverter drive loads. PSPICE models of each system were built and the results were compared to the MATLAB power flow results.

A study was conducted on an individual six-step inverter drive system that had a larger line resistance value to examine the effects of higher line resistances on a multiple-bus system. Even harmonics were present in the inverter input voltage and current waveforms of the system with a higher line resistance. However, the higher line resistance and the presence of even harmonics on the input side of the inverter did not significantly impact the accuracy of the MATLAB results.

CHAPTER 5

CONCLUSIONS

5.1 Summary

A simplified model of an inverter-fed induction motor has been developed to be used in the analysis of a DC power system containing motor-drive loads. The model was based on the steady-state T-type equivalent circuit of an induction motor and the input-output relationships of a voltage source inverter. In the simplified model, a V-I load characteristic curve was established that allowed the inverter, motor, and load to be replaced by a current-controlled voltage source. Power flow analyses were conducted in MATLAB using the simplified model and the results were comparable to PSPICE. The simplified model used in the analysis of a multiple-bus DC power system by incorporating the V-I load curves of each motor-drive load in a particular system into a Newton-Raphson type iterative procedure.

The focus of Chapter 2 was on the harmonic analysis of different types of voltage source inverters. The types of inverters analyzed in Chapter 2 included: (1) the six-step inverter, (2) the sinusoidal PWM inverter, and (3) the space vector PWM inverter. Two methods for finding the harmonic components of the output voltage of sinusoidal PWM inverters and space vector PWM inverters were presented in Chapter 2. The method of pulse pairs was the first method discussed. This method was shown to be applicable to different multilevel inverter types such as the two-level sinusoidal PWM inverter and the

three-level sinusoidal PWM inverter. The main limitation of the method of pulse pairs was the possibility of the loss of symmetry in the output voltage of the inverter. In this scenario, there would no longer be corresponding pulse pairs. The method of multiple pulses was developed to overcome this limitation. This method was used to calculate the Fourier coefficients of individual positive and negative pulses of the output PWM waveform. The coefficients of the individual pulses were added together using the principle of superposition to calculate the Fourier coefficients of the entire PWM output signal.

The final expression for the PWM output voltage can be expressed compactly in a single-cosine Fourier series that allows direct calculation of harmonic components and can easily be implemented in a computer software package such as MATLAB. This method allows direct calculation of harmonic magnitudes and angles without having to use look-up tables, linear approximations, iterative procedures, Bessel functions, or the gathering of harmonic terms required by other methods. The method of multiple pulses, presented in Chapter 2, is entirely general and has the potential to be used to analyze the harmonic content of inverter output waveforms produced by various types of multilevel inverters and PWM schemes. There is no limitation to the method of multiple pulses due to loss of symmetry or the harmonic content of the inverter output voltage waveform. The method of multiple pulses can also be used to calculate the harmonic content of inverter waveforms produced by the six-step inverter. This method can be extended to analyze other types of multilevel inverters and PWM schemes not studied in this dissertation.

A harmonic model of the induction motor operating under balanced, steady-state conditions was presented in Chapter 3. The model produced simulation results for an induction motor supplied from a nonsinusoidal source that was comparable to EMAP [49]. A simplified model of an inverter-fed induction motor that was based on the steady-state T-type equivalent circuit and the input-output relationships of the voltage source inverter was developed. A *V-I* load characteristic curve was established that allowed the inverter, motor, and load to be replaced by a current-controlled voltage source. The model was coded in MATLAB and compared with PSPICE simulations. The model was shown to be applicable to six-step, sinusoidal PWM, and space vector PWM inverters.

An iterative procedure was presented in Chapter 4 that can be used to perform a power flow analysis on a DC power system containing motor-drive loads. The simplified model presented in Chapter 3 was shown to be applicable to the analysis of a multiple-bus DC power system containing motor-drive loads by forming the *V-I* characteristic curve of each motor-drive load in a given system. The *V-I* load characteristic curve developed for each motor-drive load in a DC power system can then be incorporated into an iterative procedure to perform a power flow analysis on a particular system. The power flow algorithm was verified by conducting a power flow analysis on a 4-bus DC power system using hand calculations. The algorithm was then coded in MATLAB and power flow analyses were conducted on a 10-bus DC power system containing six-step inverter-drive loads and PWM inverter-drive loads. PSPICE models of each system were constructed and simulated. The MATLAB power flow results were found to be comparable to PSPICE.

Chapter 4 also included a section on the impact of larger line resistance values for an individual six-step inverter drive system. The system was constructed in PSPICE for simulation purposes. The results of the PSPICE simulations were used to examine the effects of higher line resistances on a multiple-bus system. The larger line resistance was shown via PSPICE simulations to produce even harmonics in the inverter input voltage and inverter input current waveforms. Power flow results from simulation of a 10-bus DC power system containing six-step inverter drives demonstrated that the higher line resistance values and the presence of even harmonics in the inverter input current and voltage did not have a significant impact on the accuracy of results.

5.2 Recommendations for Future Work

An area for future consideration is the study of the effects caused by higher line resistance values. Even harmonics appear in the inverter input voltage waveform when the line resistances are higher. The appearance of even harmonics in the inverter input voltage will affect other machine variables such as the line-to-line voltages.

Various researchers have developed methods for calculating the inverter input current of a six-step voltage source inverter [9-13 and 59]. Most of these methods use a power balance between the inverter input and the inverter output to establish an expression for the inverter current. An instantaneous power balance between the inverter input and inverter output was used by some of the researchers [10, 11, and 59] to develop an expression for the inverter current in terms of the synchronously rotating reference frame currents.

In the methods that used instantaneous power balance [10, 11, and 59], electric machine reference frame transformations and the Fourier series of the six-step inverter

voltage waveforms were used to represent the inverter-drive system in the synchronously rotating reference frame. An expression for the inverter input current was then developed in terms of the synchronously rotating reference frame currents. However, the results presented in [10, 11, and 59] are based on the assumption that the inverter input voltage is a stiff DC voltage. As noted by [59], the determination of harmonics on both the input and output sides of an inverter that has even harmonics present in the input voltage is a complex problem and normally requires a detailed computer simulation using PSPICE or other computer circuit simulation packages to produce accurate results.

REFERENCES

[1] S.D.T. Robertson and K.M. Hebbar, "Torque Pulsatins in Induction Motors with Inverter Drives," IEEE Transactions on Industry and General Applications, vol. IGA-7, no. 2, Mar./Apr. 1971, pp. 318-323.

[2] V.B. Honsinger, "Induction Motors Operating from Inverters," in *Conference Record of the 1980 Annual Meeting of the Industry Applications Society*, pp. 1276-1285.

[3] M.A. Rahman, "Efficiency of Inverter-Fed Induction Motors," in *Conference Record of the 1980 Annual Meeting of the Industry Applications Society*, pp. 1286-1291.

[4] K. Venkatesan and J.F. Lindsay, "Comparative Study of the Losses in Voltage and Current Source Inverter Fed Induction Motors," IEEE Transactions on Industry Applications, vol. IA-18, no. 3, May/June 1982, pp. 240-246.

[5] A. Iliadis, L. Heming, and T.H. Barton, "Time Domain Analysis of Induction Motors with Non-Sinusoidal Supplies," in *Conference Record of the 1983 Annual Meeting of the Industry Applications Society*, pp. 555-564.

[6] S.M. Abdulrahman, J.G. Kettleborough, and I.R. Smith, "Fast Calculation of Harmonic Torque Pulsations in a VSI/Induction Motor Drive," IEEE Transactions on Industrial Electronics, vol. 40, no. 6, Dec. 1993, pp. 561-569.

[7] E. Muljadi, "PV Water Pumping with a Peak-Power Tracker Using a Simple Six-Step Square-Wave Inverter," IEEE Transactions on Industry Applications, vol. 33, no. 3, May/June 1997, pp. 714-721.

[8] J.M.D. Murphy and F.G. Turnbull, *Power Electronic Control of AC Motors*, NY: Pergamon Press, 1988.

[9] M. Abbas, and D.W. Novotny, "Stator Referred Equivalent Circuits for Inverter Driven Electric Machines," in the *Conference Record of the 1978 Annual Meeting of the Industry Applications Society*, IAS78:29A, pp. 828-835.

[10] P.C. Krause and T.A. Lipo, "Analysis and Simplified Representations of a Rectifier-Inverter Induction Motor Drive," IEEE Transactions on Power Apparatus and Systems, vol. PAS-88, no. 5, May 1969, pp. 588-596.

[11] P.C. Krause and J.R. Hake, "Method of Multiple Reference Frames Applied to the Analysis of a Rectifier-Inverter Induction Motor Drive," IEEE Transactions on Power Apparatus and Systems, vol. PAS-88, no. 11, Nov. 1969, pp. 1635-1641.

[12] D.W. Novotny, "Switching Function Representation of Polyphase Invertors," in the *Conference Record of the 1975 Annual Meeting of the Industry Applications Society*, pp. 823-831.

[13] D.W. Novotny, "Steady State Performance of Inverter Fed Induction Machines by Means of Time Domain Complex Variables," *IEEE Transactions on Power Apparatus and Systems*, vol. PAS-95, no. 3, May/June 1976.

[14] K. Tseng, W. Kao, Y. Cheng, and S. Lin, "Analytical Solution to Harmonic Characteristics of Three-Phase PWM Inverter Using 3-D Modulation Model," *Electric Power Components and Systems*, vol. 32, no. 11, Nov. 2004, pp. 1105-1120.

[15] G. Franzo, M. Mazzucchelli, L. Puglisi, and G. Sciutto, "Analysis of PWM Techniques Using Uniform Sampling in Variable-Speed Electrical Drives with Large Speed Range," *IEEE Transactions on Industry Applications*, vol. IA-21, no. 4, July/Aug. 1985, pp. 966-974.

[16] D.G. Holmes and T.A. Lipo, *Pulse Width Modulation for Power Converters: Principles and Practice*, NJ: 2003, pp. 95-257.

[17] J. Hamman and F.S. Van Der Merwe, "Voltage Harmonics Generated by Voltage-Fed Inverters Using PWM Natural Sampling," *IEEE Transactions on Power Electronics*, vol. 3, no. 3, July 1988, pp. 297-302.

[18] G.W. Chang and S.K. Chen, "Characterizing Harmonic and Interharmonic Currents Generated by the VSI-Fed Adjustable Speed Drives," in the *Conference Record of the International Conference on Power System Technology*, vol. 1, 2004, pp. 475-480.

[19] W.R. Bennett, "New Results in the Calculation of Modulation Products," *The Bell System Technical Journal*, vol. 12, Apr. 1933, pp. 228-243.

[20] H.S. Black, *Modulation Theory*, NY: 1953, pp. 263-281.

[21] S.R. Bowes and B.M. Bird, "Novel Approach to the Analysis and Synthesis of Modulation Processes in Power Converters," *Proceedings of the IEE*, vol. 122, no. 5, May 1975, pp. 507-513.

[22] S.R. Bowes, "New Sinusoidal Pulsewidth-Modulated Invertor," *Proceedings of the IEE*, vol. 122, no. 11, Nov. 1975, pp. 1279-1285.

[23] M. Mazzucchelli, L. Puglisi, and G. Sciutto, "PWM Systems in Power Converters: An Extension of the "Subharmonic" Method," *IEEE Transactions on Industrial Electronics and Control Instrumentation*, vol. IECI-28, no. 4, Nov. 1981, pp. 315-322.

[24] G. Carrara, S. Gardella, M. Marchesoni, R. Salutari, and G. Sciutto, "A New Multilevel PWM Method: A Theoretical Analysis," *IEEE Transactions on Power Electronics*, vol. 7, no. 3, July 1992, pp. 497-505.

[25] D.G. Holmes, "A General Analytical Method for Determining the Theoretical Harmonic Components of Carrier Based PWM Strategies," in *Proceedings of the IEEE Industry Applications Conference*, 1998, pp. 1207-1214.

[26] K. Tseng, W. Kao, Y. Cheng, and S. Lin, "Analytical Solution to Harmonic Characteristics of Three-Phase PWM Inverter Using 3-D Modulation Model," *Electric Power Components and Systems*, vol. 32, no. 11, Nov. 2004, pp. 1105-1120.

[27] N. Mohan, T.M. Undeland, W.P. Robbins, *Power Electronics: Converters, Applications, and Design ,* NY: 1995, pp. 206-210.

[28] S.R. Bowes and Y. Lai, "The Relationship Between Space-Vector Modulation and Regular-Sampled PWM," *IEEE Transactions on Industrial Electronics*, vol. 44, no. 5, Oct. 1997, pp. 670-679.

[29] J.T. Boys and P.G. Handley, "Harmonic Analysis of Space Vector Modulated PWM Waveforms," *IEE Proceedings*, vol. 137, Pt. B, no. 4, July 1990, pp. 197-204.

[30] D. Rathnakumar, J. LakshmanaPerumal, and T. Srinivasan, "A New Software Implementation of Space Vector PWM," in *Proceedings of IEEE SoutheastCon*, 2005, pp. 131-136.

[31] R.S. Kanchan, M.R. Baiju, K.K. Mohapatra, P.P. Ouseph, and K. Gopakumar, "Space Vector PWM Signal Generation for Multilevel Inverters Using Only the Sampled Amplitudes of Reference Phase Voltages," *IEE Proceedings – Electric Power Applications*, vol. 152, no. 2, Mar. 2005, pp. 297-309.

[32] J. Holtz and S. Stodtfeld, "A Predictive Controller for the Stator Current Vector of AC Machines Fed from a Switched Voltage Source," in *Conference Record of the IPEC Conference*, 1983, pp. 1665-1675.

[33] H.W. Van Der Broeck, H.C. Skudenly, and G.V. Stanke, "Analysis and Realization of a Pulse Width Modulator Based on the Voltage Space Vectors,"

IEEE Transactions on Industry Applications, vol. 24, no. 1, Jan./Feb. 1988, pp. 142-150.

[34] O. Ogasawara, H. Akagi, and A. Nabae, "A Novel PWM Scheme of Voltage Source Inverters Based on Space Vector Theory," in *ConferenceRecord of theEuropean Power Electronics Conference*, 1989, pp. 1197-1202.

[35] K. Bresnahan, H.Z. De La Parra, R. Teodorescu, and P.D. Evans, "Harmonic Analysis of SVM and Experimental Verification in a General Purpose Induction Motor Test Rig," in *Proceeding of 5th International Conference on Power Electronics and Variable-Speed Drives*, 1994, pp. 352-356.

[36] J.F. Moynihan, M.G. Egan, and J.M.D. Murphy, "Theoretical Spectra of Space-Vector-Modulated Waveforms," *IEE Proceedings – Electric Power Applications*, vol. 145, no. 1, Jan. 1998, pp. 17-24.

[37] S. Halasz, I. Varjasi, and A. Zakharov, "Novel Voltage Spectra Investigation of Space Vector Modulation Technique," in *Proceeding of the 29th Annual Conference of the IEEE Industrial Electronics Society*, 2003, pp. 2660-2666.

[38] R.C. Panaitescu and N. Mohan, "A Simple Space-Vector PWM Algorithm for VSI-fed AC Motor Drives," in *Proceedings of the Applied Power Electronics Conference and Exposition*, vol. 1, Mar. 2002, pp. 72-75.

[39] N. Mohan, *Advanced Electric Drives: Analysis, Control and Modeling using Simulink®*, MNPERE, MN: 2001, pp. 7-1 - 7-11.

[40] A.E. Fitzgerald, C. Kingsley, Jr., and S.D. Umans, *Electric Machinery, 5th ed.*, McGraw-Hill, Inc., NY: 1990, pp. 332-342.

[41] B. Ozpineci and L.M. Tolbert, "Simulink Implementation of Induction Machine Model – A Modular Approach," in *Proceedings of the IEEE International Electric Machines and Drives Conference*, vol. 2, June 2003, pp. 728-734.

[42] Giesselmann, M., "Advanced Simulation of Motor Drives and Power Electronics using PSPICE®", Tutorial for the Industrial Drives Committee, IAS Annual Meeting, pp.1-117, 2001.

[43] P.C. Krause, *Analysis of Electric Machinery*, McGraw-Hill, NY: 1986.

[44] A.W. Leedy and R.M. Nelms, "Simplified Model of an Inverter-Fed Induction Motor for the Analysis of a DC Power System," in *Proceedings of the 36th IEEE Southeastern Symposium on System Theory*, 2004, pp. 275-279.

[45] H.W. Van Der Broeck, "Analysis of the Harmonics in Voltage Fed Inverter Drives Caused by PWM Schemes with Discontinuous Switching Operation," in

Proceedings of the 3rd European Conference on PowerElectronics and Applications, 1991, pp. 261-266.

[46] R.C. Panaitescu and N. Mohan, "A Simple Space-Vector PWM Algorithm for VSI-fed AC Motor Drives," in *Proceedings of the 17th Annual IEEE Applied Power Electronics Conference and Exposition*, 2002, pp. 72-75.

[47] R.A. Pearman, *Power Electronics: Solid State Motor Control*, Reston Publishing Company, Inc., VA: 1980, pp. 170-182.

[48] P.C. Krause, and O. Wasynczuk, *Electromechanical Motion Devices*, McGraw-Hill, Inc., NY: 1989, pp. 171-193.

[49] T. Kataoka, Y. Kandatsu, and T. Akasaka, "Measurement of Equivalent Circuit Parameters of Inverter Fed Induction Motors," IEEE Transactions on Magnetics, vol. MAG-23, no. 5, Sept. 1987, pp. 3014-3016.

[50] C.A. Gross, "EMAP: An Aid to Understanding Energy Conversion Device Performance," IEEE Transactions on Power Systems, vol. 11, no. 2, May 1996, pp. 607-612.

[51] C.A. Gross, *Power System Analysis*, 2nd ed., John Wiley & Sons, Inc., NY: 1986, pp. 255-273.

[52] W.D. Stevenson, Jr., *Elements of Power System Analysis*, New York: McGraw-Hill, Inc., 1982.

[53] K.M. Brown and S.D. Conte, "The Solution of Simultaneous Nonlinear Equations," in *Proceedings of the A.C.M. National Meeting*, 1967, pp. 111-114.

[54] A. von Jouanne, P. Enjeti, and W. Gray, "The Effect of Long Motor Leads on PWM Inverter Fed AC Motor Drive Systems," in *Proceedings of the 10th Annual IEEE Applied Power Electronics Conference and Exposition*, 1995, pp. 592-597.

[55] A.H. Bonnett, "A Comparison Between Insulation Systems Available for PWM Inverter Fed Motors," IEEE Transactions on Industry Applications, vol. 33, no. 5, Sept./Oct. 1997, pp. 1331-1341.

[56] G. Skibinski, D. Leggate, and R. Kerkman, "Cable Characteristics and Their Influence on Motor Over-Voltages," in *Proceedings of the 12th Annual IEEE Applied Power Electronics Conference and Exposition*, 1997, pp. 114-121.

[57] A. von Jouanne and P.N. Enjeti, "Design Considerations for an Inverter Output Filter to Mitigate the Effects of Long Motor Leads in ASD Applications," IEEE Transactions on Industry Applications, vol. 33, no. 5, Sept./Oct. 1997, pp. 1138-1145.

[58] T.R. Mukundan, "Calculation of Voltage Surges on Motors Fed From PWM Drives – A Simplified Approach," IEEE Transactions on Energy Conversion, vol. 19, no. 1, March 2004, pp. 223-225.

[59] B.K. Bose, *Power Electronics and AC Drives*, Prentice-Hall, NJ: 1986.